2018

Synthesis and Characterization of Magnetic Cabides and Oxides Nanomaterials

Hei Man Tsui
Virginia Commonwealth University

Synthesis and Characterization of Magnetic Carbides and Oxides Nanomaterials

A dissertation in partial fulfillment of the requirement for the degree of doctor of philosophy at Virginia Commonwealth University

by

Hei Man Tsui

B.S., Virginia Polytechnic and State University, 2012

Director: Everett E. Carpenter

Professor, Department of Chemistry

Virginia Commonwealth University

Richmond, Virginia

May 2018

Acknowledgements

In the completion of this dissertation, there are many people whom I owe my thanks. First, my fiancé Brian for his love, support, and patience being by my side through this journey. Brain has always believe in me and give me the confidence that I need. My parents for their inspiration and guidance, they are always there and just one phone call away. In addition, I would like to thank my friends and family - I apologize for many skipped vacations, family reunions, game nights etc.

I would also like to thank Dr. Everett Carpenter for his guidance and direction throughout this journey. Dr. Carpenter gave me the freedom to explore new areas of research, and at the same time contribute to valuable advice. My committee members, VCU Department of Chemistry, and VCU Nanomaterials Core Characterization facilities for allowing me as well as and providing assistance to study my research topics. I would also like to thank my lab mates especially Sarah Smith, Brent Williams, and Dustin Clifford for their help with instrumentation training as well as data analysis.

I am thankful to have met Dr. Karen J. Brewer, who, although no longer with us, encouraged me on this journey toward my Ph.D. I will be forever thankful for the opportunity that she had given me to be a part of her research group at Virginia Tech. In addition, I would like to thank Dr. Shamindri Arachchige. I am very grateful to have met her during my time at Dr. Brewer's research group in 2009. She has been a good friend ever since.

Table of Contents

List of Figures

List of Tables

Abstract

SYNTHESIS AND CHARACTERIZATION OF MAGNETIC CARBIDES AND OXIDES NANOMATERIALS

Hei Man Tsui

A dissertation in partial fulfillment of the requirements for the degree of Doctor of Philosophy at Virginia Commonwealth University

Virginia Commonwealth University, 2017

Director: Dr. Everett E. Carpenter

Professor, Department of Chemistry

The design and development of nanoparticles is of great interest in the current energy and electronic industry. However, based on the current materials available the production cost can be high with insignificant magnetic and mechanical properties. Specifically, rare-earth magnetic materials composed of neodymium and samarium are known for their high magnetic performance, however, due to the cost of development there is a need to develop a versatile and cost effective material. Alternatively, cobalt carbide nanomaterials have shown to be a promising alternative for

rare-earth free magnets as they exhibit comparable properties as hexaferrite magnetic materials. The primary goal of this dissertation focuses on the development of nanoparticles for permeant magnetic, and magnetic refrigeration applications. The first part of this work focuses on the synthesis of cobalt carbide (Co_xC, x=2,3) nanoparticles using a novel polyol synthesis method by introducing a small amount of Ru, Cu, or Au as nucleating agent. It was found that the morphology and magnetic properties of the as-synthesized Co_xC nanoparticles change as a result of directional growth of nanoparticles using nucleating agents. Needle-like particle morphology ranges from 20-50 nm in width and as long as 1 μm in length were synthesized using Ru as nucleating agent. These particles exhibit magnetization saturation of 33.5 emu/g with a coercivity of 2870 Oe and a maximum energy product 1.92 MGOe (BH_{max}) observed. Particle morphology is a critical aspect in the development of magnetic nanoparticles as anisotropic particles have shown increased coercivity and magnetic properties. These Co_xC nanomaterials have a higher maximum energy product compared to previous work providing further insight into the development of non-rare earth magnetic material.

The second part of this dissertation work focuses on the sol-gel synthesis of perovskite $LaCaMnO_3$ (LCMO) nanomaterials. In this process, various chain lengths of polyethylene glycol (PEG) was added into a solution consisting of La, Ca, and Mn salts. The solution was left for the gelation process, and high temperature sintering to obtain the final product. By varying the polymer chain of the PEG, the size of the as synthesized $LaCaMnO_3$ nanomaterials were altered. The as-synthesized LCMO nanomaterials have shown a maximum change in magnetic entropy ($-\Delta S_M$) was found to be 19.3 $Jkg^{-1}K^{-1}$ at 278 K for a field change of 0-3 T and 8.7 $Jkg^{-1}K^{-1}$ for a field change of 0-1 T. This is a significant improvement in comparison to current literature of the material suggesting that this is a promising alternative to Gd materials that is prone to oxidation.

With additional development, LCMO or related maganites could lead to application in commercial technologies.

Chapter 1: Introduction

1.1.Overview

Modern society has been relying on the use of magnetic materials for applications such as data storage, generators, motors, sensors, environmental remediation etc.[2-6] This dissertation focuses on the synthesis of magnetic hard magnet and magnetocaloric materials for the enhancement of energy applications. As the current demand for electric transportation increases over the years, the demand for rare earth type permanent magnetic materials have been increasing with the need for higher efficiency and smaller size materials to replace induction type machines. Rare earth permanent magnets with Sm, Dy and Nd contents are among the most popular materials as they have shown excellent thermal magnetic response as well as high flux density for permanent magnet type electric machines. Currently, China dominates 95% of production of rare earth metals and in 2011 China has limited the export of rare earth metals for serval months that lead to a rare earth metal crisis as counties were scrambling for alternatives.[6] Since then research and development of rare earth free magnetic material is crucial since the cost of the mining process of

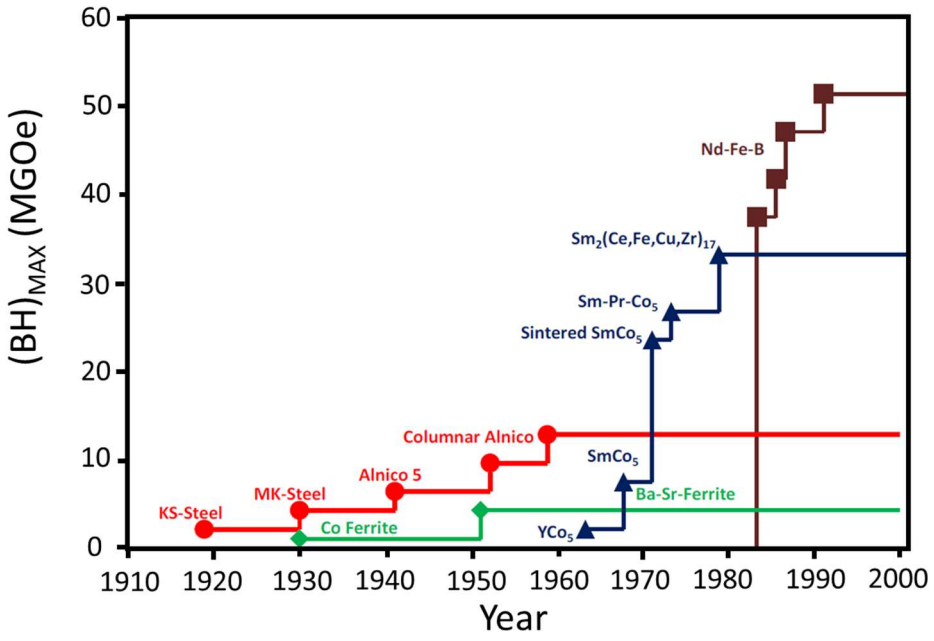

Figure 1. Energy density of magnetic material over the years. Modified from ref [1].

rare earth metals has a negative environmental and human impact.[7] Doped iron oxide, and AlNiCo are among the most popular rare earth free permanent magnetic materials as shown in Figure 1. Recent research has shown that transition metal (Co, Fe) carbides and nitrides have promising properties for hard magnetic applications with energy density up to 20 MGOe in $Fe_{16}N_2$ material.[8] However, the efficiency of current materials are significantly less than Nd based compounds.

Magnetic materials that have shown magnetocaloric effect (MCE) have gained interest in recent years as the demand for energy efficiency increases. Magnetic refrigeration (MR) technology has shown to be 30% more efficient in comparison to conventional cooling and refrigeration that rely on compressed gas systems.[1] MR technology is based on the MCE where adiabatic demagnetization is observed in a material. In theory, MCE is observed in all ferromagnetic material, however, hard magnetic materials are not ideal as they require near zero hysteresis for high working efficiency. In 1997, Percharsky et al. discovered the use of Gd metal and later $Gd_5Si_2Ge_2$ as MR material that have sparked the interest among researchers for the observance of giant magnetocaloric effect (GMC) at room temperature.[9-10] Although Gd based material have shown to be a promising MCE material, it is expensive (~$4000 per kg) and prone to oxidation over time.[11] Therefore most of the current research has been focused on finding new materials that is more cost effective for MR technology. Alternatively, ferromagnetic perovskite maganites ($R_{1-x}M_xMnO_3$, R = La, Nd, Pr, and M = Ca, Sr, Ba, Na, etc) have been of interest as they have shown large MCE in the room temperature range.[12] However, the MCE of these materials are still inferior to Gd based compound.

1.2.Magnetic Properties

Magnetic nanoparticles are used in a variety of products such as catalysis, drug delivery, magnetic data storage, and refrigeration applications. The high surface-to-volume ratio of

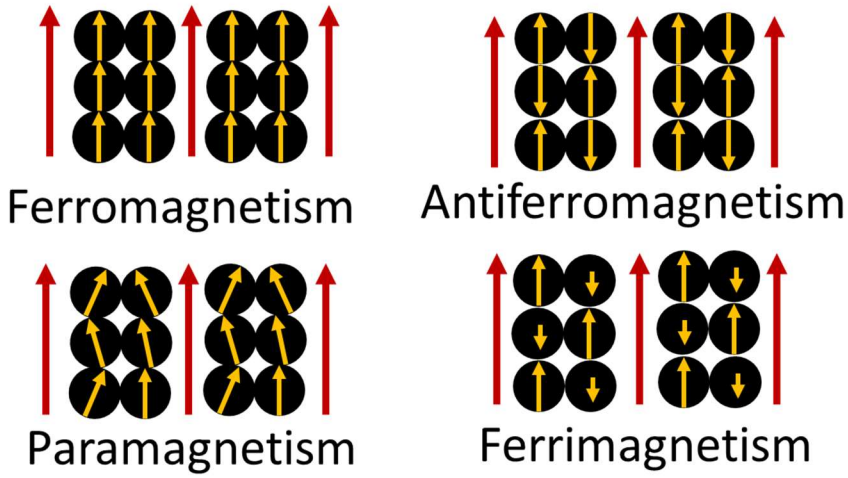

Figure 2. Types of magnetism observed in materials. Red arrow represent the direction of the applied field (H), yellow arrow represent electron spin direction.

nanoparticles are attractive as its surface and physical property can be easily modified. The electron configuration of atoms and molecules determine its magnetic properties. Particularly, the presence of unpaired electron in the outer shell of an atom can be determined from its magnetic properties. Materials behave differently under the presence of a magnetic field. Some materials will be attracted to a magnetic field, where it will then become magnetized and behave differently to the surrounding environment. In general, there are five different types of magnetism: diamagnetism, paramagnetism, ferromagnetism, antiferromagnetism and ferrimagnetism.

1.2.1.1.Diamagnetism

Diamagnetism occurs when atoms contains spin paired electrons replaced under a magnetic field resulting in the repulsion from the field. Diamagnetic materials are also known as non-magnetic materials. Examples of a magnetic material include copper, water, silver, mercury, and wood. Interestingly, diamagnetic materials are great superconductors as it can repel most fields.

1.2.1.2. Paramagnetism

Paramagnetism occur when atoms and molecules contain one or more unpaired electrons. In paramagnetic materials, electron spins are randomly oriented, however, with an applied field their moment tend to align to the direction the field. The electron spins of magnetic material are randomly oriented in the absence of a magnetic field, when a field is applied the magnetic moment align to the direction of the field as well. However they are typically slightly misaligned as a result of the thermal energy barrier as demonstrated in Figure 2. This type of alignment results in attraction of the material toward the applied magnetic field. Paramagnetism is dependent upon the temperature of the material.[13] When a paramagnetic material is being cooled below its Curie temperature, ferromagnetic behavior can be observed. A special type of phenomenon called the magnetocaloric effect relies on the ferromagnetic to paramagnetic transition at Curie temperature will be discussed in section 1.2.1.4.

1.2.1.3.Ferromagnetism, Antiferromagnetism, and Ferrimagnetism

Ferromagnetic materials have a wide industrial importance as they can be used in permanent and electromagnetic applications. Ferromagnetism is observed when the unpaired electrons in a paramagnetic material align parallel to its neighboring spin in the absence of an applied field. This typically occurs below the Curie temperature of a paramagnetic material. In a ferromagnetic material the maximum derivative of the susceptibility over temperature is defined as Curie temperature. Below the Curie temperature of a magnetic material, the susceptibility becomes field dependent. Unlike ferromagnetism, antiferromagnetism is observed when the neighboring spins are antiparallel direction to each other. This type of behavior is usually observed under the Neel temperature where the material exhibits no magnetic response to an applied field. [13] Above the Neel temperature, some spins will align in response to an applied magnetic field.

Ferrimagnetism is observed in a material when the spins are antiparallel to each other, they are also of different magnitude. As a result, a spontaneous magnetization remains in the material.

1.2.1.3.1. Properties of ferromagnetic materials

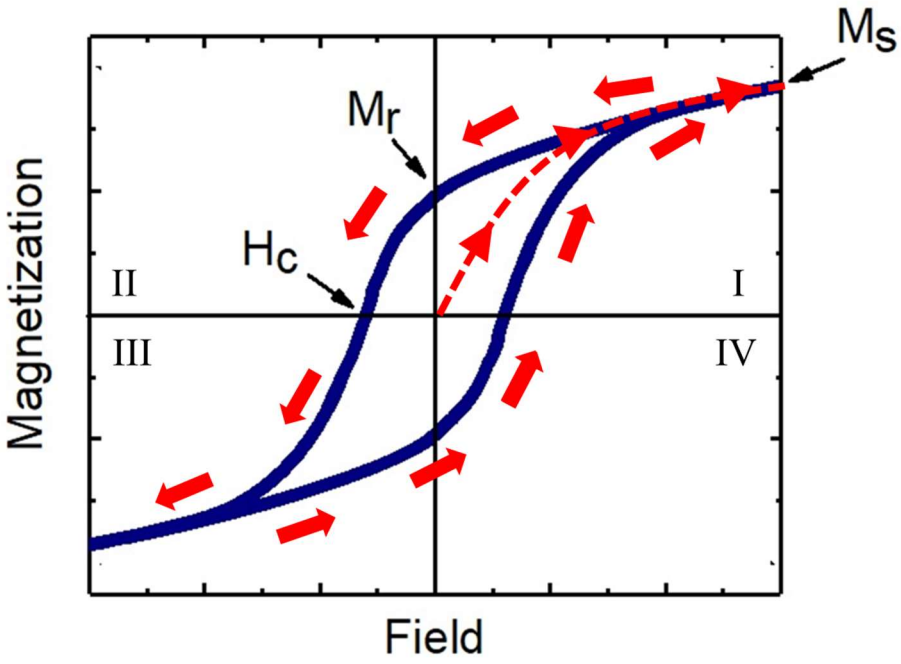

Figure 3. Magnetic hysteresis loop showing the relationship between magnetization as a function of magnetic field in a ferromagnetic material.

Ferromagnetic materials possess nonlinear magnetization response under an applied field. The formation of magnetic domains causes three main characteristics of a ferromagnetic material: magnetic saturation, magnetic remnants, and magnetic coercivity. The evaluation of these properties of ferromagnetic materials can be achieved by measuring a hysteresis loop as demonstrated in Figure 3. In the first quadrant, maximum magnetic saturation (Ms) of a material is observed under a high applied field as a result of all the unpaired spin aligning in the direction of the applied field. As the applied field decreases, this result in a decrease of magnetic saturation. When the applied field reaches zero, magnetization is still retained in the ferromagnetic material

called magnetic remnant (Mr) or residual magnetism. In order to randomize the magnetic spin in a ferromagnetic material, there are energy barriers known as the coercive force must be overcome until the material becomes demagnetized at this point.

1.2.1.3.2. Hard and Soft Ferromagnetic Materials

There are two types of ferromagnetic materials hard and soft magnets. The evaluation of the magnetic properties of these magnetic materials are from measuring the hysteresis loop as demonstrated in Figure 4. Soft magnetic materials is characterized by a small coercive force and magnetic remnants which make them easy to be magnetized and demagnetized. Since they are easily magnetized with high magnetic polarization and low magnetorestriction properties, they are excellent candidates for medical applications such as magnetic hypothermia treatment and drug delivery.[13] Examples of soft magnetic material includes iron, nickel and their alloys. Soft magnets are not suitable as permanent magnet or magnetic storage material as those applications require a large permanent magnetization by an external field that will not suffer hysteresis loss overtime.

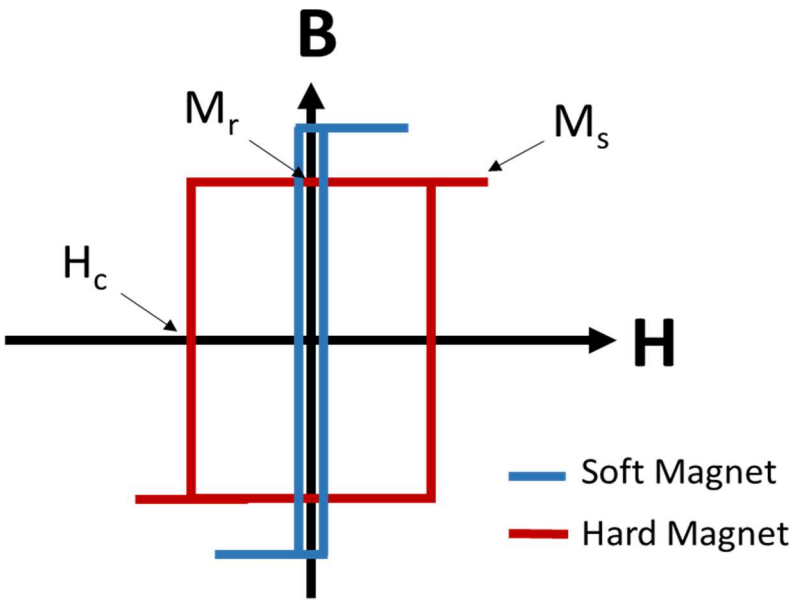

Figure 4. Magnetic hysteresis curve for hard and soft ferromagnetic materials.

Hard magnetic materials typically have a square hysteresis loop. They are good candidates as permanent magnet materials as they are hard to demagnetize once they are magnetized by the applied field. The ability for magnetic storage relies on the energy product (BH_{max}) of a hysteresis loop. A hard magnetic material for magnetic storage application should be strong enough to produce a measurable effect for recording, but not too strong that it becomes irreversible.

1.2.1.3.3.Magnetic Anisotropy

In a ferromagnetic or antiferromagnetic material, there is an easy axis for hard magnets. The easy axis of a material is the crystallographic direction that ferromagnetic or antiferromagnetic is oriented under the absence of an applied magnetic field. There are several properties that play a role in the magnetic anisotropy of materials, this includes crystalline structure as well as the shape of the particles. A strong magnetic anisotropy is important for permanent magnet applications. Magnetocrystalline anisotropy is a property that is observed within a material where the maximum magnetization is different along a certain crystal plane. In magnetic nanoparticles, shape anisotropy plays an important role as the morphology of the particles can be altered in order to minimize the demagnetizing field within a particle.

1.2.1.3.4. Permanent Magnetic Materials

As mentioned in the previous chapter, hard magnetic materials are typically used as permanent magnets for storage purposes. This is because of their large coercive force making them hard to be demagnetized once they are magnetized by an external field. Table 1 shows some examples of permanent magnet materials and their magnetic properties. Samarium cobalt Sm_xCo_y, neodymium iron boride NdFeB, hexaferrites, and AlNiCo are among the most common hard magnetic materials. Among these magnets, Sm_xCo_y and NdFeB are rare earth based magnets that have excellent magnetic properties. These rare earth magnets can be synthesized by cast melting,

high temperature sol-gel, or calciothermic reduction methods.[14-15] Cast melting of rare earth magnetic materials yields bulk materials, however the control over size of the as synthesized materials can be achieved by the calciothermic and sol gel methods. Calciothermic reduction methods involve the reduction of metal oxides precursor salts using calcium as a reducing agent under an inert atmosphere to prevent oxidation.[14] As demonstrated in table, Nd-Fe-B type magnets possess the highest maximum energy product and highest magnetization making it most efficient in magnetic storage applications. This is due to the spin-orbit coupling properties between Fe and Nd resulting in a favorable exchange between the two elements. However, the high temperature stability of Nd-Fe-B is unstable and it is easily demagnetized at high temperature.

Table 1. Magnetic properties of selected permanent magnet materials. Adapted and modified from ref 13.

Material	Curie Temperature T_c (K)	Saturation Magnetization (emu/g)	Maximum Energy Product BH_{max} (MGOe)
$Nd_2Fe_{14}B$	588	128	64
$SmCo_5$	838	97	28.9
$Sm_2Fe_{17}N_3$	749	123	59
Sm_2Co_{17}	838	86	36.8
AlNiCo 5	1210	135	5.5

As its name suggest, AlNiCo magnets are composed of Al, Ni, Co, and Fe. The exact composition depends on the grade of the magnet. Synthesis of AlNiCo mangets often involve cast melting or high temperature sintering methods. These type of magnets exhibit large intrinsic shape anisotropy as a result of the α_1 - FeCo phase in a non mangetic α_2 -NiAl based phase.[16] Hexaferrites are an interesting type of permanent magnetic materials. They are iron oxide based material most

commonly doped with Sr, Ba, and Pb. Due to their hexagonal structure in doped ferrets, they experience the magnetocrystalline anisotropy resulting in a hard magnetic material.

1.2.1.4.Magnetocaloric Effect

Magnetic refrigeration (MR) technology is based on the magnetocaloric effect (MCE). It is estimated that MR is an emerging technology where it is environmentally feasible as it can reduce our energy use by 30% without the use of conventional compressed gas refrigerants.[17] The magnetocaloric effect (MCE) was first observed in iron by German physicist E. Warburg in the 1880s.[18] MCE is defined as the temperature change in the material upon a change in magnetic field.[12] It is based on the thermodynamic correlation of reversible change in magnetic entropy in

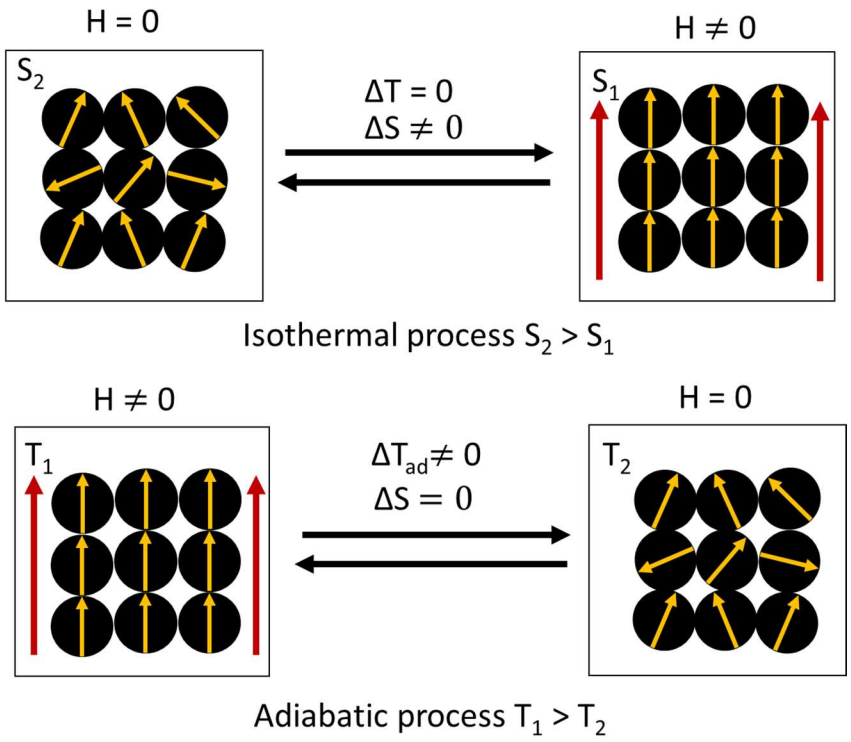

Figure 5. Magnetocaloric effect when magnetic field is removed or applied. Red arrow represent direction of the applied field, yellow arrow represent the electron spin.

an isothermal process defined using the Maxwell relations[19] $\Delta S_M(\Delta H) = \int_{H_1}^{H_2} \left(\frac{\partial M}{\partial T}\right)_H dH$ where ΔS_M is the change in magnetic entropy, ΔH is the change in applied field, M is the magnetization, and T represent temperature.

Materials that exhibit MCE typically experience a coupling between its crystal structure and magnetism where a change in magnetic and lattice entropy is observed under an applied magnetic field. In principle, all ferromagnetic magnetic material exhibit some type MCE. However, the material chemistry, lattice structure, and electronic state of the material plays an important role in the determination of MCE properties. In addition, temperature change has a significant influence on the electron distribution and lattice vibration properties within a magnetocaloric material (MCM).[12] Figure 5 shows four main steps in MCE observed in a material. When a magnetic field is applied to MCM under an isothermal process, all magnetic spins will align parallel to the applied field decreasing the magnetic entropy of the system. Similarly, when the applied field is removed, the magnetic entropy in an isothermal process increases. In an adiabatic process, when a magnetic field is applied, the temperature of the MCM increases as a result of the decreases in magnetic entropy to balance the increase of lattice entropy of the material.[17] Similarly, when a magnetic field is removed from the material, magnetic entropy increases and the temperature of the material decrease.

MCE can be measured directly and indirectly. Due to the instrumental limitations provided at the time, the MCE results reported in this dissertation are obtained indirectly. There are two ways to measure MCE indirectly, by measuring the magnetization as a function of temperature and magnetic field or heat capacity as a function of temperature and applied field. It is important to note that when comparison is made for different classification of MCE materials, the results

may be biased as adiabatic temperature change is an intensive property where magnetic entropy is an extensive property, making them very complex to compare directly.[20]

1.2.1.4.1.Relative cooling power

The efficiency of a magnetocaloric material for MR is evaluated by calculating its relative cooling power (RCP). RCP measures the maximum entropy change in an ideal refrigeration cycle, it is determined by multiplying the maximum entropy change ΔS_M (max) by the change in temperature at full width half max of a temperature dependence of magnetic entropy curve as demonstrated in Figure 6. In similar fashion, Maximum RCP with respect to adiabatic temperature change can be calculated by multiplying the change in maximum adiabatic temperature and the full width half max.

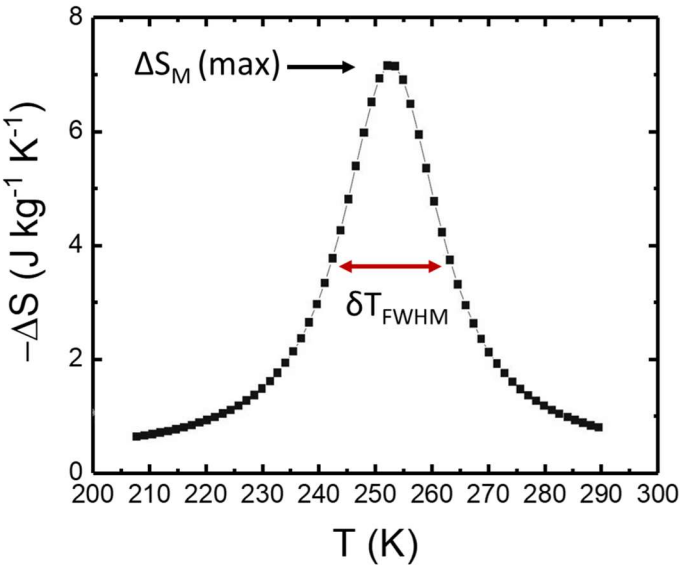

Figure 6. Example of temperature dependence of magnetic entropy curve for the determination of relative cooling power.

1.2.1.4.2. First and second order phase transition

First order phase transition is characterized by a discontinuous change in entropy at constant temperature. In this system, two phases are in equilibrium resulting in and discontinuous

face transformation showing a discontinuity in magnetisation and entropy. It has been shown in the literature that first order phase transition can be limiting in refrigerator performance. This is mainly due to the slow kinetics of the phase transition in addition to the possible existence of thermal and magnetic hysteresis.[11] However, it has been suggested that the purity of the material contribute to a more refined microstructure, leading to a smoother and faster first order magnetic phase transition.[21]

Unlike first order phase transition, second-order phase transition it's characterized by the continuous change from one phase to another without the presence of an equilibrium between the two phases. This type of transformation is kinetically faster in comparison to first order transformation making it more desirable for refrigerator performance.

Banerjee criterion plots can be used to evaluate the order of phase transition.[22] This can be achieved by plotting H/M vs. M^2 near the transition region. Based on the thermodynamics of magnetic phase transformation, first order phase transition is characterized by the negative slope, whereas second-order phase transition is characterized by the positive slope of the Banerjee plot.[23]

1.2.1.4.3.Material properties for magnetic refrigeration

As mentioned previously, all magnetic materials show magnetocaloric effect to some extent. However, not all materials are suitable for magnetic refrigeration. Below are some characteristic properties of potential candidates for magnetic refrigeration technology:

- Large magnetic entropy along with a large adiabatic temperature range
- Small thermal hysteresis for better reversibility
- Near zero hysteresis for higher working efficiency
- Large electrical resistance
- High chemical stability

- Low production cost for commercialization purposes

In addition to large entropy and adiabatic temperature change, physical properties of the magnetic refrigeration materials is also an important factor in the commercialization of these materials.

1.2.1.4.4. Current Magnetocaloric Materials

Since the MCE was first observed in iron by Warburg in the 1880s, MCE materials have made a significant progress.[18] The most significant progress in MCE materials was made in 1997 by Pecharsky et. al. in the discovery of near room temperature giant magnetocaloric effect in Gd and $Gd_5(Si_xGe_{1-x})_4$ (ΔT_{ad} = 3.3, ΔS_M = 3.1 J^{-1} K with ΔH = 1T for Gd) .[17, 24] Gd was the first element to show a ferromagnetic to paramagnetic transition near room temperature, its Tc is dependent upon its purity. However, its heat capacity is lower in comparison to other Gd based alloy, where the T_c can be tuned. This discovery has sparked interest among the scientific community in the development of alternative refrigeration material. Materials that exhibit giant MCE typically have a large lattice entropy change under an applied field causing a structural transformation with or without symmetry change within the material.[10, 19, 24-25] For instance, the origin of MCE in $Gd_5Si_2Ge_2$ is due to its magneto structural transformation from the monoclinic paramagnetic phase to its orthorhombic ferromagnetic phase.[9, 26] In addition, the transition temperature of $Gd_5Si_2Ge_2$ was found to be strongly dependent upon the Si doping in its structure.[26]

Over the years, many efforts have been made to seek Gd free elements that exhibit a large MCE near room temperature in order to reduce the cost of production. Efforts have been made to explore compounds such as $LaFe_{13-x}Si_x$, $MnFeSi_xP_{1-x}$, Heusler alloys, manganites, and nanocrystalline alloys. In $LaFe_{13-x}Si_x$ systems with Si $x \leq 1.6$ its paramagnetic to ferromagnetic transition at temperature near its Curie temperature. However, above its Curie temperature it is an

Table 2. List of current mangetocaloric materials and its magnetic properties.

Sample	$\lvert(\Delta S_M)_{max}\rvert$ (J kg^{-1} K^{-1})	ΔH (T)	T_c (K)	Reference
$LaFe_{11.6}Si_{1.4}$	8	2	200	[27]
$Ni_{51.5}Mn_{22.7}Ga_{25.8}$	4.1	0.9	351	[28]
$Mn_{1.25}Fe_{0.7}P_{0.5}Si_{0.5}$	9	1	274	[29]
Gd	4.0	1	295	[30]
$Gd_{90}Fe_{5.7}Al_{4.3}$	7.2	5	279	[31]
$Gd_5Si_2Ge_2$	6.5	1	277	10
$Gd_{4.9}Sc_{0.1}Si_{1.8}Ge_{2.2}$	19	2	248.4	[32]
$Fe_{75}B_{12}Cr_8Ce_5$	1.1	1.8	295	[33]
$La_{0.5}Ca_{0.5}MnO_3$	1.2	2	210	[34]
$La_{0.6}Ca_{0.4}MnO_3$	8.3	5	270	[35]
$La_{0.8}Ca_{0.2}MnO_3$	8.6	4.5	236	[36]
$LaMnO_3$	2.4	5	150	[37]
$La_{0.75}Sr_{0.25}MnO_3$	1.6	1.5	332	[38]
$La_{0.925}Na_{0.075}MnO_3$	1.32	1	195	[39]

electron metamagnetic transition.[40] It has been shown that in the $LaFe_{13-x}Si_x$ alloy system, the transition can be altered by changing the Si content of the system. First order transition is observed in Si $x \leq 1.6$ whereas a second order transition is observed in Si $x > 1.6$. Several attempts have been made in altering the transition of this material in which hydrogen insertion into the $LaFe_{13-x}Si_x$ structure as well as the introduction of a mismatched metal have shown to preserve the weak first order transition in this system.[41-42] $LaFe_{13-x}Si_x$ type materials have shown to be an economical choice as MR material as they are inexpensive and can be easily scale up for manufacturing

purposes. However, the relative cooling power is smaller than Gd in comparison, and addition surface treatment of the material to prevent surface corrosion of the material.

Heusler alloy is a family of materials discovered in 1903 with X_2YZ formula where X is a transitional metal, Y is a rare earth or alkaline rare earth metal, and Z is from group IIIA-VA. This alloy consist of ternary intermetallic compounds where the full Heusler have the L_{21} crystal structure and semi Heusler are C_{16} crystal structure. The first Heusler alloy that was reported to exhibit the MCE in Ni_2MnGa.[28] The mangetic entropy change in Heuler allow is due to martensitic transition in which the crystal structure of the material transforms from martensite to austensite under a certain temperature and magnetic field resulting in a strong first order magnetic transition.[43-45] Heusler alloy is an interesting family of alloys as inverse MCE, magnetic superelastic behavior along with magnetic field induced strain have been observed in this material.[46] Inverse MCE has been observed in NiMnZ (Z=Sn, In, Sb) materials where material cools when a magnetic field is applied adiabatically and the entropy increases as the magnetic field is applied, resulting in a positive magnetic entropy value.[43, 45-47] One of the major drawbacks for the use of Heusler alloy for MR application observed is its large thermal hysteresis. Irreversible phase transformation occur upon cooling of the material in which the paramagnetic martensite will not transform back to the ferromagnetic austensite phase in the absence of a strong applied field.

Perovskite type ferromagnetic manganites $R_{1-x}M_xMnO_3$ (R = rare earth, M = Ca, Pb, Na, Ba, Ag, Sr, or K) have shown to be a promising MCE material as they have exhibited large MCE near room temperature. The MCE in perovskite is originated from the lattice distortion from the cubic structure where the bonding of the MnO_6 octahedron is deformed to rhombohedra or orthorhombic crystal structure.[12] In addition, Jahn-Teller distortion as a result of the Mn^{4+} and Mn^{3+} coupling in the MnO_6 octradehron can also give rise to the MCE in magnanites.[12, 48] The

structural, electrical, and magnetic properties of this type of material can be changed by the M and Mn site substitution with different metals. In the manganite family, $La_{1-x}Ca_xMnO_3$ have shown to exhibit the largest MCE, however, its critical temperature is below room temperature. Literature have shown that the replacement of Ca by other metals (Sr, Pb, Ba etc.) can lead to a higher transitional temperature. In order to overcome this issue, Ni, Co, Cu, Ti, and Cr can be doped in order to substitute the Mn^{3+} content within the perovskite structure.

Chapter 2: Synthesis Techniques

2.1.Nucleation and Growth

The synthesis of nanoparticles in solution occurs in two steps: nucleation and growth. When nucleation and growth occur simultaneously, polydispersity is observed in the resulting particles. The particle formation kinetics was not well understood until LaMer and Oswald's work in the 1890s. LaMer suggested that crystallization is a diffusion driven process that occur in multiple steps as shown in Figure 7.[49] At stage I, precursor decompose and nucleation is thermodynamically allowed, forming monomers until it reaches a critical supersaturation concentration. At stage II, burst nucleation occur and forms stable nuclei, however, the concentration of monomers at this point will start to decrease and nucleation stops while remaining above the supersaturation limit. Over time the concentration of monomers will fall below the supersaturation limit and Oswald ripening occurs in which the monomers will start to grow. Small nuclei exhibit high surface to volume ratio, where the surface of the nuclei govern the free energy of the crystal growth. In comparison, bulk free energy governs the growth of large nuclei.[49-50] It is important to note that nucleation occurs homogeneously as well as heterogeneously. Homogeneous nucleation only occurs when the Gibbs free energy is negative.[50] The energy

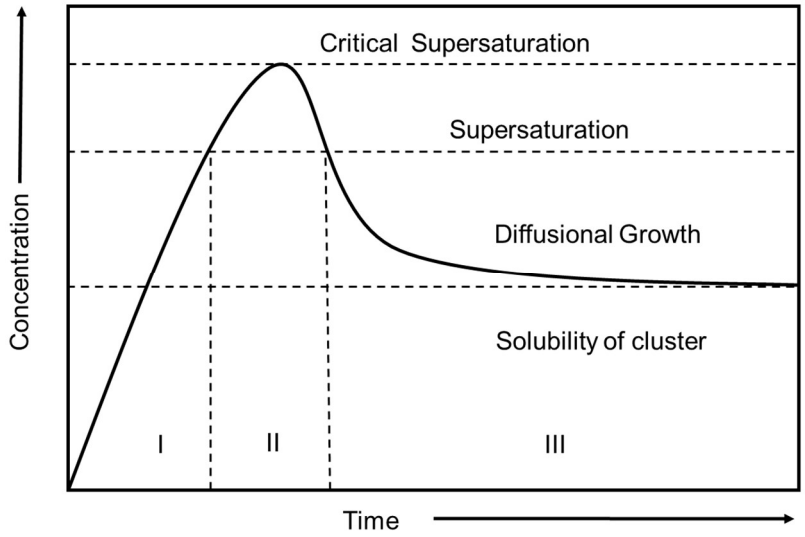

Figure 7. Nucleation and growth of particles.

requirement of homogeneous nucleation is high since it involves the formation of a new surface. On the other hand, in heterogeneous nucleation, the nuclei is growing on a preexisting surface such as thin films or support, consequently the energy requirement is comparatively lower than homogeneous nucleation.[50]

2.2. Synthesis of Nanoparticles

2.2.1. Choice of Precursor

The choice of metal precursor is an important process in the synthesis of nanoparticles as it can alter the nucleation and growth of crystals by modifying the surface energy with ligands. This is mainly due to the difference in metal to ligand bond strength where some metal ligand bonds require more energy to break than others. The strength of the bond can be explained in hard soft acid base theory as well as spectrochemical series.[51] In the hard soft acid base (HSAB) theory, metals and bases are categorized into hard and soft. In general, metals and ligands that are classified as hard acids and bases have a small atomic radii, with high charge density, and low polarizability. On the other hand, metals and ligands with soft acids and bases characteristics have larger atomic radii, low charge density, and more polarizable. Typically, hard acids preferably bond with hard bases and soft acids preferably bond soft bases. Therefore the bond between and hard acid and soft acid is stronger than a bond formed between a hard acid and soft base.[51]

2.2.2. Heat-up synthesis

Heat up synthesis of nanoparticles is a popular method to obtain semiconductors, metals, ceramic, and non-metals nanoparticles. As its name suggest, heat up method involves heating metal precursor salts in a high boiling point organic solvent. The metal precursor will then dissociate and reduced at elevated temperatures resulting in nanoparticles as a product. Heat up

synthesis allows control over the nucleation and growth of nanoparticles by altering metal salts, solvent, reducing agent, temperature, and surfactants. The heat-up synthesis method is versatile and can be adapted in the synthesis of semiconductors, inorganic metal oxides, carbides, and nitride nanomaterials have also been reported in the literature shown in Table 3.[50] It is important to note that in the solution based synthesis of nanocrystals, the heating rate, and precursor reactivity have a strong effect on the final size, shape, and size distribution of the product.

Table 3. Selected sample of heat up synthesis conditions.

Material	Temperature / reaction duration	Chemistry	Size / morphology	reference
CoO	200 °C / 1-3 hr	$Co(acac)_3$, OLA	40 nm / rods	[52]
NiS	150-190 °C / 5-300min	$Ni(OctA)_2$, DDT	6-20 nm / tetrahedral, rods	[53]
CeO_2	200 °C / 2 hrs	Ce-oleate, TD	60-90 nm / spheres	[54]
Fe_3C	365 °C / 45 mins	$FeCO_3$, OLA, CTAC	50-200 nm / spheres, plates	[55]
Co_9S_8	250 °C / 10 mins	$CoCl_2$, TOP, DDT, OLA	18 nm / faceted	[56]
In_2S_3	300 °C / 2 hrs	$InCl_3$, S, OLA	22 – 63 nm / discs	[57]

*OLA=Oleylamine, DDT = Dodecylthiol, TD=Tetradecene, CTAC= Cetyltrimethylammonium chloride

2.2.2.1. Polyol Process

The polyol method was first reported by Fievet et al. in 1989 for the synthesis of elemental metal (Cu, Ni, Co) and metal alloys.[58-59] The polyol method is a variation of the heat up synthesis method where metal salts are suspended in a high boiling point polyhydric alcohol solution and heated to elevated temperatures to encourage the interaction of the precursors during synthesis resulting in nanoparticles with various sizes and morphologies. Polyol method is a versatile approach to synthesizing elemental metal, metal oxides, carbides, chalcogenides, and non-metal main group elements.[60-63] It is a straightforward process in comparison to some other high temperature synthesis involving organometallic compounds. Polyol typically refers to a polyhydric alcohol such as glycol, ethylene glycol, 1,2 – hexadecadiol. In a typical polyol process, metal precursor salts (nitrates, chlorides, acetates, carboxylates etc.) are dissolved or suspended in a selected polyol solution, the solution is then heated up to the boiling temperature of the polyol between 120-300 ºC for an extended period depending on the desired physical property.[58-59, 64-67] The reduction of metal in polyol solution occur upon the dissociation of metal salt in solution at elevated temperatures, forming an intermediate to reduce the metal through a redox pathway, followed by the nucleation and growth of particles.[58-59, 65] The polyol solution acts as a solvent, reducing agent, and stabilizing agent to control the nucleation, growth, and surface properties of the particles.

The type of metal precursor, concentration of base, reaction temperature, and the type of polyol plays an important role in the reduction potential of the solution. Table 4 shows commonly used polyol and its boiling point. The selection of polyol depends upon the metal of interest. Typically, easily reducible metals can be reduced by using a low boiling point polyol (<200 ºC), however, less noble metals require higher boiling point polyol (>200 ºC) or with the presence of

additional reducing agents.[60] To overcome the issue with less noble metals, a metal seed can be introduced in order to control the reduction kinetics.[5, 68] In more recent years, the polyol method has extended to metal carbides (Ni_3C, Co_2C, Co_3C) and they have shown interesting properties.[69-70] These types of transitional metal carbides can be used in various applications such as catalyst for hydrogen evolution reactions (HER), hard magnetic, and sensing applications.[71]

Table 4. Common polyols and its properties.

Type of polyol	Abbreviation	Structure	Molecular weight (g/mol)	Boiling point (°)
Glycerol	/	$HOCH_2CH(OH)CH_2OH$	92.1	290
1,2 - hexadecadiol	HDD, HDIOL	$C_{16}H_{34}O_2$	258.4	356.1
Ethylene glycol	EG	$OH(CH_2)_2OH$	62.07	198
Triethylene glycol	TEG, 3-EG, TriEG, TREG	$HOCH_2(CH_2CH_2O)_2CH_2OH$	150.2	285
Tetraethylene glycol	TEG, 4-EG	$HOCH_2(CH_2CH_2O)_3CH_2OH$	194.2	327.3
Propylene glycol	PG	$C_3H_8O_2$	76.1	188.2

2.2.3.Sol-Gel Synthesis

The sol-gel process is a wet chemical process where a colloidal suspension of inorganic precursor or polymer (sol) through a series of hydrolysis and condensation reactions to obtain a continuous network of structure (gel). This process started in the 19th century by Jacques Joseph

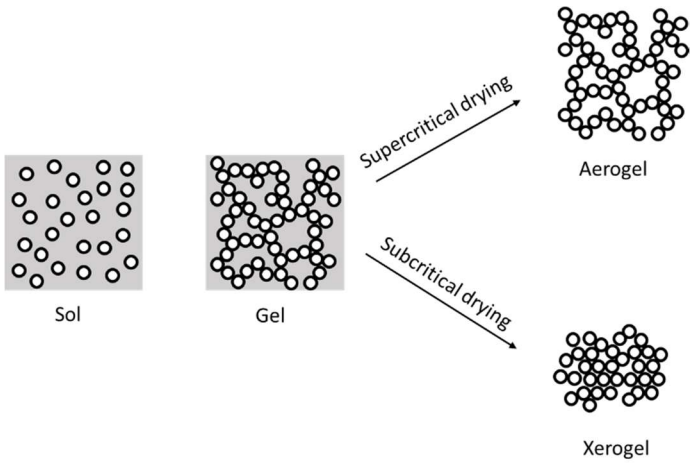

Figure 8. Various drying method of gel.

Ebelman and Thomas Graham for the development of glass-like ceramic material through a series of hydrolysis and condensation of tetraorthosilicate (TEOS).[72] The sol-gel process can be thought of as a series of steps: formation of sol, gelation, aging, drying, and densification.[73-74] Each of these processes, prior to the drying step, is reversible. The sol can be obtain by hydrolysis and condensation reaction where its kinetics is pH dependent. At low pH, hydrolysis is favored where condensation is the rate determining step. On the other hand, at high pH, condensation is favored and hydrolysis becomes the rate determining step in this process.[75] The resulting pore size of the gel is dependent upon the length of the gelation process where the longer the gel is allowed to age, the sols become more interconnected due to the polycondensation reactions resulting in the removal of solvent within the gel forming a dense monolithic structure.[76] The final step of the sol-gel process involves the removal of solvents. This step is critical in the determination of the density and surface area of the product. Supercritical drying using CO_2 will result in a high surface area and low density gel also known as aerogel whereas subcritical drying in ambient environment will lead to pore shrinkage resulting in a dense gel known as xerogel.[77-78]

Throughout the years, the sol-gel method has extended to the synthesis of metal and metal oxides.[79-81] In general, any metal and its oxides can be prepared through the sol-gel process.

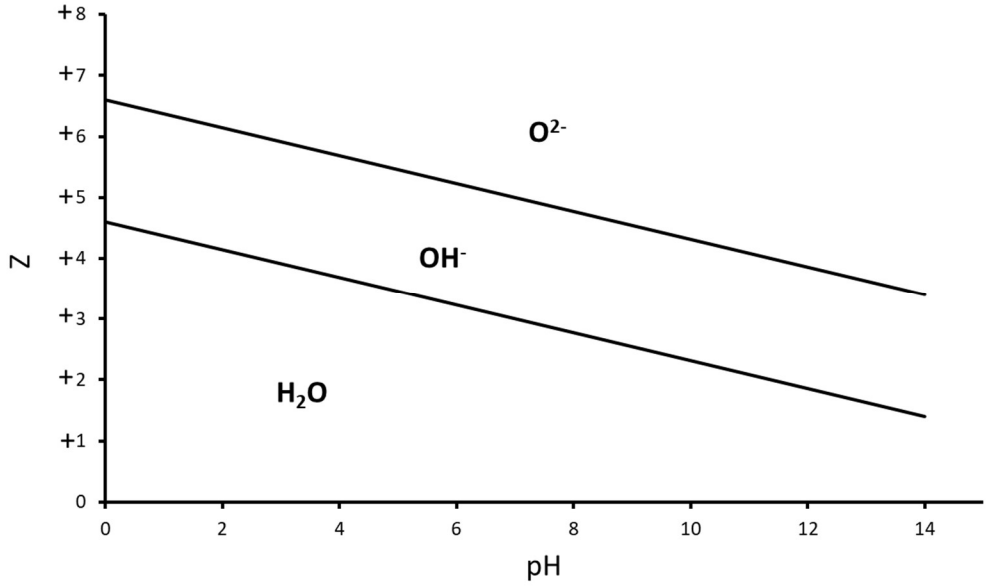

Figure 9. Charge pH diagram indicating OH^-, H_2O, and O^{2-} species.

Typically, metal-organic precursor salt is used in the sol-gel synthesis since they have a tendency to become solvated by the surrounding water molecules.[81] Condensation of metals involves the formation of M–O–M species that require the M–OH where it can be obtained by adjusting the pH of the solution shown in Figure 9.[74] Alternatively, M–O–M can also be obtained through heating the sol at elevated temperatures to promote the condensation reaction.

2.2.3.1. Pechini method

The Pechini method is an extension of the sol-gel process where it utilizes a polymer matrix to obtain metal particles. This method allows the synthesis of mixed metal compounds that are not suitable for sol-gel reaction due to unfavorable hydrolysis equilibra by elimating the formation of M–OH species. The formation of metal or non-metal complexes with chelating agents such as ethylenediaminetetraacetic acid (EDTA) and citric acid.[82-83] This process provides homogeneity in the as-synthesized mixed metal particles as it converts the metal precursor materials into a polymer matrix to entrap metal ions slowing the decomposition rate.[82] In a typical Pechini process,

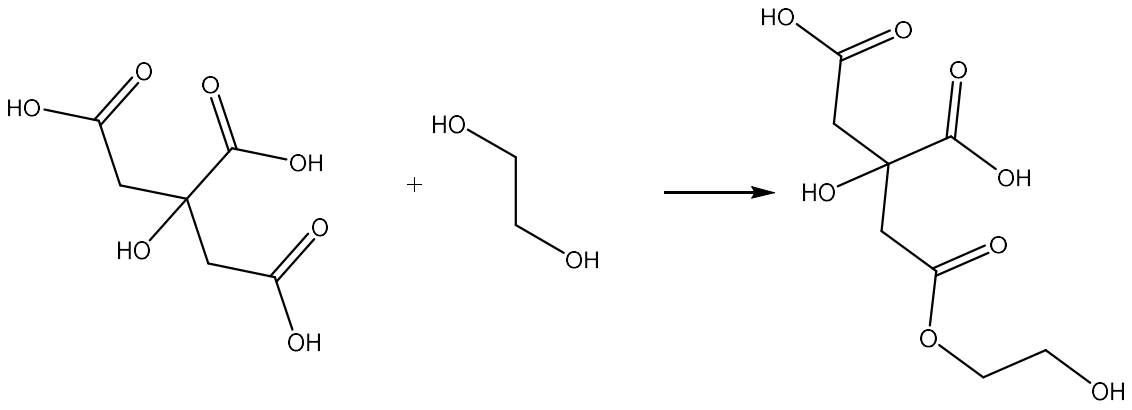

Figure 10. Schemtic of transesterification of citric acid and ethylene glycol.

metal precursor salts are dissolved in a solution containing citric acid and ethylene glycol. The solution is heated in order to initiate the formation of metal citrate complex as well as transesterification between citrate and ethylene glycol as shown in Figure 10.[84] It is to be noted that while the Pechini method is versatile in the synthesis of mixed metal ceramic materials, it is sensitive to pH as low pH will stabilize the citric acid keeping it protonated while high pH environment will result in the formation of metal hydroxides.

Chapter 3: Characterization Techniques

3.1.Introduction

The characterization of nanomaterials is important to the development of new materials. This chapter aims to give an overview of a variety of techniques that are commonly used in the characterization of metal based nanomaterials in order to characterize chemical and physical properties of the materials of interest. Materials characterization is of importance in science and engineering fields as it applies to quality control, product development, impurities detection, failure analysis, and chemical effect of materials. This chapter will provide an overview of characterization techniques used in this work.

Table 5. Summary of characterization instrumentation and techniques.

Characterization Technique	Advanced techniques	Details
X-Ray Diffraction (XRD)	High Temperature XRD, Scherrer Analysis, Rietveld Analysis	Crystal phase identification, crystallite size determination, stability of phase,
Scanning Electron Microscopy (SEM)	Energy-dispersive X-Ray spectroscopy (EDX)	Elemental composition, particle size and morphology determination
Transmission Electron Microscopy (TEM)	Electron Diffraction, Election Energy Loss Spectroscopy	Particle size and morphology determination, elemental mapping for core-shell of individual particles
Dynamic Light Scattering (DLS)	Zeta potential	Hydrodynamic size determination of particles, colloidal, surface charge
Atomic Force Microscopy (AFM)		Surface roughness analysis
Fourier Transform Infrared Spectroscopy (FT-IR)		Chemical analysis of functional groups in solution or surfactants
Vibrating Sample Magnetometry (VSM)	Heat capacity measurement	Magnetic properties measurement
Thermogravimetric Analysis (TGA)	FT-IR	Thermal stability analysis of materials, FT-IR used for the analysis of the evolved gas

3.2. X-Ray Powder Diffraction (XRD)

X-ray powder diffraction (XRD) is a powerful tool to determine the crystal structure, phase identification, and chemical purity of a material. This method is non-destructive to the sample of interest, and it is a popular tool in determining the molecular structure of a crystalline material. When an x-ray enters a sample, it is then scattered by the electrons surrounding the atoms of the sample.[85] In crystalline materials, atoms are arranged periodically in a three-dimensional space allowing the scattering of electron through the crystal structure resulting in an increase intensity at a certain diffraction angle. On the other hand, amorphous materials lack the periodic arrangement where the atoms are randomly distributed within the material, as a result the X-ray that entered the sample will be scattered in many direction resulting in a large and broad peak in the resulting diffraction pattern. It is important to note that crystalline materials are required for powdered XRD analysis as amorphous materials lacks distinct diffraction pattern to be accurately identify its phase and composition, other characterization method will be required for amorphous material.

X-ray diffraction relies on the constructive interference as a result of the interaction between the x-ray and crystalline sample. In a typical analysis, the sample is under x-ray radiation at different angles, and at certain angle the incident ray and sample produce diffracted rays when the condition satisfies Bragg's Law:

$$n\lambda = 2d_{hkl}\sin\theta \quad (1)$$

where n is a positive integer, λ is the wavelength of the x-rays, d is the spacing between two crystal planes that contribute to the diffraction, θ is the incident angle of the x-ray. When the Bragg diffraction condition is satisfied, an increased intensity in the diffraction pattern will be observed. In cases where the Bragg condition is not satisfied, the resulting interference will be destructive with low observed intensity for the diffracted beam.

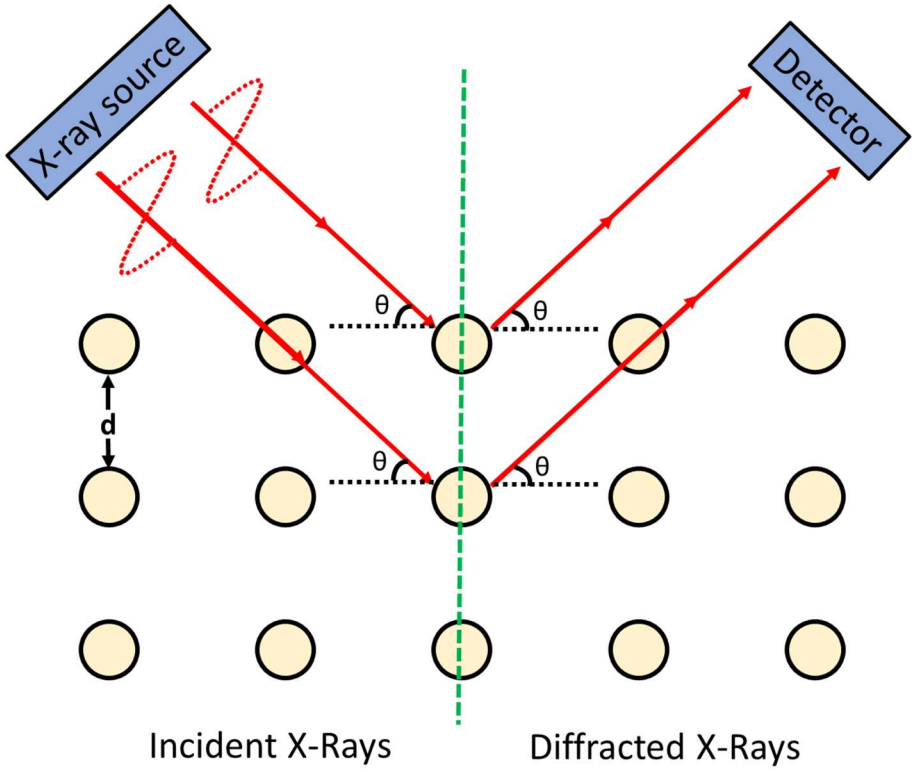

Figure 11. X-Ray diffraction of atoms within the surface of lattice structure.

Basic X-ray diffraction patterns analysis involve the comparison of diffraction patterns to known standards from the International center for diffraction data collection. However, more in-depth analysis is required to determine the lattice spacing, phase composition, and crystallite size of the sample.These methods will be discussed in the next sections.

3.2.1. Scherrer Analysis

The term particle size or grain size can be different in context in bulk and nanomaterials. In nanotechnology, it is important to know that in a nanomaterial particle size is used to describe each individual particles that is composed of small crystallites as shown in Figure 12. In a perfect

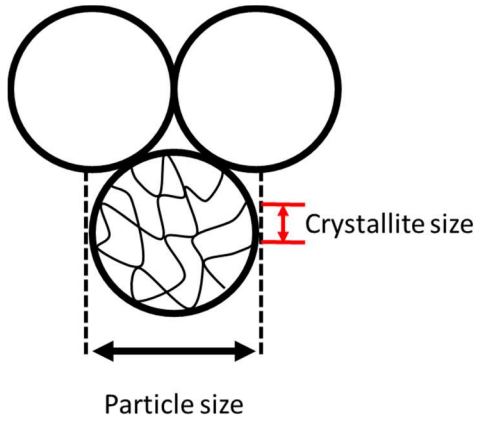

Figure 12. Diagram for crystallite size or grain size in a particle.

crystal, the distance between each plane should have the same lattice spacing. However, experimentally this is uncommon as the nanomaterial often experiences line broadening due to size effects, plastic deformation, or distorted lattice. Therefore it is important to determine the relationship between the peak widths with regards to crystallite size in a material. This relationship is known as the Scherrer analysis:

$$t = \frac{K\lambda}{FWHM\ cos\theta_B}$$

where t is the diameter of the crystallites, K is the Scherrer constant (K=0.9 for spherical particles), λ is the wavelength of the incident x-ray, θ is the diffraction angle. As shown in the equation above, the crystallite size is inversely proportional to width of a diffraction peak. As a result, Scherrer analysis is biased towards larger crystallites and assume model dispersed particle of the same morphology.

3.2.2. Rietveld Refinement

Rietveld refinement is one of the methods and analysis of X-ray diffraction patterns developed by Hugo Rietveld in 1967.[86] This method is still widely used in the full pattern phase analysis of X-ray diffraction patterns generated from various materials. This analysis method applies profile fitting method by minimalizing the square of the difference between the measured intensity and the calculated intensity. Information such as space group, lattice parameter, and atomic arrangement can be deduced from the refinement method. This method utilize the modeling of different lattice parameters along with the difference between phases within a sample, allowing the calculation of various phases within a sample. The calculated lattice patterns in this work are obtained from Pearsons Handbook of Lattice Spacing and calculated using X'Pert High Score Plus program.

3.3. Vibrating Sample Magnetometer (VSM)

Vibrating sample magnetometer as shown in Figure 13 is used to measure the magnetic properties of materials. Magnetic measurements in this work were measured by a Quantum Design Versalab physical property measurement unit. In a typical measurement, the sample is placed under a uniform magnetic field provided by two electromagnets. The sample is then vibrated along the z-axis of the instrument perpendicular to the applied magnetic field. The applied magnetic field causes the material to magnetize creating a magnetic flux along with an electric potential. This electric potential is then measured by the pickup coils that are attached to the electromagnets and surrounding the sample. This electrical potential generated by the vibrational frequency measured is directly proportional to the magnetic moment of the sample.

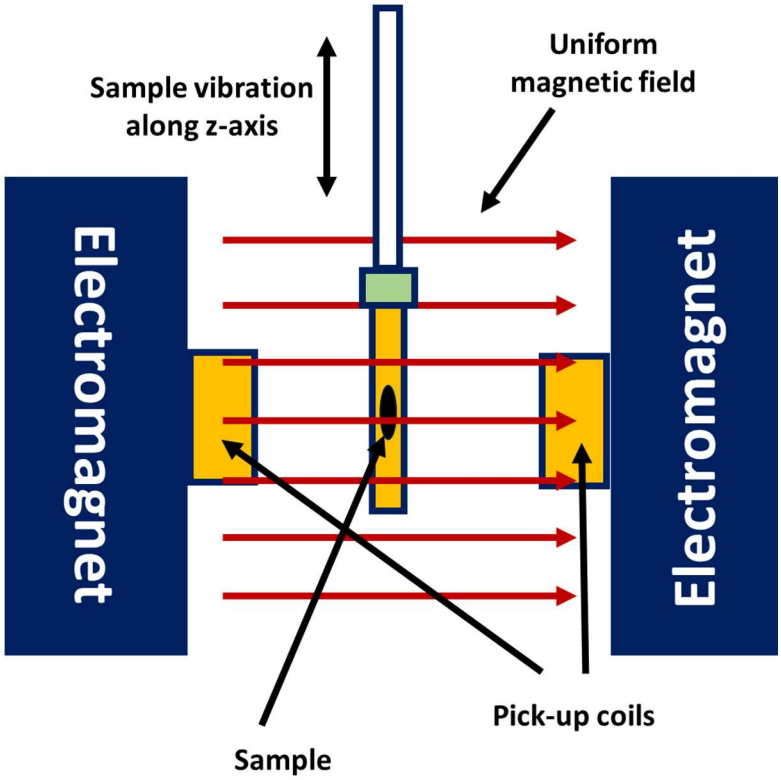

Figure 13. Typical schematic of vibrating sample magnetometer.

3.3.1. Magnetic Measurements

The most common magnetic measurements performed using a VSM unit is a room temperature isothermal magnetization (M-H) measurement. In this measurement, the magnetization of the material as a function of applied field is measured. Isothermal magnetization measurement is typically used to determine the type of magnetic properties (diamagnetic, paramagnetic, ferromagnetic, ferrimagnetic, or antiferromagnetic) within a material. When isothermal magnetization measurement is made in temperature increments, the magnetic entropy can be calculated by taking the difference of the area under the curve at each temperature increment. Another type of VSM measurement is the magnetization as a function of temperature (M-T). M-T curve can be used to measure magnetic transition, as well as temperature dependency of other interactions within in the material.

3.4. Scanning Electron Microscopy (SEM)

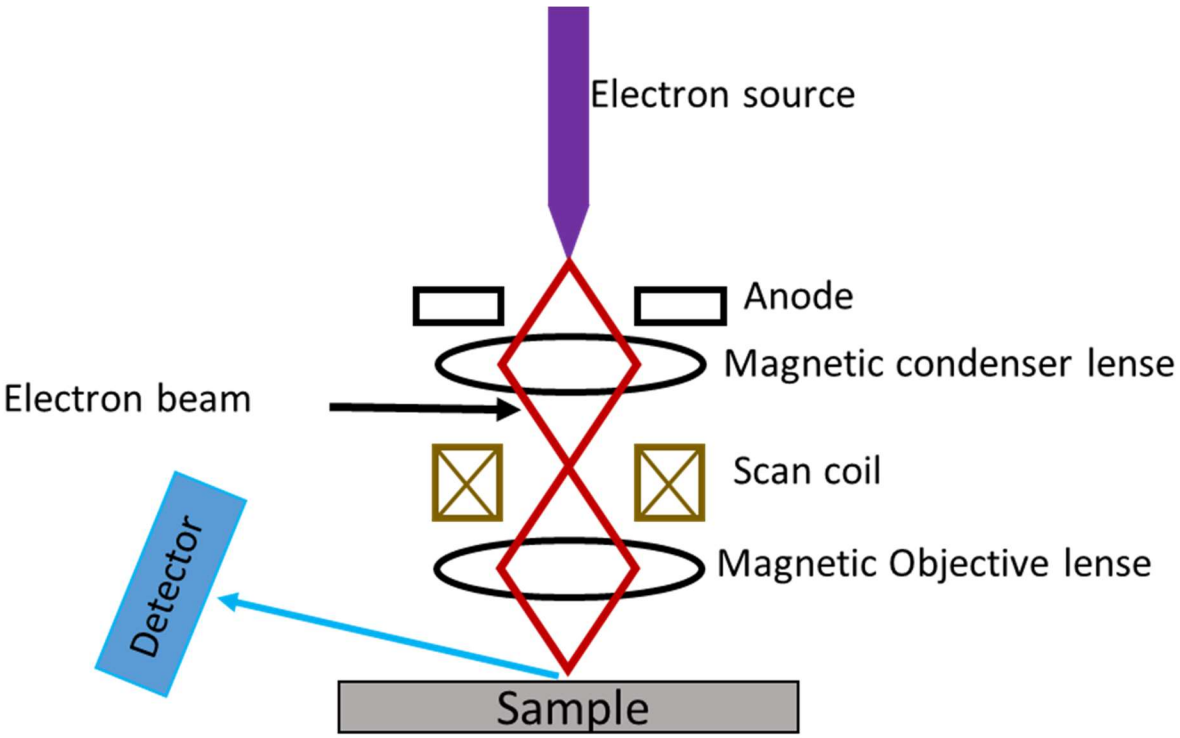

Figure 14. Schematic of a scanning electron microscope.

Scanning electron microscopy is a surface characterization technique used to determine the size and morphology of materials. As shown in Figure 14, it utilizes a focused electron beam typically generated by a tungsten filament that is accelerated to an energy a range of 1-40keV, the surface topography of the sample is generated by scanning in a rester pattern. When the electron beam interacts on a specimen sample, the surface will emit characteristic x-rays, backscattered electrons, secondary electrons, and auger electrons as shown in Figure 15. SEM is a non-damaging method for the analysis of samples, however, the sample must be electrically conductive or electrically grounded to prevent charge accumulation on the surface of the sample. Basic SEM imaging provides information on surface morphology and particle size irrelevant to

the sample thickness. However, more sophisticated SEM methods can be used to analyze the chemical composition and phase composition of the sample.

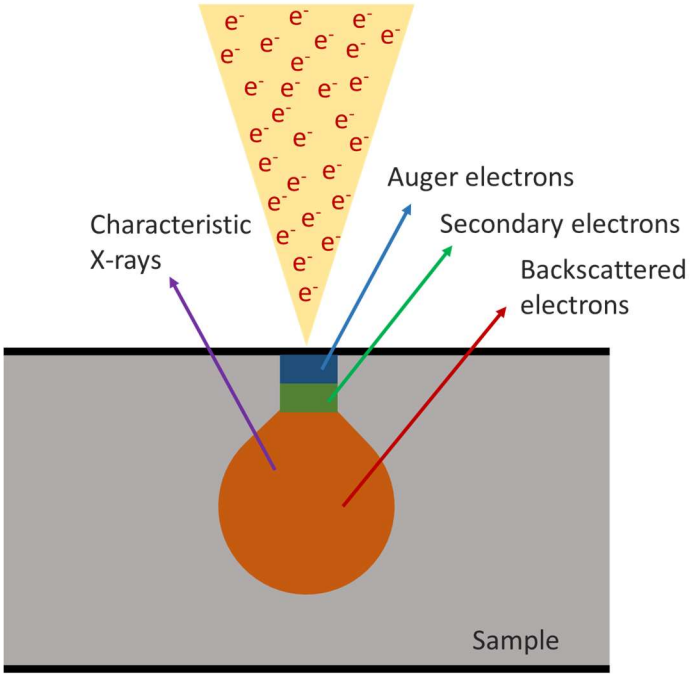

Figure 15. Interaction between sample and electron.

3.4.1. Energy dispersive X-ray Spectroscopy (SEM-EDS)

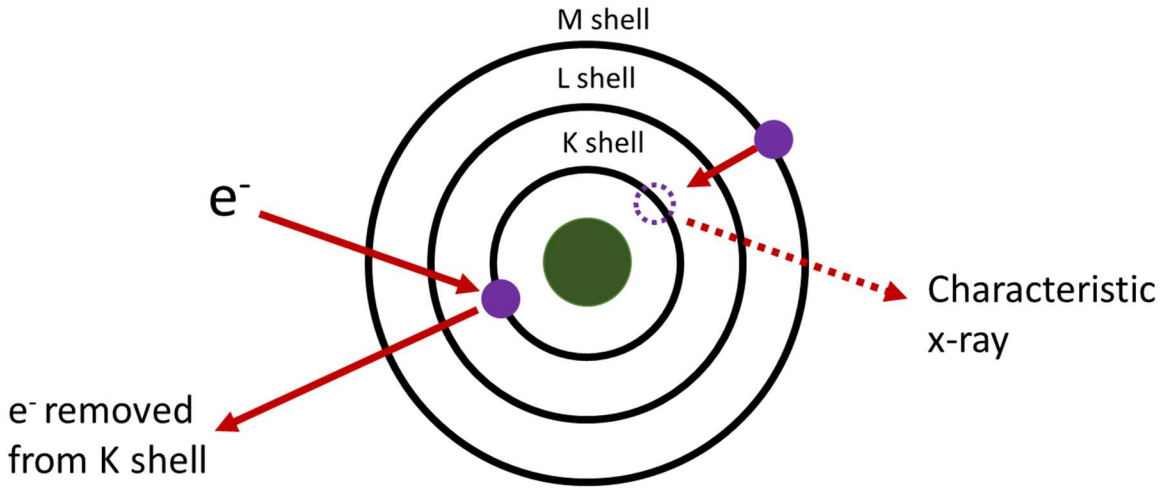

Figure 16. Schematic of x-ray generating from an electron source in SEM-EDS.

Energy dispersive x-ray spectroscopy is an extension of basic SEM imaging. EDS utilizes the X-ray emitted from a sample to analyze chemical composition of the specimen. When an incident electron hit the sample of interest, secondary electrons can be formed and removed from the shell. This results in a positively charged electron hole in an inner shell of an atom, in order to compensate for the electron loss an electron from the outer shell will relax into inner shell admitting a characteristic X-ray that is associated with electron-hole pair as demonstrated in Figure 16.

3.5. Transmission Electron Microscopy (TEM)

Transmission electron microscopy is often used to examine metals, alloys, ceramics, polymers, and biological specimens. TEM is a powerful technique to characterize the size, morphology, in size distribution of nanomaterials in high resolution. In comparison to SEM, TEM

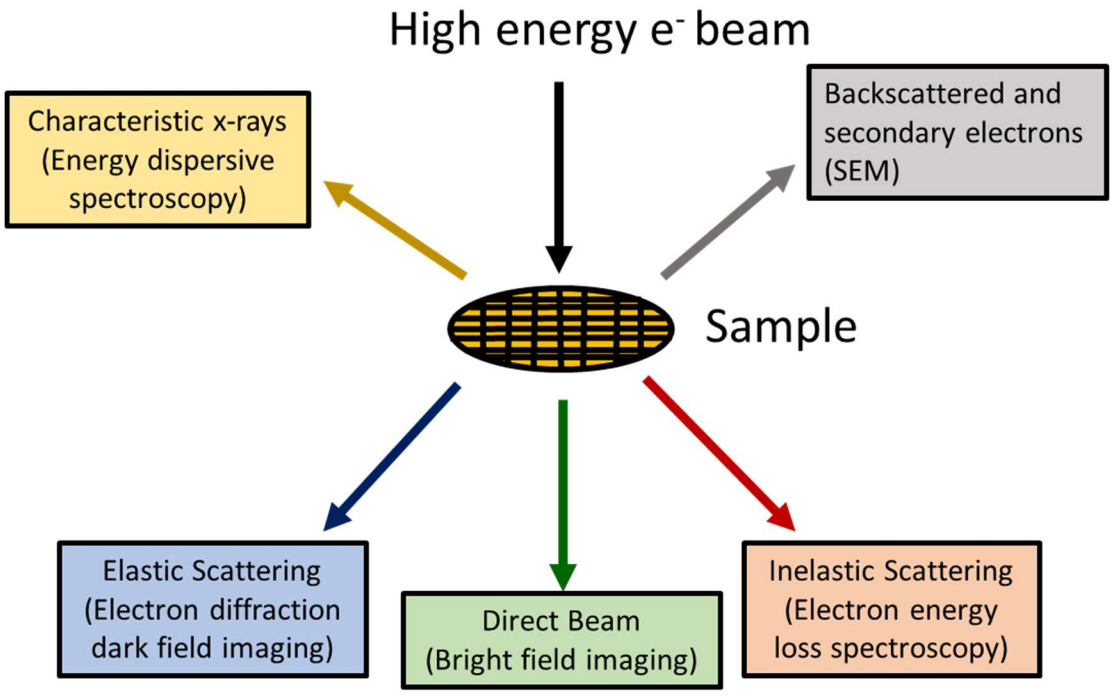

Figure 17. Examples of signal generated when a high energy electron beam interact with a sample.

use a high electron beam with energy ranges from 100,000 to 400,000 eV.[87] This high intensity electron beam allows for high resolution images where the electron beam is able to travel through specimen allowing for allowing a more detailed analysis. Images generated from TEM are limited to thin specimens (typically less than 100 nm), this is mainly due to fewer electrons being able to pass through a dense material resulting a very dark area on the image it generates. This is particularly important in the analysis of core shell, thin film gradient type materials.

When a high-intensity electron-beam interacts with a specimen, it emits characteristics x-rays, backscattered, secondary, elastic scattering, and elastic scattering of electrons. As mentioned in previous chapter, SEM-EDS utilize characteristic x-rays to identify the chemical composition of the specimen of interest. Electron diffraction information on a particular location of a specimen can be obtained from electron scattering phenomenon. This is more sensitive in comparison to x-ray diffraction since it allows the analysis of small sample size. Another type of TEM technique is called electron energy loss spectroscopy (EELS). This is observed as a result of the elastic scattering of electrons where the electron excite a core electron from the sample to the lowest unoccupied molecular orbital. This electronic excitation is characteristic to each element, and the identity of the element can be identified through this change in energy. EELS is an important method to determine if a specimen is indeed a core-shell material or an alloy of metals.

3.6. Fourier-Transform infrared spectroscopy (FT-IR)

Fourier transform infrared spectroscopy utilizes infrared light source to measure the absorption of an organic material. The schematic of a Michelson IR spectromenter is shown in Figure 18. When the sample is exposed to different infrared wavelength, some radiation is absorbed and others are transmitted. This result in a spectrum that shows a certain vibrational or rotational frequency that is associated with the energy that is absorbed in the sample. This is a

powerful tool that is used in the identification of functional groups in an organic material. Typical FT-IR can measure wavenumber between 500 cm^{-1} to 4000 cm^{-1}, however, 200 cm^{-1} to 800 cm^{-1} can also be observed using far-IR attachments. The use of far IR spectroscopy allow the measurement of vibrational or rotational frequency between metal Inorganic species.

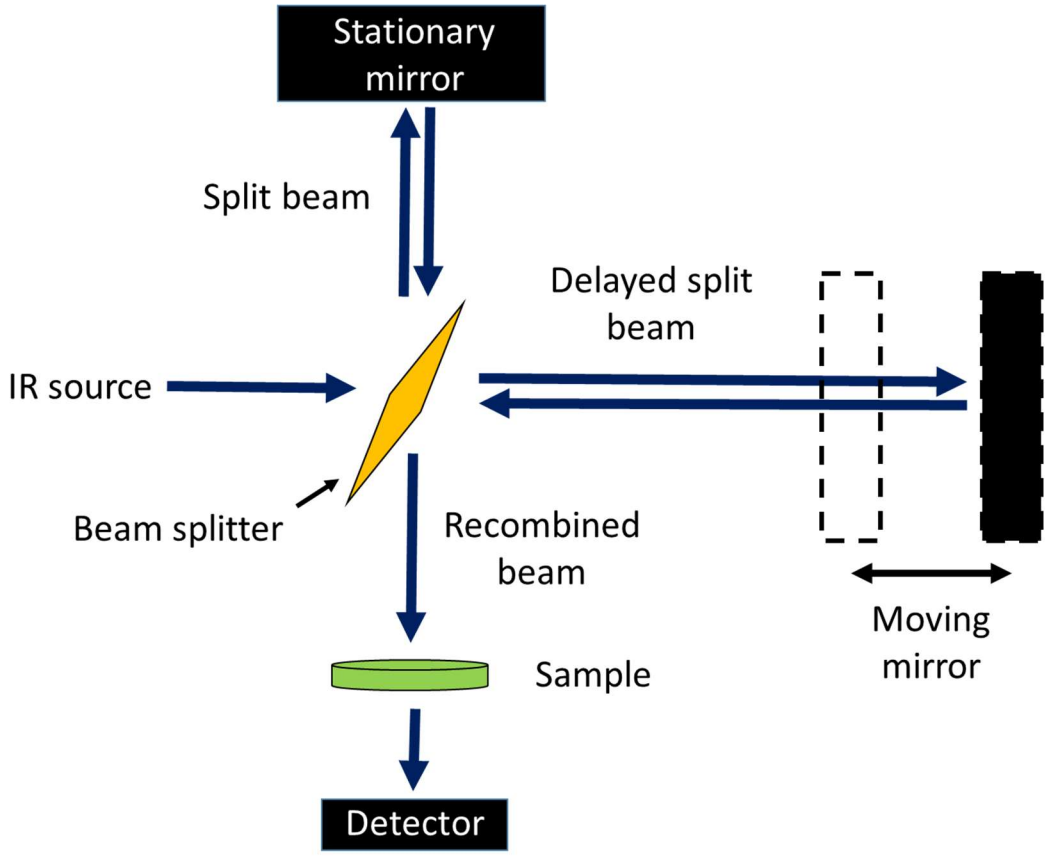

Figure 18. Schematic of a Michelson interferometer.

Chapter 4: Synthesis of Cobalt Carbide Nanomaterials using Seed Mediated Nucleating Agents

4.1.Introduction

Permanent magnet materials are extensively used in the present technologies where it can be found in the computer, medical, energy, and transportation industries.[88] High performance permanent magnetic materials are classified in three categories: rare earth 3d transitional metal alloys such as SmCo and NdBFe; AlNiCo magnets which is a family of iron alloys with Al, Ni, and Co; ceramic magnets which consist of strontium doped hexaferrites. The efficiency of permanent magnets are determined based on the maximum energy product $(BH)_{max}$ of the material. The maximum energy product of magnetic material is a measure of magnetic density within the material where it is the area of the largest rectangle under the B-H curve. Typically efficiency of the permanent magent materials increases with larger $(BH)_{max}$ area measurement. Among the different categories of permanent magnets, rare earth type magnets exhibit the highest energy product, however, it is often time expensive and prone to corrosion.[88] In comparison, AlNiCo and ceramic magnets have smaller $(BH)_{max}$ area in comparison to rare earth magnets, but they are more corrosion resistant and cheaper alternatives.

Since the 1980s, there have been serval advances in the development of rare earth free permanent magnetic materials. In recent years, carbon coating cobalt have been gaining attention as they are versatile in various applications such as permanent magnet, Fischer-Tropsch catalyst, magnetic recording, high resultion MRI, and magnetic toners.[4, 70, 89] The origin of the hard magnetic properties of cobalt carbide nanomaterials is due to the addition of C within the structure of Co quenches the local magnetic moment, resulting in uniaxial anisotropy in both the Co_2C and Co_3C phases.[89] Experimental data have shown that single phase Co_2C was found to be lower in coercivity (4.5-1200 Oe) and lower magnetization (20 emu/g), on the other hand, pure phase Co_3C was determined to exhibit higher coercivity (1.6-2.1 kOe) and higher magnetization (60 emu/g)

values.[70, 89] The highest energy product of Co_xC observed thus far typically consist of a mixture of 40-80% Co_2C. This is due to the uniaxial magnetic anisotropy of the Co_3C crystal structure causes a demagnetizing interaction between the nearby Co_3C gain, resulting in lower coercivity values.[89] By introducing Co_2C into the Co_3C structure, it minimize the demagnetizing interaction between the Co_3C crystals, creating an exchange coupling interaction and thus increasing its magnetic properties.[63, 70, 89]

Polyol synthesis of metal nanoparticles was first reported by Fievet et al. in 1993 for the synthesis of micron-sized copper particles.[59] In a typical polyol synthesis, metal salts are dissolved or suspended in a solution of a polyhydric alcohol where the solution is then heat up to the boiling temperature of the solvent for an extended period of time. The reduction of metal occurs upon the dissociation of the metal salt in the polyol medium at elevated temperatures, forming an intermediate to reduce the metal salt through a redox pathway, followed by the nucleation and growth of metal particles.[58] The first solution based cobalt carbide synthesis reported in 2004 using a one-pot polyol reduction process in the synthesis of cobalt carbide hard magnetic material in which a cobalt precursor is placed in a solution of polyol and the cobalt carbide nanomaterials is formed at high temperature.[70] Recent work have been focused on tailoring the size, morphology, and composition of cobalt carbide nanomaterials to optimize the magnetic properties of the material for various applications. Huba et al. have successfully controlled the Co_2C and Co_3C size and phase of cobalt carbide nanomaterials by adjusting the NaOH and NaCl concentration in a polyol solution.[63] It have been previously suggested that the formation of Co_xC in polyol solution is similar to Fischer-Tropsch catalysis process where a transitional metal catalyst is used to convert a mixture of carbon monoxide and hydrogen gas into hydrocarbons.[89] In this process, the transitional metal can often times transformed into metal carbide though a diffusion driven

mechanism from the decomposition of carbon monoxide in the system. Similarly, in the synthesis of cobalt carbides in polyol, the Co^{2+} is reduced to Co^0 at high temperatures and the glycol forms an ethoxy acetaldehyde.[89] The Co then remove a CO ligand from the acetaldehyde forming a cobalt-formyl intermediate, followed by the decomposition of carbon onto the surface of cobalt particles.[63, 90] It is well discussed in the literature that the reduction mechanism of polyhydric alcohol solution is dependent upon the formation of ethoxy acetaldehyde during the reduction of cobalt in solution.[89, 91-92] Here we present the study of heating rate, nucleating agent, and water to alter the reaction kinetics of Co_xC resulting in phase and morphology control of cobalt carbide nanomaterials.

4.2.Experimental

4.2.1. Synthesis of Cobalt Fumarate Precursor

Cobalt fumarate precursor was prepared by first dissolving 20 mmol of cobalt (II) nitrate hexahydrate (Alfa Aesar) in 20 mL of deionized water. In a separate container, 20 mmol of sodium fumarate dibasic (Alfa Aesar) was dissolved in 20 mL of deionized water. The solution consist of sodium fumarate was then magnetically stirred and heated to 50 °C to allow complete dissolution. The cobalt (II) nitrate solution was then added dropwise to the sodium fumarate solution. The mixture was allowed to stir for 15 minutes, during this time the cobalt fumarate forms a pink precipitate. The product solution was then allowed to cool to room temperature. It was then washed with a 50:50 ethanol-water mixture and centrifuged at 5000 rpm for 3 times to collect the final wet powder. Final product is obtained by drying in a vacuum oven at room temperature for 3 days.

4.2.2.Seed Mediated Synthesis of Cobalt Carbide Nanomaterials

Cobalt carbide nanomaterials was synthesized using a modified polyol process. In a typical experiment, 0.2 g of cobalt fumarate was dissolved in 20 mL of tetraethylene glycol (Alfa Aesar 99%). The solution was then purged with N_2 for 20 minutes prior heating. The solution was then mechanically stirred and heated to 300 °C at a rate of 15 °C/min. Once the solution reach 300 °C, 0.05 mmol of secondary metal salt ($RuCl_3$ / $Cu(OAc)_2$ / $Au(OAc)_3$) is added to the reaction. The solution remained at 300 °C for 30 minutes, and was allowed to cool to room temperature. The particles were magnetically separated and washed three times with ethanol.

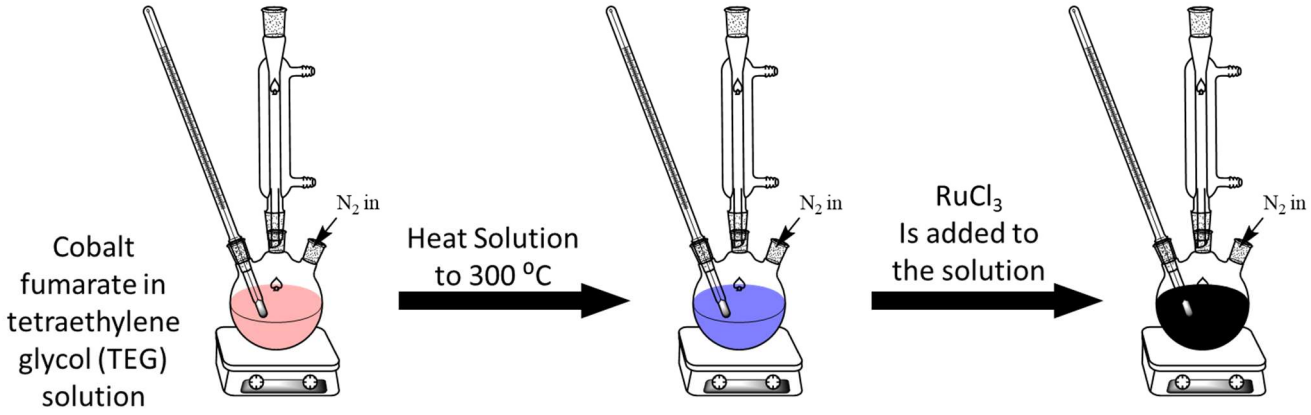

Figure 19. Reaction scheme for the seed mediated synthesis of cobalt carbide nanomaterials.

4.2.3. Characterization

PANalytical MPD X'Pert Pro x-ray diffractometer (Cu Kα = 1.54 Angstroms) was used for crystal phase identification. X'Pert HighScore Plus was used to analyze the x-ray diffraction (XRD) patterns and calculate the crystallite size of the particles. Scanning electron microscopy (SEM) was performed on Hitachi SU-70 FE-SEM operating at 5 keV. SEM samples were prepared on colloidal graphite paste and sputtered with platinum to prevent charging. Transmission electron microscopy (TEM) was performed using Zeiss Libra 120 operating at 120 keV. Samples for TEM

were deposited on 300 mesh Cu TEM grid. Magnetic characterization was performed on Quantum Design Versalab cryogen-free physical property measurement system. Field cooled (FC) and zero field cooled (ZFC) magnetization (M-T) curve was measured from 50-400 K in 100 Oe external field. The temperature and field dependence of magnetization was measured from 50-300 K with a temperature increment of 5 K.

4.3. Results and Discussion

4.3.1. Seed mediated Co_xC nanoparticles

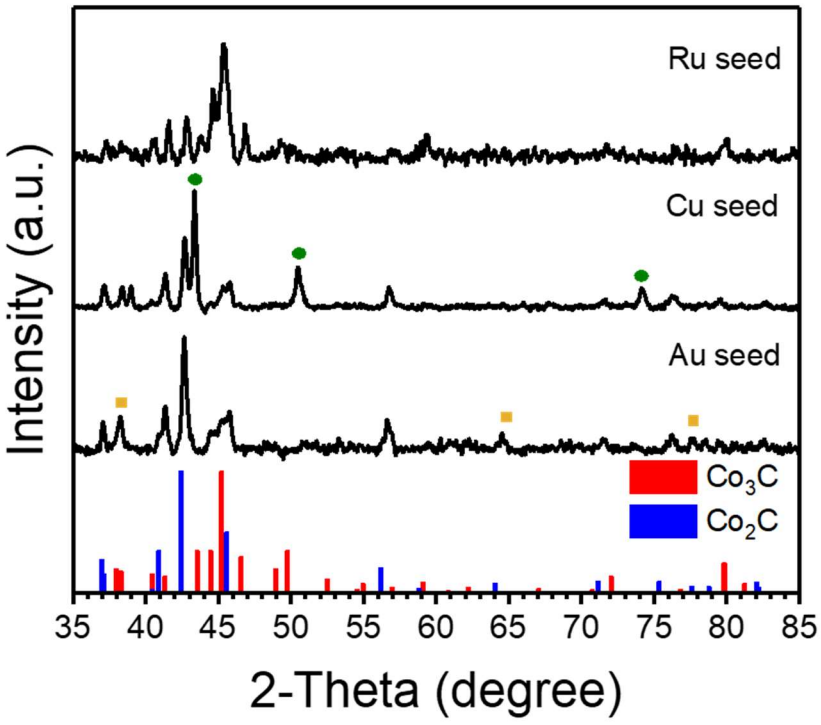

Figure 20. X-ray diffraction patterns of seed mediated Co_xC nanoparticles. Green circle represents Cu XRD peaks and yellow squares represent Au peaks.

Powdered x-ray diffraction was performed at room temperature to determine the phase presence in the as-synthesized nanocomposite. Figure 20 shows the diffraction patterns for Co_2C (reference: 03-065-1457), Co_3C (reference: 00-026-0450), Cu (reference: 03-065-9206), and Au

(reference: 00-001-1174) nanoparticles with synthesized using various nucleation agents. Rietveld refinement was performed to quantify the Co_2C (space group: *Pnnm* with $a = 4.4465$ Å, $b = 4.3707$ Å, and $c = 2.8969$ Å) and Co_3C (space group: *Pnma* with $a = 5.033$ Å, $b = 6.731$ Å, and $c = 4.483$ Å) phase presence is shown in Table 6. In all samples, XRD confirms that Co_2C and Co_3C phase a dominant phases in all these nanocomposites with mixed phase composition. In the Au and Cu seed mediated nanocomposite samples, they both show seed metal diffraction patterns on the XRD. However, in the Ru nucleating system Ru was not observed in the XRD pattern. In all XRD samples, all cobalt carbide nanocomposites do not show the presence of metal oxides.

Table 6. Rietveld refinement results for phase composition of Co_xC.

Metal Seed	Composition
Ru	73 % Co_3C 27 % Co_2C
Cu	30 % Co_3C 38 % Co_2C 32 % Cu
Au	66.7 % Co_3C 31.7 % Co_2C 1.6 % Au

In order to study the magnetic properties of the Co_xC nanocomposites, isothermal magnetization (M-H) curves at room temperature were collected for the as-synthesized Co_xC nanocomposites shown in Figure 21. The magnetization saturation values for Au nucleated Co_xC particles was 6.37 emu/g with a coercivity of 1430 Oe. With the addition of Cu to system, the magnetization saturation values were 10.9 emu/g with a coercivity of 1655 Oe. Surprisingly, the highest magnetization saturation of 33.5 emu/g with a coercivity of 2870 Oe was observed using Ru as the seed nucleating agent in this system. As previously confirmed with the XRD results for the absence of cobalt oxides, the positive ($+H_c$) and negative ($-H_c$) did not show a significant difference indicating the absence of exchange bias due to surface oxide particles. Theoretically,

the magnetocrystalline anisotropy energies are very similar.[70] Calculations have previously shown that pure phase Co_3C exhibit higher magnetization compared to Co_2C, however, experimentally Co_3C was found to be the phase that is higher in magnetization but lower in coercivity values than Co_2C.[93]

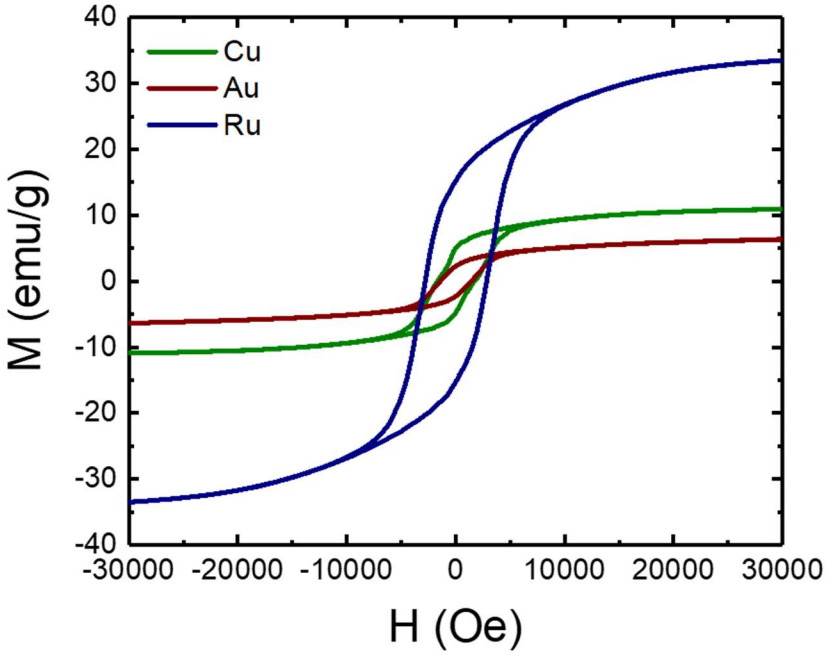

Figure 21. Room temperature isothermal magnetization (M-H) curve of CoxC nanocomposites.

SEM micrographs of Co_xC nanoparticles are shown in Figure 22. From the SEM observations, particle morphology using $RuCl_3$ as a nucleating agent result in particles with high aspect ratio needle like morphology that are approximately 50 nm in width and 1 μm in length. On the other hand, particles synthesized using $Cu(OAc)_2$ demonstrate popcorn like morphology approximately 150 nm in diameter. The particles synthesized using $Au(OAc)_3$ show plate like structures that are approximately 70 nm thick and 200 nm in diameter. Previous research have

shown that shape plays an important role in the magnetic properties of materials in the nanoscale where some particle morphology can introduce demagnetizing magneto-static interaction in the

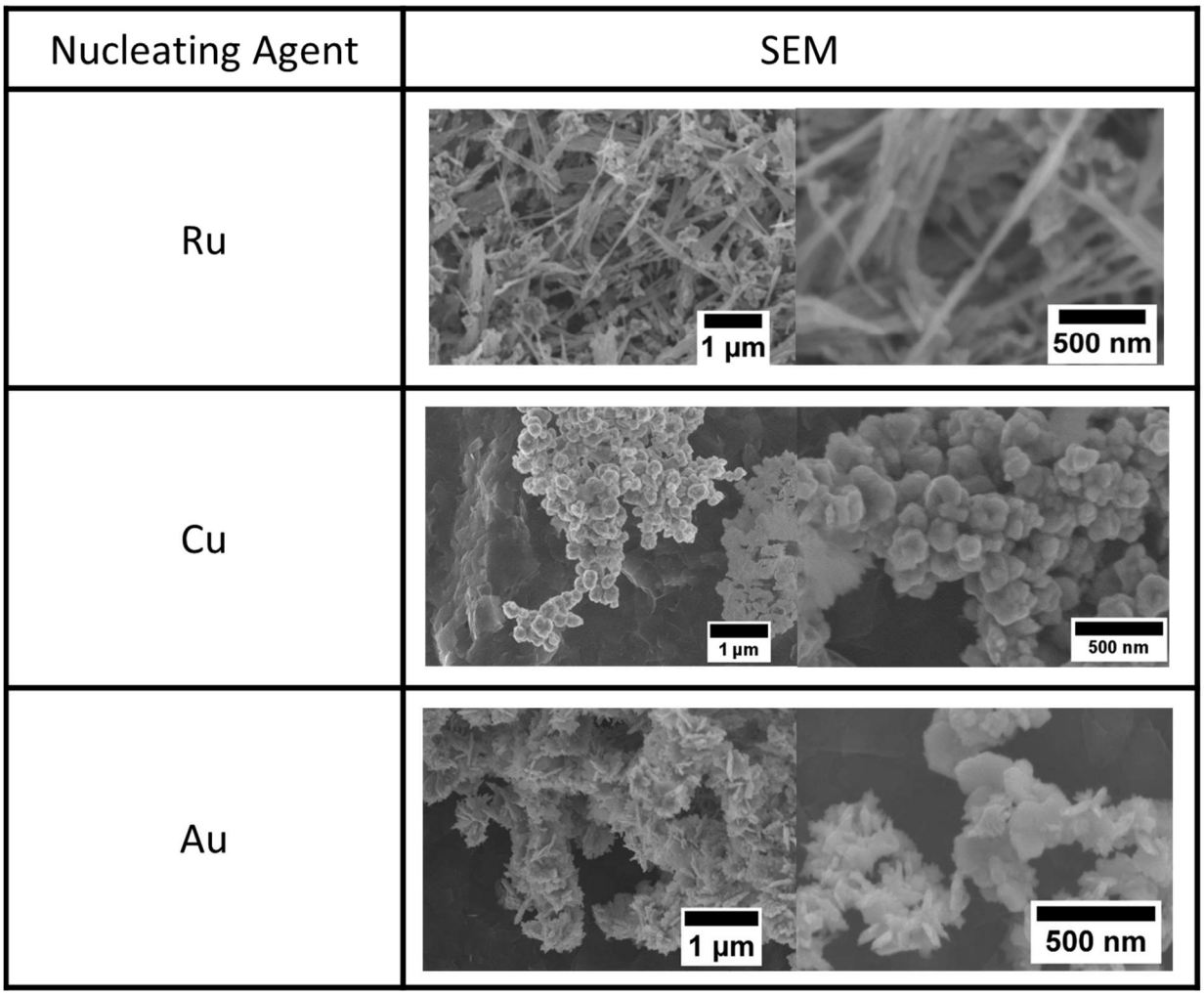

Figure 22. Scanning electron microscopy image of seed mediated Co_xC nanocomposite.

particles resulting in lowered coercivity.[5, 94-96] Experimentally, high aspect ratio nanoparticles with round edges possess higher shape anisotropy in comparison to spherical particles.[5, 94, 97-98] In our case of the needle like Co_xC nanostructures synthesized using Ru as the seed mediated nucleating agent, the shape anisotropy is introduced where the particles grow along a certain axis, thus minimalizing the internal demagnetizing field within the particle.

4.3.2. Ru seed mediated nucleating agent

The isothermal magnetization curve shown in Figure 23(a) was measured for the as synthesized Co_xC nanocomposite at difference temperature ranging from 50 – 400 K in 50 K increments. In Co_xC systems, typically a kink is observed at low temperature indicating a decoupling of hard and soft magnetic phases as a result of the temperature dependence magnetic properties such as magnetization, and exchange constant.[3, 70, 93] However, in our system the lack of kink in our M-H curve at low temperature infer that the hard and soft phases of Co_xC are coupled at low temperatures as well as room temperature. This is preferred in hard magnetic materials as it leads to higher energy product compared to decoupled systems. The maximum energy product (BH_{max}) observed for the needle like Co_xC nanocomposites was 1.92 MGOe with magnetization (M_s) of 33.5 emu/g and coercivity of 2870 Oe at room temperature. Stoner et al. have established that the coercivity dependence of temperature can be used to determine the blocking temperature (T_B).[99] In that regards, the measured coercivity as a function of the square root of temperature in

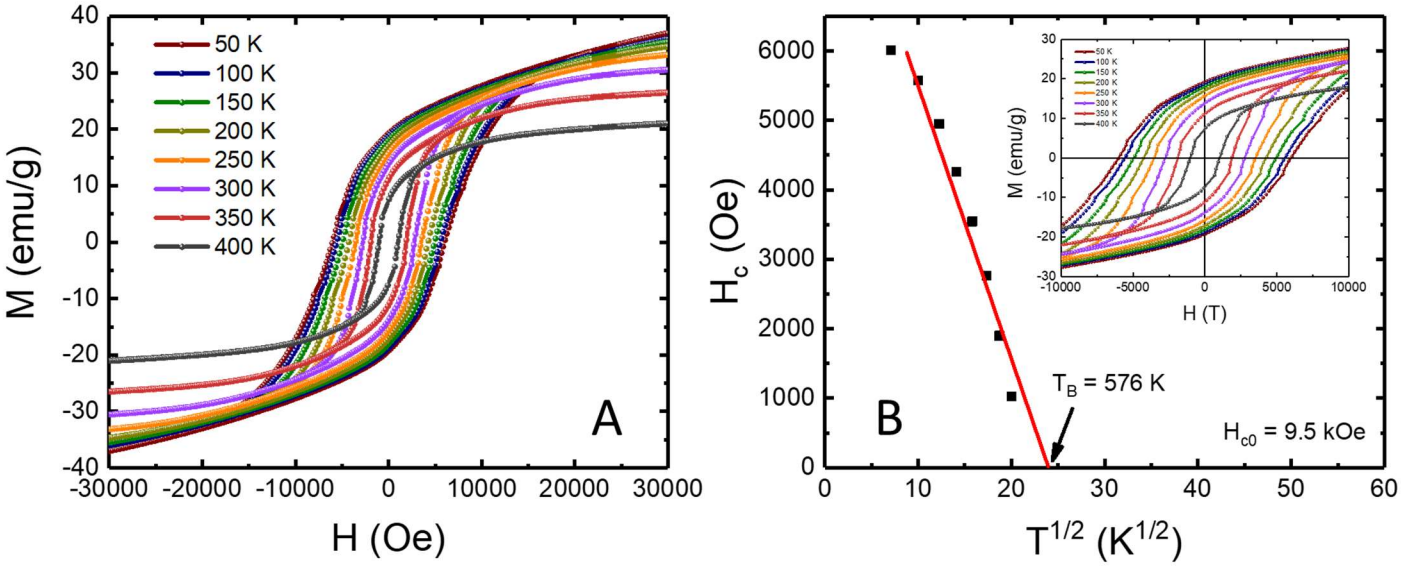

Figure 23. Magnetic properties of the as-synthesized Co_xC. (a) Magnetic hysteresis loop from 50 K - 400 K in 50 K increments. (b) Coercivity dependence on temperature in the determination of T_B and H_{C0}.

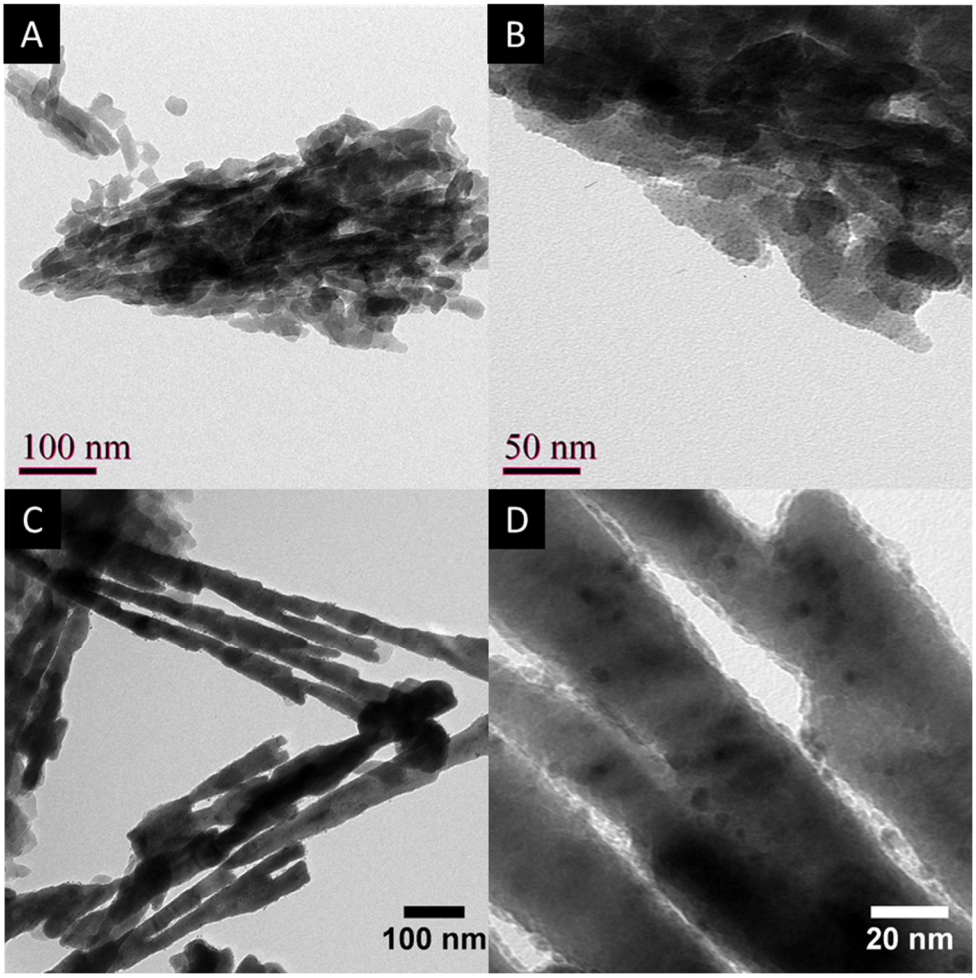

Figure 24. TEM image of CoxC synthesized (a-b) without nucleating agent (c-d) with Ru as nucleating agent.

Figure 23(b) was used to determine the T_B of the Co_xC as well as the coercivity at 0 K. The blocking temperature was determined to be 576 K and H_c at 0 K was determined to be 9.5 kOe. The observed T_B value is slightly higher than the Co_xC nanocomposites that are previously published in the literature.[3, 93] In order to determine the presence of paramagnetic character of the Co_xC, a Honda-Owen plot was constructed by plotting magnetic susceptibility verses inverse of magnetic field from 20 kOe to 30 kOe to quantify the amount of paramagnetic susceptibility. This revealed that the Co_xC nanocomposites synthesized with Ru seed mediated nucleating agent possessed 15.5% paramagnetic behavior. It is possible that Ru on the surface of the Co_xC

contributed to the paramagnetic character of the particles, however, paramagnetic character of the Co_xC nanocomposite up to 19.07% had been observed previously in the literature.[63]

TEM images of the as synthesized Co_xC are shown in Figure 24. Particles synthesized without nucleating agent shown in Figure 24(a,b) consist of short rods agglomerated to a larger structure. The Co_xC synthesized using 0.5 mmol $RuCl_3$ as nucleating agent showed an elongated needle like morphology shown in Figure 24(c,d). The needle like particles ranges from 20-50 nm in width and as long as 1 μm in length. TEM at higher magnification of particles synthesized using

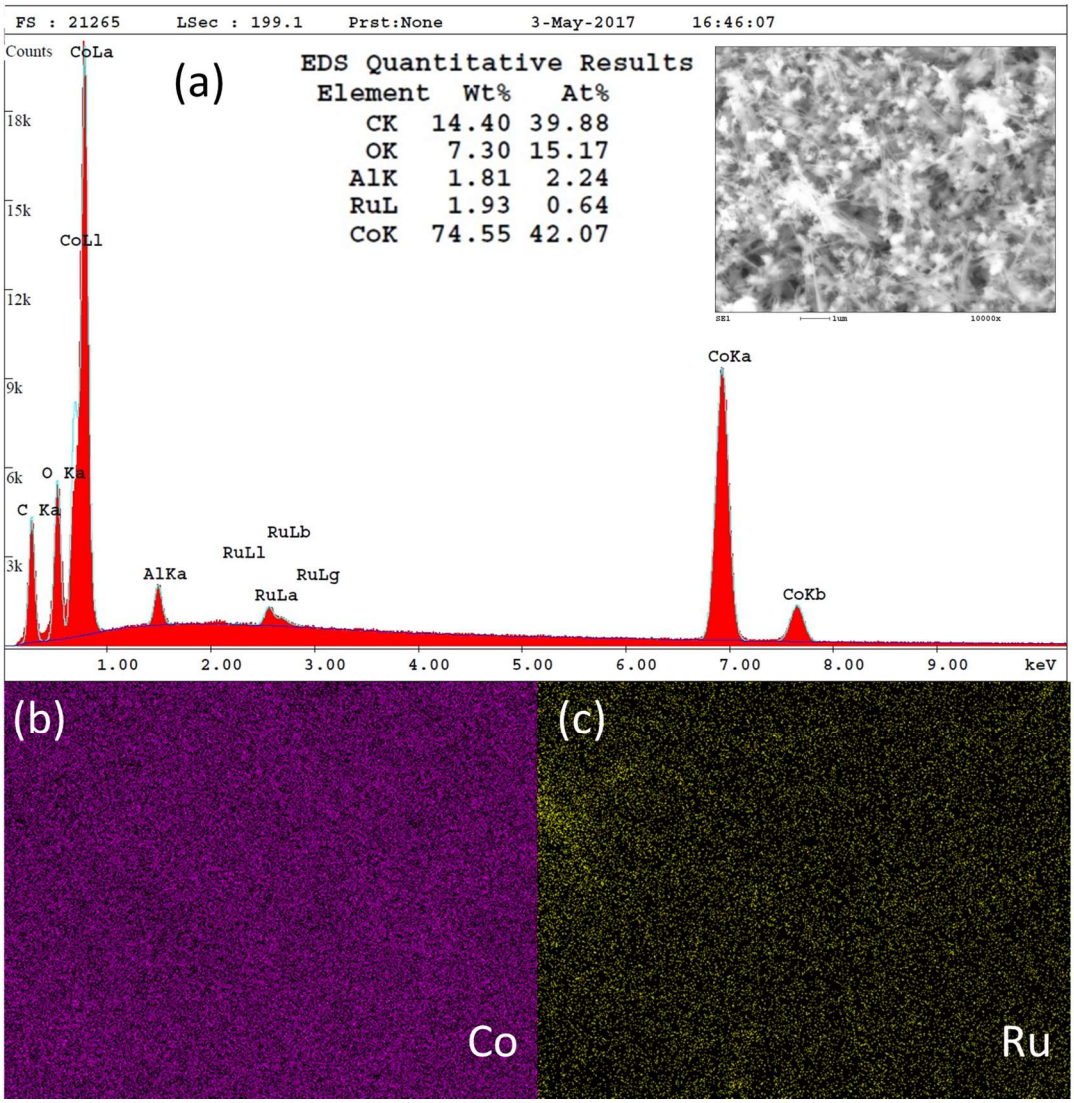

Figure 25. (a) SEM-EDX of spectrum of CoxC nanoparticles (b) selected area EDX mapping of Co (c) of Ru.

Ru seed nucleating agent (Figure 24d) show smaller particles on the surface of the seaweed like particles. This is potentially a result of small Ru particles nucleating on the surface of the larger needle like particles directing the growth of the Co_xC nanoparticles. SEM-EDX spectra in Figure 25(a) shown the presence of Ru in the area of interest with 42 at%, 0.64 at% of Co and Ru respectively. However, upon further examination with SEM-EDX elemental mapping shown in Figure 25(b, c) the Ru is shown throughout the sample. This result suggested that the Ru is evenly distributed on the surface of the Co_xC, however, it might be too small to accurately locate its distribution on the Co_xC. The exact mechanism involving the size and morphology control using a nucleating agent in the synthesis of Co_xC is not well studied. Typically, in a solvothermal synthesis the shape and morphology of nanoparticles is dependent upon the formation of metal clusters and the rate at which the metal atom formed and assemble are related to the reaction kinetics.[50, 100] The addition of Ru, Cu, or Au as seed mediated nucleating agent was to alter the reaction kinetics since the size and morphology of the product is highly sensitive to the reduction kinetics. It is possible that with the introduction of small amounts of Ru, Cu, or Au metal seed, the tetraethylene glycol to glyceraldehyde reduction pathway is catalyzed by the metal resulting in directional growth of the Co_xC nanoparticles.

4.3.3.Effect of heating rate and concentration of water in polyol system

It had been established that heating rate plays an important role in the synthesis of nanoparticles. Simulation studies in the literature showed that increasing rate result in smaller nanoparticles with a narrower size distribution compared to slower heating rate.[50] Typically, fast heating rate will result in higher concentration of particles at the end of the reaction and narrower particle size distribution. However, in the synthesis of Co_xC nanoparticles, it appears that the heating rate did not have a significant effect based on the X-ray diffraction patterns showing the

mixed phase Co_xC nanoparticles in Figure 26. However the differences in signal to noise ratio diffraction patterns Figure 26 suggests that the particles synthesized at the highest heating rate of 24.6 °C/min result in Co_xC that are comparatively less crystalline than particles synthesized from 8-18 °C/min. Ritveld and Scherrer analysis presented in Table 7 were performed based on the X-ray diffraction patter obtained in Figure 26. The Co_xC phase analysis did not show a distinct trend regarding the composition of Co_2C and Co_3C, suggesting that the synthesis of Co_xC is not sensitive to heating rate parameters and will fall between 45-55% Co_2C phase composition. However, Scherrer analysis shown in Table 7 suggest that heating rate impact the crystallite size of Co_3C and Co_2C where the crystallite size of Co_3C increases as the heating rate increases.

Table 7. Co3C and Co2C phase percentage at various heating rate.

Heating rate (°C/min)	% Co_2C	d_{XRD} Co_2C (nm)	% Co_3C	d_{XRD} Co_3C (nm)
8.7	46.7	44.9	53.3	16.3
12.4	50.9	39.3	49.1	17.5
18.1	58.9	50.2	41.1	20.0
24.6	52.2	31.4	47.8	27.8

The synthesis of metal or metal carbide nanoparticles by the reduction of metal precursor in polyol process typically begin with the dissolution of the metal precursor, reduction of the dissolved species, followed by nucleation and growth of the particles from the solution.[50, 58-59] Previously, Huba et al. were able to control the Co_2C and Co_3C phase of cobalt carbide nanomaterials by varying the concentration of [OH^-] and [Cl^-] in the polyol solution.[63] However, the H_2O content in the polyol solution was not well discussed since hydroxide salt is hydroscopic and can play a role in the properties of the glycol solvent as the metal salt dissociate in solution.

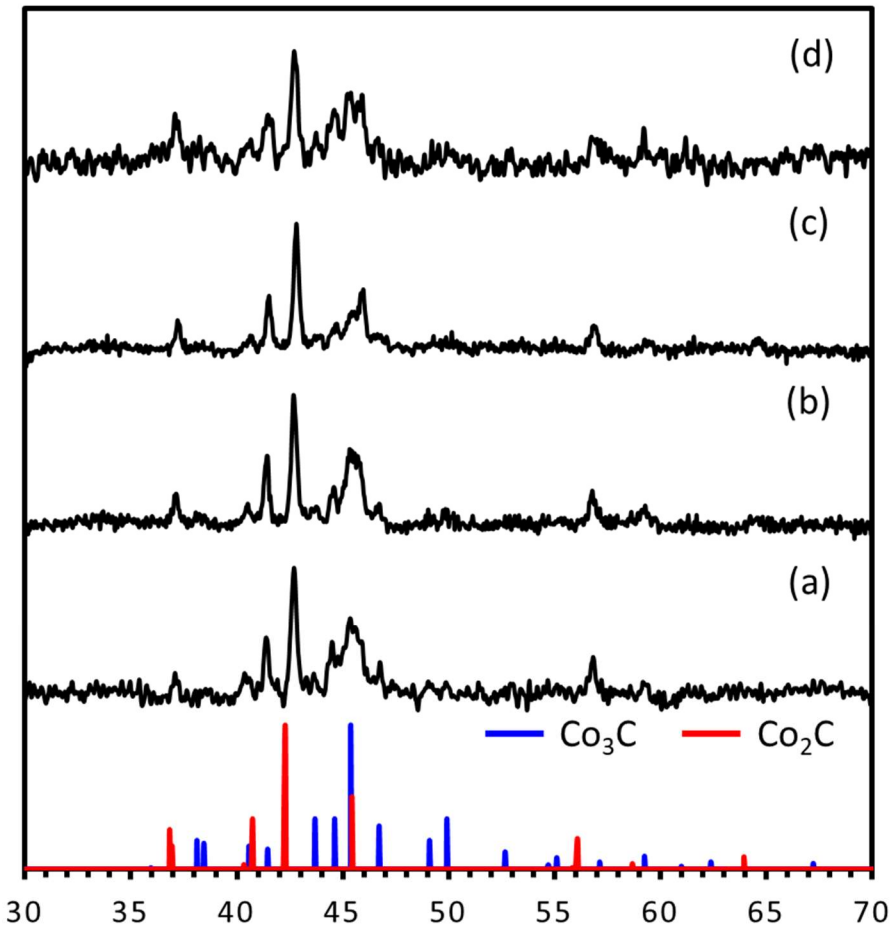

Figure 26. X-ray diffraction pattern of cobalt caride nanocomposite made at various heating rate (a) 8.7, (b) 12.4, (c) 18.1, and (d) 24.6 ºC/min. References for Co_2C (PDF 03-065-8206) and Co_3C (PDF 00-026-0450) are shown for comparison.

The water content within polyol solution is not well studied in Co_xC systems as the introduction of water could potentially encourage the formation of cobalt oxide species and alter phase composition. Figure 27 shows the x-ray diffraction analysis of the as synthesized cobalt carbide nanomaterials at various water content in the polyol solution. Rietveld analysis was performed to

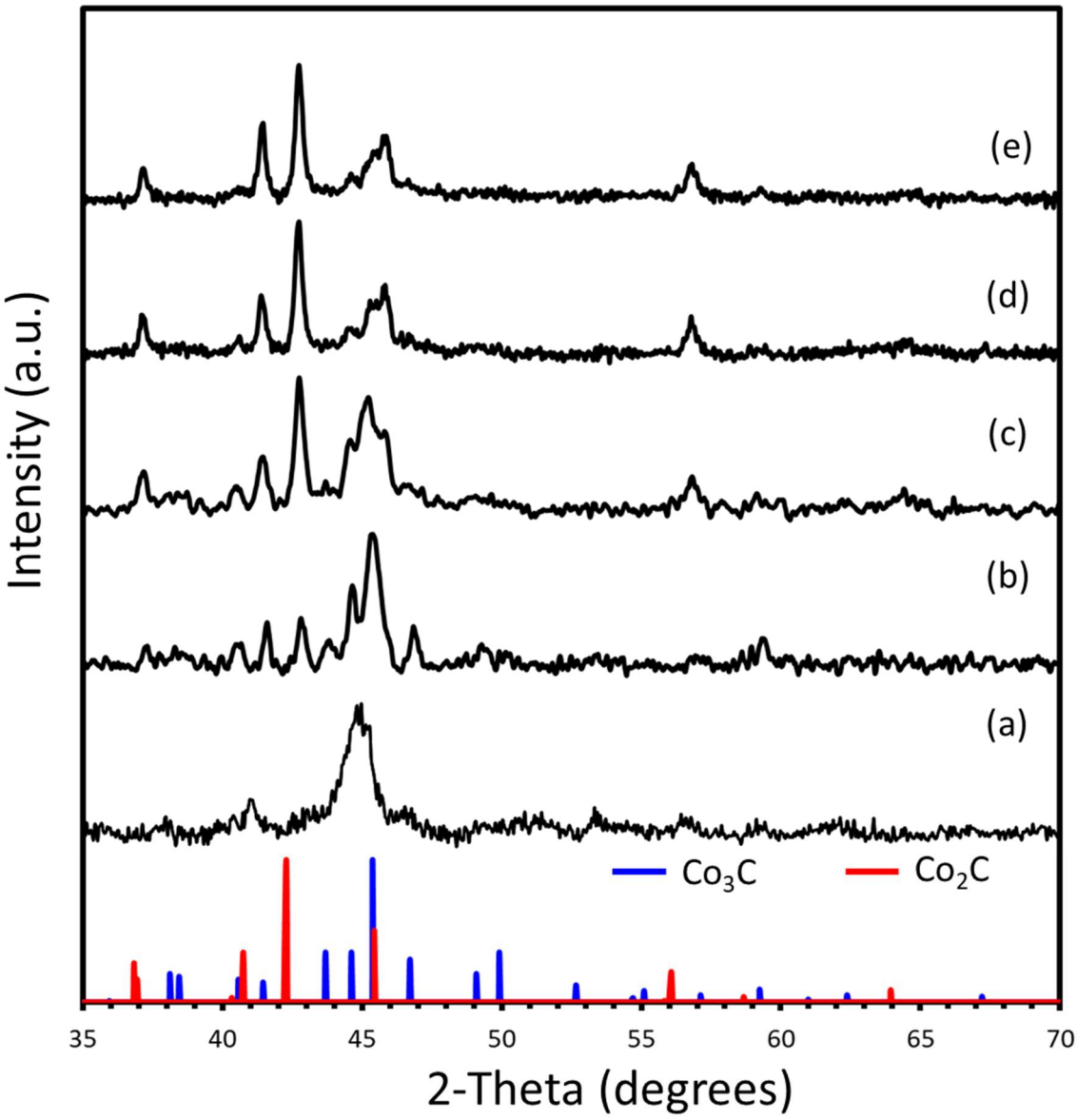

Figure 27. X-ray diffraction pattern of cobalt caride nanocomposite made with (a) 0, (b) 165, (c) 193, (d) 220, and (e) 442 mM of H_2O. References for Co_2C (PDF 03-065-8206) and Co_3C (PDF 00-026-0450) are shown for comparison.

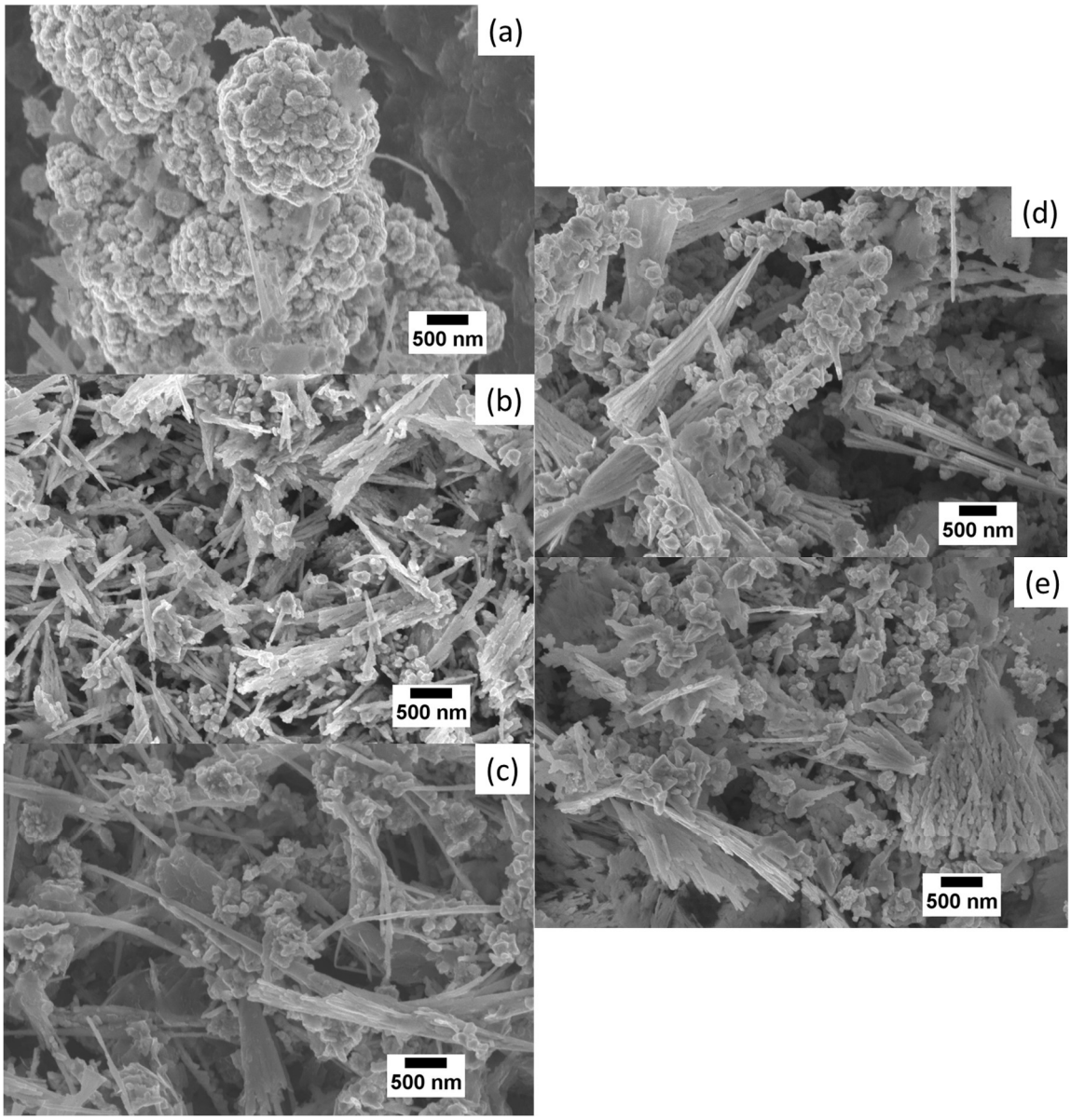

Figure 28. SEM images of cobalt caride nanocomposite made with (a) 0, (b) 165, (c) 193, (d) 220, and (e) 442 mM of H_2O.

determine the composition of the cobalt carbide phase. The x-ray diffraction patterns from Figure 27 appear to match both Co_2C and Co_3C phases, however their peak intensities of the diffraction pattern varies, suggesting that they are composed of a mixture of Co_2C and Co_3C as a result of water content in the polyol system. As shown in Table 8, the addition of H_2O affects the cobalt carbide crystal phase where in the absence of H_2O, only no Co_2C is observed in the as synthesized Co_xC. As the concentration of water within the system increases, the percent of Co_2C in Co_xC

increases. The most significant difference occur from 165.1 mM to 192.8 mM H_2O where the percent Co_2C increased from 13.8% to 42.7%. Magnetic measurements using the vibrating sample magnetometer shown in Figure 29 further confirmed the magnetic properties of the Co_xC nanomaterials. Where it was determined that Co_3C is the soft magnetic phase with magnetic moment up to 60 emu/g and 1.5 kOe coercivity and Co_2C is the hard magnetic phase with magnetic moment of 20 emu/g and up to 3 kOe coercivity.[89] The Co_xC particles synthesized with 165.1 mM H_2O exhibit the highest H_c and M_s in comparison to other Co_xC with various amount of H_2O in the system. As mentioned in the introduction, the formation of Co_xC the reduction mechanism of polyol solution is dependent upon the formation of ethoxy acetaldehyde species during the reduction of cobalt.[89] It is known that cobalt carbide formation is correlated to the oxidation of the glycol species in solution where pure cobalt carbide nanomaterial is formed at the higher oxidation rate of glycols.[89] Figure 28 shows the SEM micrographs of the Co_xC synthesized with various water content. As shown in the figure, in the 0 mM H_2O Co_xC produced small agglomerated particles with only a small presence of wires. However, as the H_2O concentration increased to 165 mM, needle type morphology started to appear. When the H_2O concentration is further increased to 193 – 220 mM, elongated wires were observed along with a higher concentration of spherical particles with rough features. Plate like structures and seaweed like morphology was observed with 440 mM H_2O in the system. The reduction potential of the polyol was found to be dependent upon its chain length, where longer chain typically lead to faster reduction rate.[101] The addition of H_2O into polyol solution likely altered the reduction kinetics of the tetraethylene glycol as the rate of ethoxy acetaldehyde formation is strongly relate to the reduction rate in the formation of nanoparticles in polyol solution.[92] From the XRD results presented in Figure 27 along with Rieveld analysis shown in Table 8, the absence of H_2O in the polyol process produced 97.5% Co_3C whereas

the high H_2O concentration produced only 39.6% Co_3C. This is consistent with previous findings in the literature regarding the rate at which single phase Co_2C is observed using a high concentration of hydroxide salts in the system.[63] In addition, the increase in water concentration in the system appears to have a mixed effect on the crystallite size and morphology of Co_2C and Co_3C, however, no trends have observe regarding the crystallite size of the two Co_xC phases. The increase in water content in the system resulting in higher Co_2C phase suggests that Co_xC synthesis is sensitive to moisture and thus alter the reduction kinetics of polyol as a solvent, reducing agent, and surfactant.

Table 8. Co_3C and Co_2C phase percentage at various H_2O concentration.

H_2O (mM)	% Co_2C	d_{XRD} Co_2C (nm)	% Co_3C	d_{XRD} Co_3C (nm)
0	0	---	100	8.8
165.1	13.8	48.5	86.2	14.9
192.8	42.7	34.1	57.3	10.4
220.5	55.8	47.4	44.2	20.0
442.6	60.4	46.9	39.6	16.2

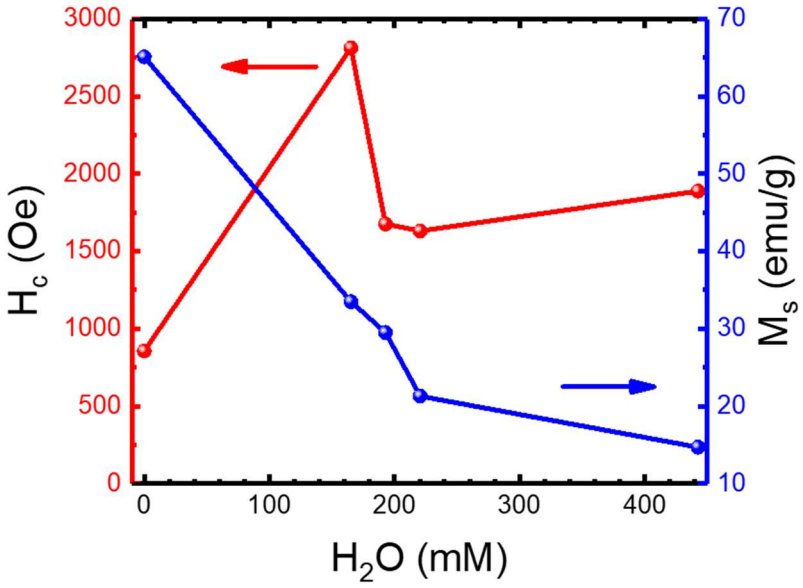

Figure 29. Magnetic properties vs. concentration of H_2O in solution.

4.4.Conclusion

In this chapter, nucleating agent, heating rate, and water content in the polyol synthesis of Co_xC (x = 2,3) nanomaterials were examined. To control the morphology of the particles, Au, Ru, and Cu were added as nucleating agents at evaluated temperature into a tetraethylene glycol solution containing cobalt precursor. The addition of Ru resulted in a needle-like Co_xC morphology with maximum energy product 1.92 MGOe (BH_{max}) observed, along with magnetization (M_s) of 33.5 emu/g and coercivity of 2870 Oe at room temperature. With the addition of Cu and Au nucleating agents, the morphology resulted in pop-corn and plate like structures, however, the magnetization significantly dropped in comparison Ru.

The second part of this chapter was to provide another approach in tailoring the magnetic properties of Co_xC nanomaterials through the change in reaction parameters: heating rate and

moisture content. Various amount of water was added into the solution of tetraethylene glycol and cobalt precursor. Interestingly, in the absence of water, 100% Co_3C phase was synthesized. With the introduction of H_2O into the tetraethylene glycol solution, the percent of Co_2C phase present in the Co_xC increase as well. This suggest that the moisture content of the glycol solution plays an important role in controlling the reduction rate of the Co^{2+} to Co^0, resulting in the difference in Co_xC compositions.

Chapter 5: Sol-Gel Synthesis of $LaCaMnO_3$ Perovskite Manganites

5.1.Introduction

Materials that exhibit magnetocaloric effect (MCE) as they have been gaining attention as they can be used magnetic refrigeration applications. The magnetic refrigeration (MR) technology that is based on the magnetocaloric effect provides an environmental friendly option to conventional gas compression technology that utilize chlorofluorocarbons and hydrocholofluorocarbons.[12] Magnetic refrigeration (MR) technology is based on the magnetocaloric effect (MCE) where the cooling efficiency is dependent upon the relative cooling power (RCP) of the material.[11-12] The MCE is a measure of thermal response to change in an external magnetic field.[11] It is based on the thermodynamic correlation of reversible change in magnetic entropy in an isothermal process defined using the Maxwell relations[19] shown in:

$$\Delta S_M\left(\Delta H\right) = \int_{H_1}^{H_2} \left(\frac{\partial M}{\partial T}\right)_H dH$$

where ΔS_M is the change in magnetic entropy, ΔH is the change in applied field, M is the magnetization, and T represent temperature. Near room temperature magnetocaloric materials with Curie temperature T_C near 300 K are of particular interest. Pecharsky et al. reported that GdSiGe based materials with entropy change of 36 J kg^{-1} K^{-1} at T_C = 272 K for a field change of 0-5T.[9] However, perovskite manganites with $La_{1-x}Ca_xMnO_3$ (LCMO) have been gaining interest due to its near room temperature large entropy change of 8.3 J kg^{-1} K^{-1} at 270 K for a field change of 0-5T.[35]

Lanthanum based perovskite manganites can be synthesized by ball milling, floating zone, pulsed laser deposition, and sol-gel methods.[102-105] Major advantages in obtaining nanomaterials via a sol-gel process include the ability to control the nucleation and growth steps resulting in large

scale production of monodispersed particles in comparison to other methods. The sol-gel method in the synthesis of perovskite manganites typically involve the dissolution of metal precursor along with citric acid and polyethylene glycol (PEG) in water.[81] The presence of citric acid and PEG allow the formation of metal chelate complexes within the solution catalyzing the polymerization of the gel.[81] In the perovskite manganites system, Wang et al. suggested that PEG polymer encapsulate the $La(NO_3)_3$ in controlling the nucleation and growth of particles by creating steric hindrance between the neighboring monomers.[106] In this work, we modified PEG chain length in the synthesis of the LCMO nanocomposites. Through this method, we report a significant enhancement in the magnetocaloric properties of the existing $La_{0.6}Ca_{0.4}MnO_3$ material by varying the chain length of the PEG polymer.

5.2.Experimental Section

5.2.1. Synthesis Method

The $La_{0.6}Ca_{0.4}MnO_3$ manganite nanomaterial was synthesized using a modified sol-gel technique. Typically, 6 mmol of lanthanum (III) nitrate (Alfa Aeasr 99%), 4 mmol of calcium carbonate (Aldrich), 10 mmol manganese (II) acetate hydrate (Acros Organics, 99%), 0.5 g of citric acid, and 0.5 g of polyethylene glycol (PEG) were added together and dissolve in 4 M solution of nitric acid. The solution was then heated to 70 ^{o}C for 6 hours to allow the polymerization of the gel as well as solvent evaporation. The initial solution consist of the metal precursors in nitric acid solution was a translucent clear color at room temperature. As the reaction process progress, the sol turns golden yellow once it reach 70 ^{o}C and lightens to pale yellow gel after 6 hrs. Upon the completion of gelation and solvent evaporation, the gel was then stabilized by annealing at 900 ^{o}C for 10 hours to obtain the final black powders.

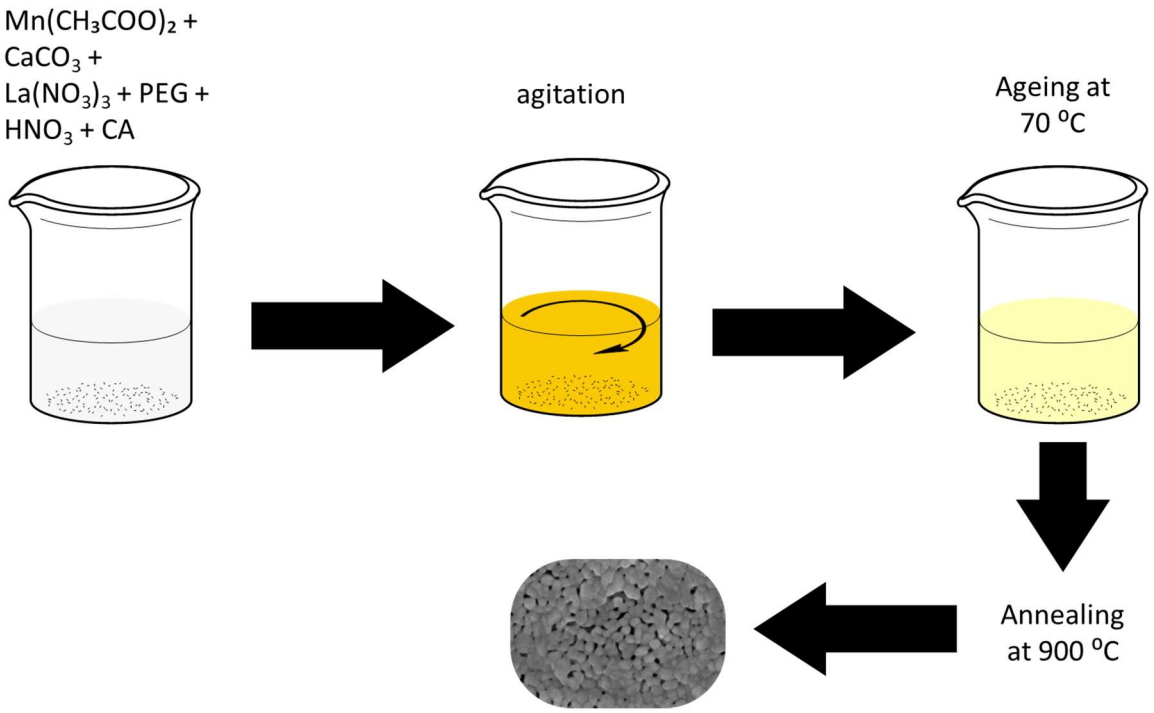

Figure 30. Synthesis method for reactions discussed in chapter 4.

5.2.2.Characterization

PANalytical MPD X'Pert Pro x-ray diffractometer (Cu Kα = 1.54 Angstroms) was used for crystal phase identification. X'Pert HighScore Plus was used to analyze the x-ray diffraction (XRD) patterns and calculate the crystallite size of the particles. Scanning electron microscopy (SEM) was performed on Hitachi SU-70 FE-SEM operating at 5 keV. SEM samples were prepared on colloidal graphite paste and sputtered with platinum to prevent charging. Transmission electron microscopy (TEM) was performed using Zeiss Libra 120 operating at 120 keV. Magnetic characterization was performed on Quantum Design Versalab cryogen-free physical property measurement system. Field cooled (FC) and zero field cooled (ZFC) magnetization (M-T) curve was measured from 50-400 K in 100 Oe external field. Banerjee criterion plots were constructed from the magnetization and applied field data to determine the order of magnetic transition. The temperature and field dependence of magnetization was measured from 50-300 K with a

temperature increment of 5 K. Far-IR spectroscopy was performed on Nicolet Advanced iS50 FT-IR with an ATR attachment.

5.3.Results

XRD analysis for $La_{0.6}Ca_{0.4}MnO_3$ nanomaterials synthesized using PEG 600, 2000, and 4000 revealed that all samples yield 100% of orthorhombic perovskite crystalline structure (reference PDF: 01-070-4067) represented in Figure 31. Crystallite size of each sample was calculated using Scherrer equation with the highest intensity peak at 32.9 degree 2-theta from the XRD patterns. The crystallite sizes were determined to be 62.8, 33.8, and 57.1 nm for the LCMO synthesized using PEG 600, 2000, and 4000 respectively. The morphology of all LCMO nanomaterials were examined using SEM and TEM analysis presented in Figure 32. As shown in

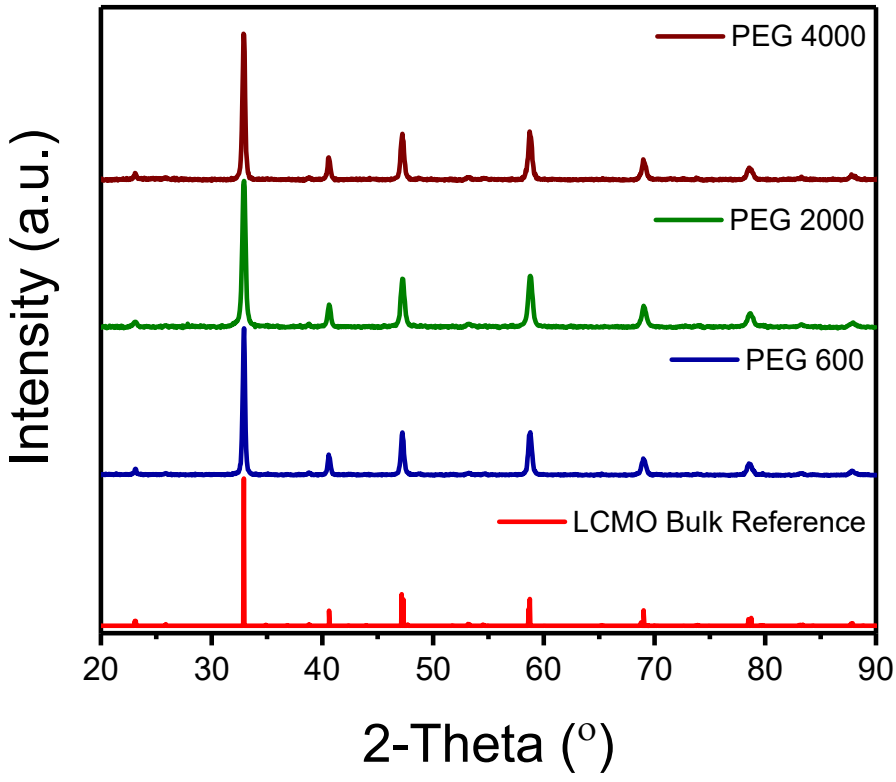

Figure 31. X-ray diffraction pattern of the as-synthesized LCMO nanomaterials.

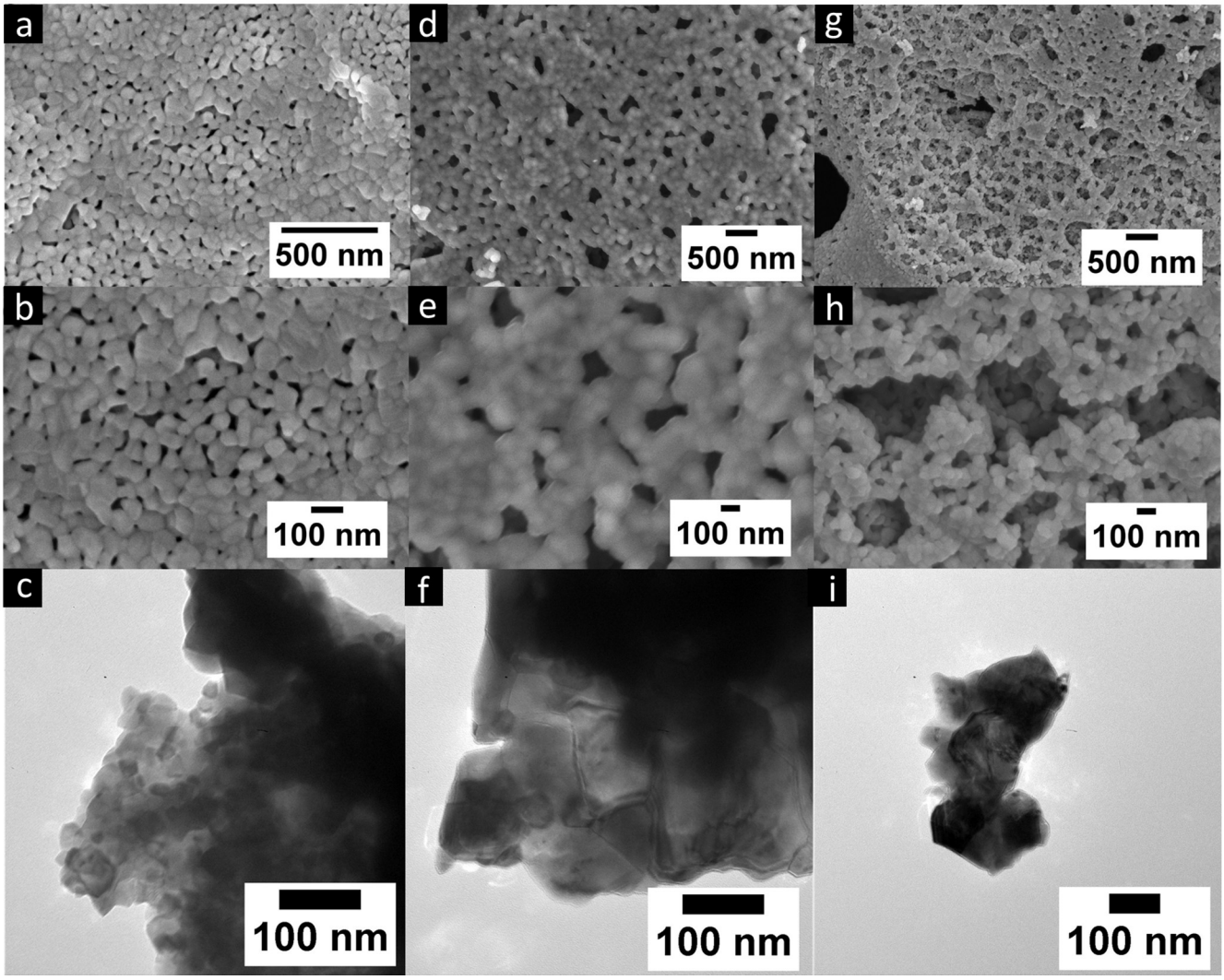

Figure 32. SEM and TEM micrographs of particles at different magnifications synthesized using (a,b,c) PEG 600 (d,e,f) PEG 2000, (g,h,i) PEG 4000.

the figure, particles obtained using PEG 600 (Figure 32 a,b) and 4000 (Figure 32 g,h)show distinct particles and appears to be less agglomerated compared to particles synthesized using PEG 2000 (Figure 32 d,e). TEM images show similar morphology for the three samples as well. Particles synthesized with PEG 600 consist of 42 ± 16 nm particles, whereas PEG 2000 and 4000 result in larger particles; 67 ± 35 nm and 71 ± 41 nm respectively. The observed particle size and the

calculated crystallite size from XRD pattern analysis are in disagreement, suggesting polydispersity and agglomeration in particle distribution within the sample.

The temperature and field dependence magnetization up to 3 T of the LCMO nanomaterials was measured using a commercial vibrating sample magnetometer (VSM). In order to study the magnetic properties of the LCMO materials, field dependence magnetization (M-H) curves at 5 K interval were obtained in order to calculate the change in magnetic entropy within the sample with respect to temperature. The M-H curve shown in Figure 33 were measured by first warming the VSM to 400 K to demagnetize the sample, then cooling the sample back down to 100 K and measure the M-H curve while the sample being warmed from 100 K – 300 K in 5 degree increments. Figure 35 shows the change in magnetic entropy ($-\Delta S_M$) for the LCMO samples calculated using eq 2 and data from Figure 33. As demonstrated in Figure 35, the overall maximum entropy of the LCMO nanomaterial increases as the external field increases. In addition, Figure 35 reveals that the LCMO sample synthesized using PEG 600 and 4000 result in the high $-\Delta S_M$ values of 19.3 $Jkg^{-1}K^{-1}$ and 17.7 $Jkg^{-1}K^{-1}$ at 3 T. Banerjee criterion plots were used to evaluate the order

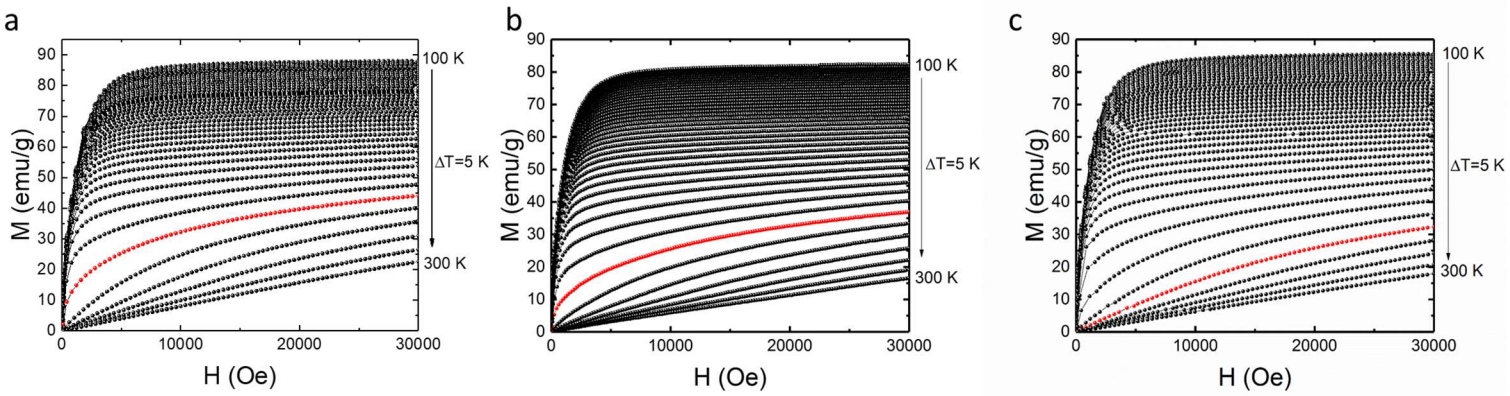

Figure 33. Isothermal magnetization (M-H) measured from 100 - 300 K (a) PEG 600, (b) PEG 2000, (c) PEG 4000.

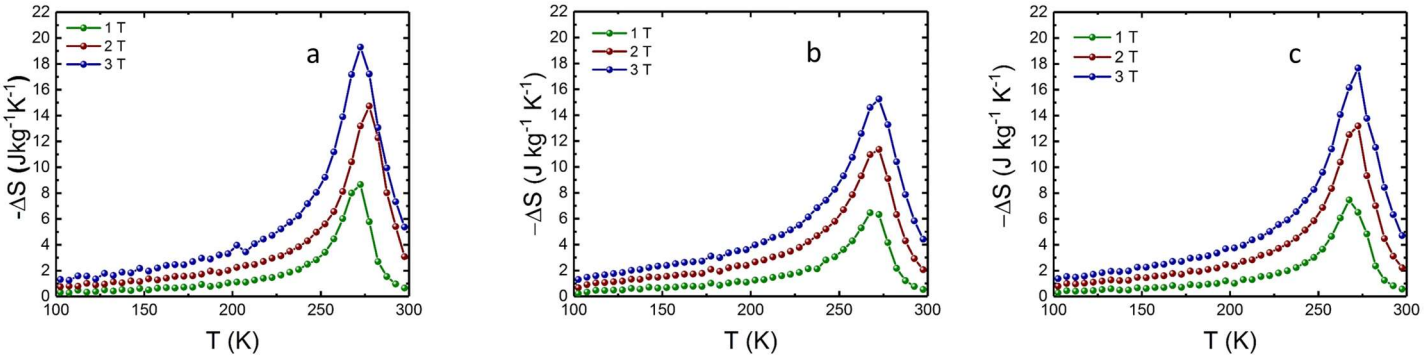

Figure 35.Temperature dependence of change in magnetic entropy of the as-synthesized $La_{0.6}Ca_{0.4}MnO_3$ calculated at various external field (a) PEG 600, (b) PEG 2000, (c) PEG 4000.

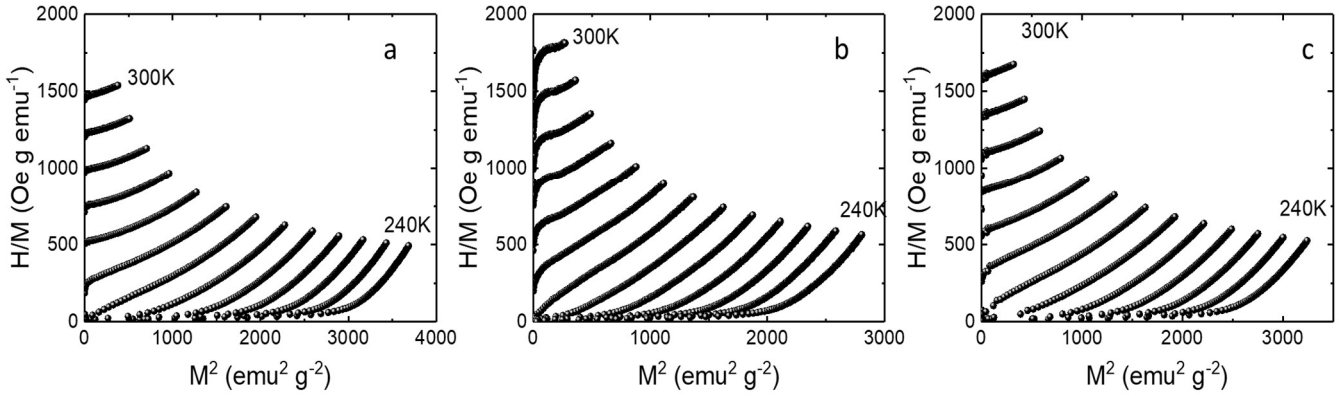

Figure 34. Banerjee plot of the LCMO sample synthesized using (a) PEG 600, (b) PEG 2000, (c) PEG 4000.

magnetic transition. This was achieved by plotting H/M vs M^2 near the transition region shown in Figure 34. From the Banerjee criterion all three samples exhibit second order magnetic transition with broad temperature range shown in Figure 35.

5.4.Discussion

In LCMO materials, the PM-FM transition is due to double exchange between the Mn^{3+} and Mn^{4+} that causes a spin coupling interaction resulting in Jahn-Teller distortion.[107] In addition, lattice distortions can be observed using Far-IR spectroscopy as phonon modes within the LCMO

system are infrared active.[108] Room temperature Far-IR spectroscopy results shown in Figure 37 indicates two major maxima at 549 cm^{-1} and 275 cm^{-1} for the LCMO synthesized using PEG 600, these peaks are associated with the stretching and bending modes of Mn-O-Mn bond.[108] However, in the Far-IR spectra for the PEG 2000 sample, the stretching mode shift to a lower wavenumber indicating that there is a bond angle and distance change between the samples. This suggests that the energy associated with the PEG 2000 sample is lower than that of the PEG 600 and 4000 samples resulting in the decrease in magnetic entropy. Since the crystallites synthesized using PEG 600 and PEG 2000 resulted in larger crystallite sizes (>60 nm) in comparison to PEG 4000. The Far-IR spectra could explain the cause of enhanced magnetic entropy in larger crystallite size materials in comparison to smaller crystallites, where the Mn-O-Mn bond energy is higher in comparison to smaller crystallites. In addition, particles synthesized using PEG 600 and 4000 appeared to be less agglomerated in comparison to particles synthesized using PEG 2000. Lampen et al. suggested that in nanoparticle systems the second order magnetic transition is strongly due to surface effects of the particles.[109] The particles synthesized using our method all show second

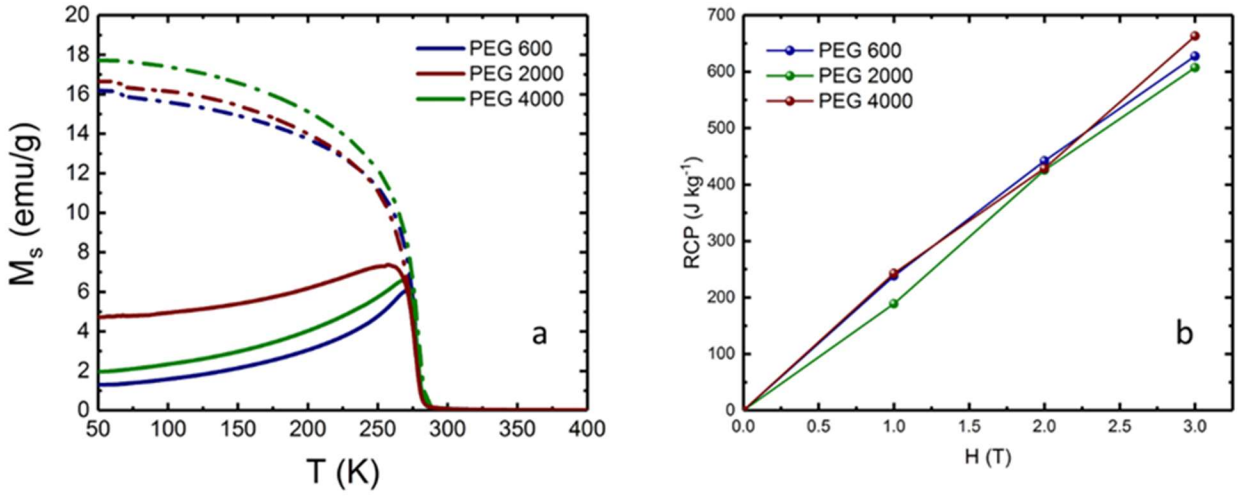

Figure 36. (a) M-T curves for the as-syntheized LCMO at 100 Oe applied field for ZFC (solid line) and (FC) dash, (b) calculated RCP values.

order magnetic transition behavior. In MCE materials, first order magnetic transition shows a narrow temperature range in comparison to second order magnetic transition, where the temperature range is typically broader.[22] Previous studies suggested that LCMO materials exhibit a change from first order magnetic transition to second order magnetic transition as the size of the particles decreases.[23, 109]

Relative cooling power (RCP) is used to measure the maximum entropy change in an ideal refrigeration cycle and is obtained by multiplying the maximum change in entropy $(-\Delta S_M)max$ by the change in temperature at full width half maximum (δT_{FWHM}) of the $-\Delta S_M$-T curve.[12] The RCP calculated for each sample is demonstrated in Figure 36b, showing that the RCP values are size dependent.

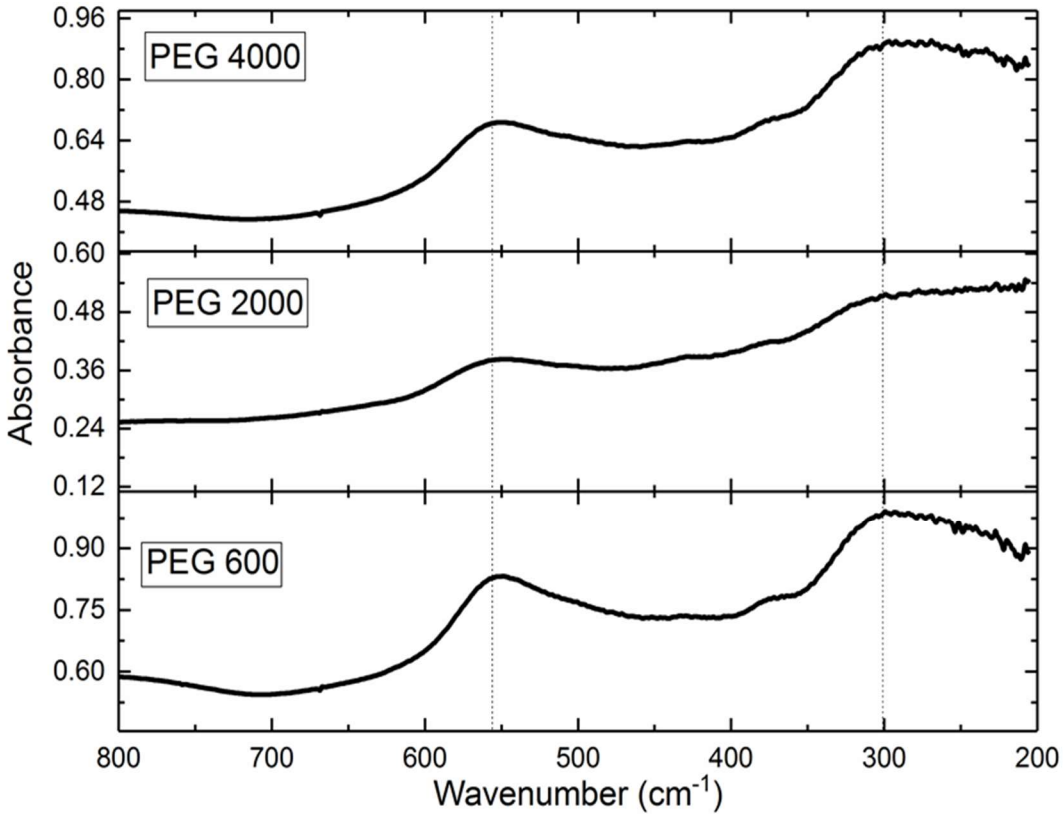

Figure 37. Far-IR spectroscopy of the LCMO samples.

The field dependence of ΔS for the LCMO manganite at a fixed temperature is accounted for in the N component of the power law $\Delta S_M(H) \propto H^N$. The N component is field independent at the maxima of magnetic entropy change and at the Curie temperature of the sample.[110] The temperature variation of in the N component for the LCMO are shown in Figure 38. Due to our instrument limitations, the magnetization isotherms were only measured up to 3T. Therefore the N component of the power law is an approximation between 0-3T. The minimum N values for PEG 600, 2000, and 4000 were found to be 0.66, 0.74 and 0.71 respectively. In all three samples,

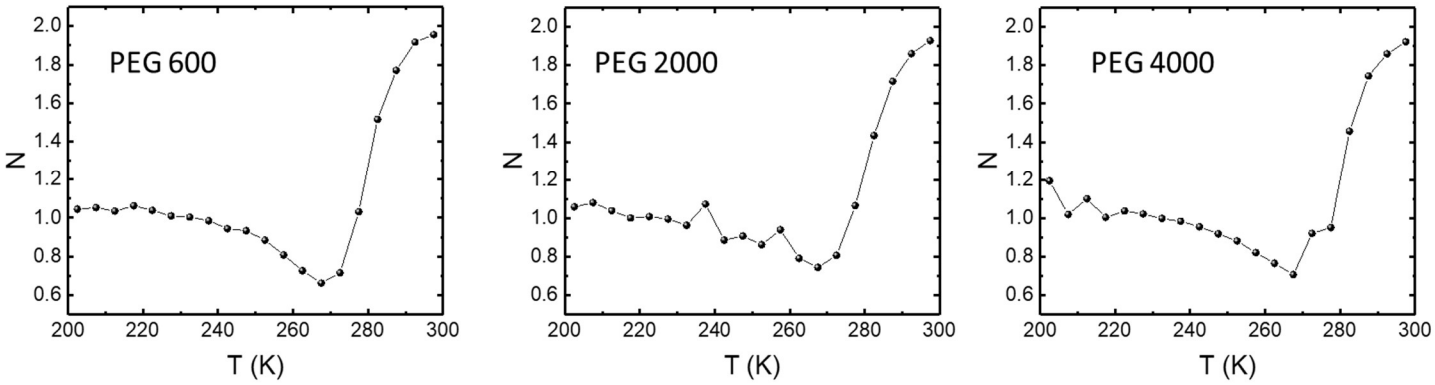

Figure 38. Temperature variation in the N exponent for the LCMO manganites.

the N values showed significant differences between the ferromagnetic and paramagnetic phase of the material. The shape of the N(T) behaves similarly to the polycrystalline samples in the literature.[110] The sample synthesized using PEG 600 have an N(T) value of 0.66, which was predicted at Curie temperature using the mean field approach.[111]

In comparison to the commonly used materials for magnetic refrigeration applications (Table 9), the $La_{0.6}Ca_{0.4}MnO_3$ in this work showed an enhancement in the magnetocaloric properties of current LCMO materials. Though the T_C of the LCMO nanocomposites are lower than that of Gd based material, the magnetic entropy is large enough to be used for magnetic

refrigeration applications as the cost of LCMO production is significantly lower than Gd based materials.

Table 9. Comparison of magnetocaloric effects in selected materials.

Sample	$\lvert(\Delta S_M)_{max}\rvert$ (J kg^{-1} K^{-1})	T_c (K)	RCP (J kg^{-1})	Reference
$La_{0.5}Ca_{0.5}MnO_3$	1.2 (2 T)	210	93	[34]
$La_{0.6}Ca_{0.4}MnO_3$	8.7 (1 T)	277	238	This work
$La_{0.6}Ca_{0.4}MnO_3$	19.3 (3 T)	277	627	This work
$La_{0.6}Ca_{0.4}MnO_3$	8.3 (5 T)	270	508	[35]
$La_{0.8}Ca_{0.2}MnO_3$	8.6 (4.5 T)	236	200	[36]
$LaMnO_3$	2.4 (5 T)	150	369	[37]
$La_{0.75}Sr_{0.25}MnO_3$	1.6 (1.5 T)	332	64	[38]
Gd	10.2 (5 T)	297	240	[112]
$Gd_{90}Fe_{5.7}Al_{4.3}$	7.2 (5 T)	279	744	[31]

5.5. Summary and Conclusions

In summary, near room temperature magnetocaloric properties were obtained for $La_{0.6}Ca_{0.4}MnO_3$ via a modified sol-gel method. In this study, PEG was shown to control morphology and magnetocaloric properties of the LCMO nanomaterials. The structure and morphology were investigated using XRD, TEM and SEM. Magnetic measurements revealed that the nanoparticles undergo a second order magnetic transition with the PM-FM transition near room temperature. The maximum change in magnetic entropy ($-\Delta S_M$) was found to be 19.3 Jkg^{-1}K^{-1} at 278 K for a field change of 0-3 T and 8.7 Jkg^{-1}K^{-1} for a field change of 0-1 T. The relative cooling power (RCP) that is used to evaluate magnetic refrigeration properties was determined to be 627

Jkg^{-1}. This synthesis method has demonstrated an enhanced magnetocaloric effect comparing to the current LCMO literature. In addition, these material are also comparable to that of Gd based magnetocaloric materials, suggesting that this can be a promising material for magnetic refrigeration application.

Chapter 6: Summary

The primary focus in the work of this dissertation is to expand our understanding in synthetic routes in the synthesis of cobalt carbide and lanthanum calcium magnesium oxides to enhance magnetic properties of existing materials. As stated in previous chapters, this dissertation was mainly separated into two parts: cobalt carbide as hard magnetic materials and lathan calcium based manganite for magnetic refrigeration. The primary goal of the development of cobalt carbide and materials in this work is to provide rare earth free alternative to currently available hard magnet material. In cobalt carbide section of this work, a modified polyol synthesis approach using hot addition of nucleating agent was shown to be able to modify the size, and morphology of the as-synthesized particles leading to an enhanced magnetic anisotropy. In addition, heating rate and water content in a polyol synthesis were also investigated. It was found that there was no noticeable trend regarding the phase of cobalt carbide under different heating rate. However, the final phase of the cobalt carbide nanomaterial obtain was found to be dependent upon the water content in the system. With this approach, we have obtained cobalt carbide nanomaterial with the maximum energy product up to 1.92 MOe (BH_{max}), along with magnetization of 33.5 emu/g and a coercivity value of 2870 Oe at room temperature.

The second part of this work involve the synthesis of perovskite type manganite lanthanum calcium magnesium oxide. We were able to manipulate the as-synthesized morphology of the LCMO material, resulting in a higher observed magnetic entropy. It was found that with the use of different chain length of polyethylene glycol, the magnetic entropy observed vary dramatically. In addition, we have determined that using PEG 600 result in LCMO second order magnetic transition behavior with a broad temperature range. We were able to deduce that the origin of the increase in magnetic anisotropy is a result of the bond energy of Mn-O-Mn bond. By visual observations from the SEM micrographs, the magnetic entropy appears to be observed in particles

that are of larger crystallites sizes. Relative cooling power and magnetic entropy of the material was found to exceed Gd in the literature, however, much work will be require to optimize the system to directly compare with GdFeAl systems. Nevertheless, LCMO synthesized using our sol-gel method reported in Chapter 5 is promising for magnetic refrigeration as it have shown comparable properties with only a third of the cost.

Appendix I: Friction and Wear Properties of Copper, Cerium oxide, and Iron oxide Nanoparticles

A.1.1. Introduction

Lubricants are often used to reduce friction, prevent where, transport debris, and provide cool line between interfaces in motion.[113] The study of tribology involve the study of two or more interacting surfaces. Tribology is in a wide field that is applied in transportation, renewable, and environmental industries. In the transportation sector, lubricant formulation consists of a base oil with mixtures of hydrocarbons such as olefin and paraffin with a surface modifying additive system. The base oil provides cooling to interacting parts and serves as a transport agent in the delivery of additives. Engine systems are typically under high pressure and high temperature conditions, overtime the base oil will start to oxidize and degrade resulting in undesirable by products that can potentially lead to engine failure.[114-116]

In recent years the use of metallic nanoparticles as lubrication additives have been gaining attention as governmental policy have been pushing for high energy efficient vehicles due to environmental concerns.[117] Metallic nanoparticles have shown advantage over traditional additives as their size, morphology, and surface can be easily modified in solution synthesis. In addition, it have shown that nanoparticles have the capability to reduce friction between contacting surfaces to improve the loading capacity and longevity of parts.[113, 118-119] Previous work in the literature have showed the nanoparticles can be used to reduce friction and wear of the surface, however the exact friction reducing mechanism with regards to the composition and size of the nanoparticle remain a topic of debate among the lubrication industry. Multiple theories have been developed to explain the mechanism and they include ball bearing effect, mending effect, rolling effect, colloidal effect, protective film formation, and third body material transfer.[120] As the name suggests, ball bearings effect suggest that the lubricant additive is acting as ball bearings between rubbing surfaces and the slide and roll motion loading will constantly reduce friction between two

parts. The mending effect indicate that as the temperature of the system increase, the frictional force will cause the material to be compressed on the surface causing repairing effect on the interacting surfaces.

Boundary lubrication regime occurs during high load and low moving velocity situations. In this regime, the oil layer film created by the base oil on the interacting surfaces are not strong enough to protect the surface from wear. During the stage, the surface is under high friction and the base oil is only acting as a carrier for additives.[117] Copper, cerium oxide, and iron oxide have shown interesting tribological properties in boundary lubrication regime. However, direct comparison in the size and morphology between materials is lacking in the literature. This work will focus on the use of nanoparticles in boundary lubrication regime.

A.1.2. Experimental Section

A.1.2.1. Synthesis of cerium oleate precursor

The synthesis of cerium oleate precursor was modified from reference 54. Cerium oleate precursor prepared by first dissolving 20 mmol of sodium oleate (VWR) along with cerium chloride heptahydrate (Alfa Aesar) in a mixture of 40 mL 190 proof ethanol, 30 mL DI water, and 70 mL of hexanes. The solution was then heated to 70 °C for 4 hours and allowed to cool to room temperature. The cerium oleate complex is in the upper hexane layer of the solution. Final product was obtain by washing with water three times and the waxy product was obtain by evaporating the solvent using a rotovap.

A.1.2.2. Solvothermal synthesis of copper and ceria nanoparticles

In a typical synthesis, hydrated salt such as cerium oleate, or copper (II) acetate hydrate was added into a solution consist of oleylamine, oleic acid (or HDEHP for Cu NPs), and 1-

octadecene. The solution was heated to 80 °C for 30 mins in order to fully dissolve the precursor salt. The resulting solution was then heated to 260 °C for 2hrs (20 mins for Cu NPs). The product solution was then washed with a mixture of 50:50 acetone and ethanol mixture and separated by centrifugation at 9000 rpm for 10 min.

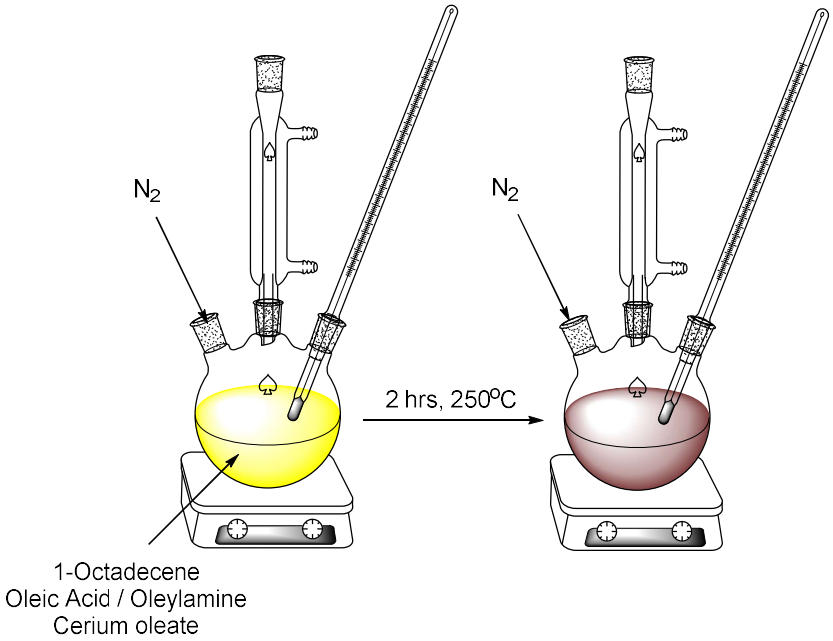

Figure 39. Reaction scheme for the synthesis of Cu and CeO_2 nanoparticles.

A.1.2.3. Co-precipitation synthesis

A.1.2.3.1 Iron oxide nanoparticles

In a typical synthesis, 5 mmol iron (II) chloride tetrahydrate and 10 mmol of iron (III) chloride hexahydrate were dissolved into 10 mL of deionized water. In a separate flask, 3 mL of concentrated ammonia hydroxide was then diluted to a final volume of 50 mL. Both of the solutions were then degassed with N_2 for 30 minutes. Stirring continuously, the iron solution was then added dropwise to the ammonium hydroxide solution along with 2 mL of oleylamine and oleic acid. The product solution turned black immediately upon the addition of the iron solution

and was allowed to stir for another 10 minutes. The product was then collected with centrifugation at 9000 rpm.

A.1.3. Characterization

PANalytical MPD X'Pert Pro x-ray diffractometer (Cu Kα = 1.54 Angstroms) was used for crystal phase identification. X'Pert HighScore Plus was used to analyze the x-ray diffraction (XRD) patterns and calculate the crystallite size of the particles. Scanning electron microscopy (SEM) was performed on Hitachi SU-70 FE-SEM operating at 5 keV. SEM samples were prepared on colloidal graphite paste and sputtered with platinum to prevent charging. Transmission electron microscopy (TEM) was performed using Zeiss Libra 120 operating at 120 keV. Samples for TEM were deposited on 300 mesh Cu TEM grid. X-ray photoelectron spectroscopy was performed on ThermoFisher ESCAlab 250 with a focused monochromic Al Kα x-ray (1486.6 eV) source. Tribological properties was tested on a PCS instruments high frequency reciprocating rig (HFRR) at 70 ºC, 100 º, and 130 ºC oscillation with 4N load, 1 mm diameter, on steel for 25 min. Tribofilm formation was measured and observed using PCS instruments mini-traction machine with spacer later imaging method with 50% slide-roll with 31 N (1.0 GPa).

A.1.4. Results and Discussion

A.1.4.1 Copper / copper oxide nanoparticles

TEM was used to determine the size of morphology of the as synthesized Cu nanoparticles. As seen in Figure 40, the nanoparticles appear to be smaller and have a narrower size distribution at shorter reaction time. The difference in size as the reaction time increases can be explained by the nucleation and growth theory. These NPs are able to suspend in nonpolar solvents shown in Figure 40(d). The NPs that are synthesized at shorter time periods are the less stable kinetic product

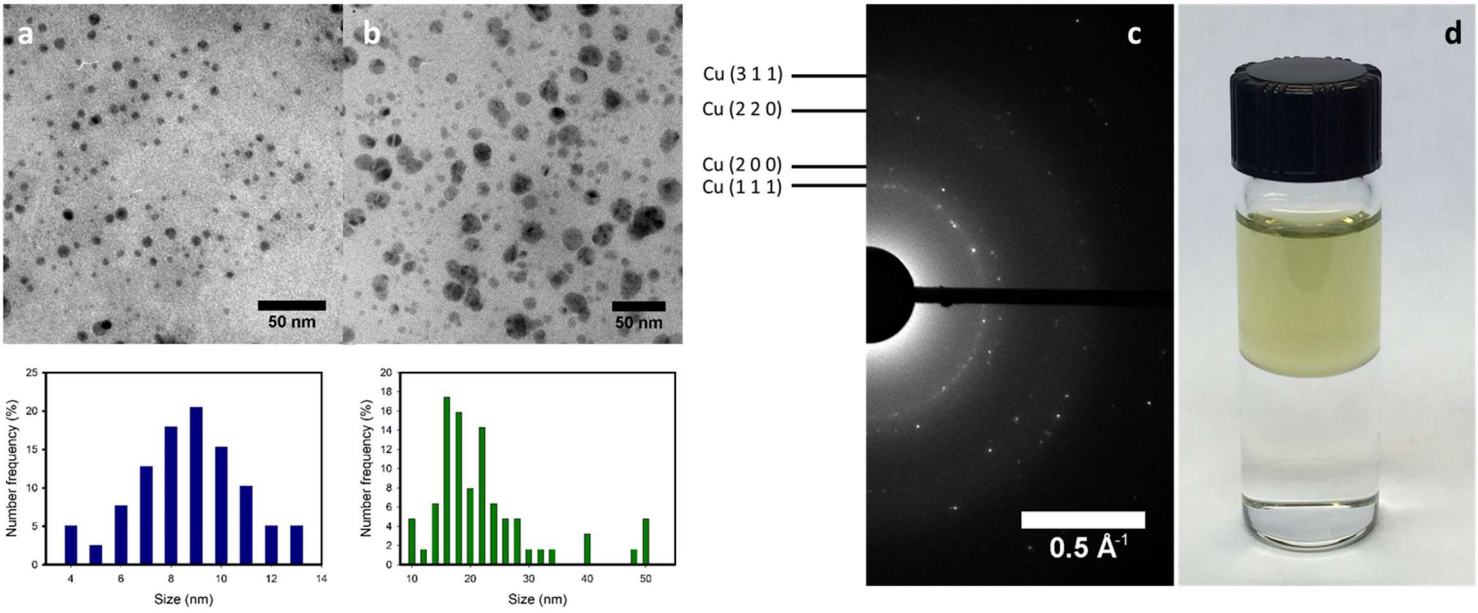

Figure 40. TEM images of the Cu nanoparticles at various reaction times (a) 12 mins, (b) 14 mins, (c) diffraction pattern of the particles synthesized for 14 mins, and (d) colloidal suspension of the Cu NPs shown in a, bottom phase consist of water and top phase.

and as the reaction time increase the larger thermodynamic products are formed. The diffraction image in Figure 40(c) originates from a number of particles and showed the diffraction ring of metallic copper.

Figure 41(a) shows XRD patterns of the samples synthesized from Cu acetate by changing the molar ratio of capping agents and time. All samples are kept at 1:2:1.5 Cu acetate, HEDHP, and OAm molar ratio to study the effect of particle size and morphology as time progress. Since the particles at 12 mins are of colloidal NPs, XRD sample preparation was done by drop casting on the XRD sample holder. Figure 40 shows that at 12 mins, the particles showed a mixed phase XRD pattern of Cu_2O, Cu, and $Cu_2P_2O_7$. The peaks of Cu_2O appears to be shifted toward the $Cu_2P_2O_7$ phase, suggesting the possibility of alloying in this system. In addition, the peak at 50.4° appears to match the Cu diffraction pattern. However, due to the low intensity of the pattern it was difficult to confirm the Cu phase by one single peak. As the reaction time increased to 20 minutes, the $Cu_2P_2O_7$ phase became more prominent and the particles are made of a mixed phase of $Cu_2P_2O_7$

(40%) and Cu (60%). SEM images of these particles (Figure 41b) reveal ~200 nm cubic particles. At 40 minutes, the particles showed a 100% fcc-Cu structure. On the other hand, (Figure 41c) the particles showed a mix phase of plates and spherical particles. The particles were examined using SEM-EDX elemental mapping, and the results showed that the plates are of phosphorus rich phase. Since the phosphorus is absent from the XRD results, suggesting that the plates are made of amorphous materials.

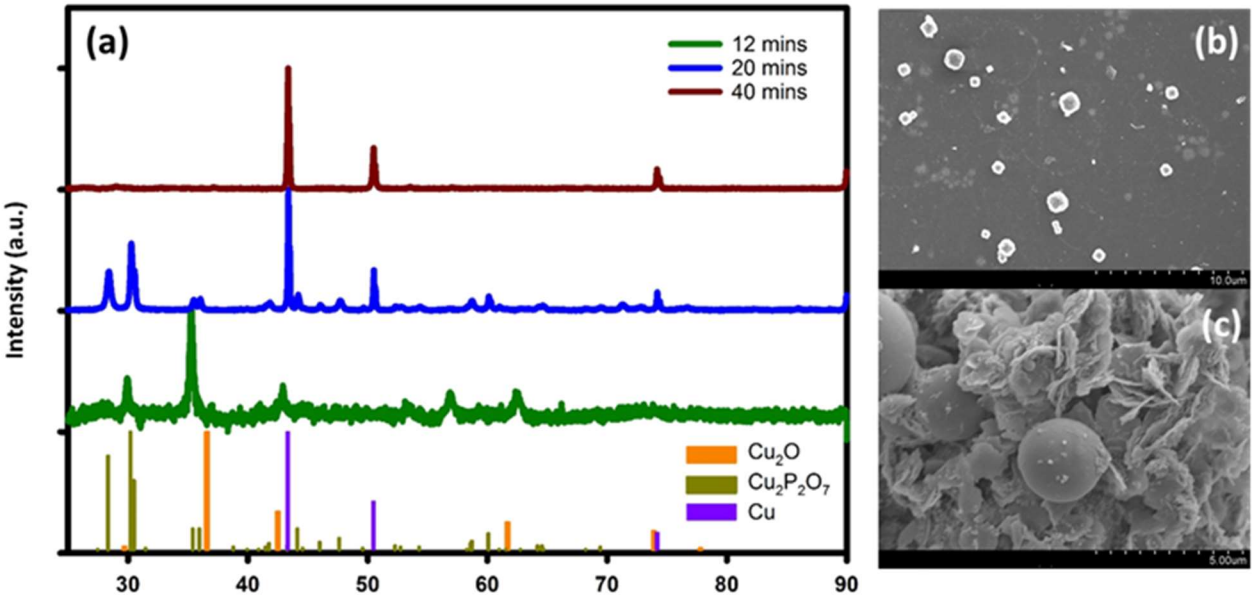

Figure 41. (a) XRD patterns of the samples synthesized by changing the reaction time, (b) SEM image of particles at 20 mins, and (c) SEM image of particles at 40 mins.

A.1.4.2. Tribological property and characterization of metal / metal oxide nanoparticles on stainless steel surface

Representative TEM image of Cu, CeO_2, and Fe_3O_4 nanoparticles there were used to study the friction and wear properties of stainless steel were shown in Figure 42. These samples were selected due to the similarities in size and morphology in order to provide comparable result base on the material used in this study. The crystal phase identification of the materials were confirmed

using electron diffraction for Cu NPs as shown in Figure 40(c), powdered x-ray diffraction for CeO_2 and Fe_3O_4 nanoparticles.

Table 10. Friction coefficient results from HFRR measurement of lubricant additives on stainless steel at various temperatures.

Additive	Loading	μ at 70°C	μ at 100°C	μ at 130°C
PAO Base oil	-	0.187	0.252	0.351
Cu (10 nm)	0.01%	0.177	0.235	0.316
Cu (10 nm)	0.50%	0.169	0.172	0.173
Cu (30 nm)	0.01%	0.169	0.188	0.247
Cu (30 nm)	0.50%	0.145	0.137	0.124
Cu (30 nm)	10%	0.117	0.118	0.1
CeO_2 (10 nm)	0.01%	0.182	0.254	0.34
CeO_2 (10 nm)	0.50%	0.182	0.206	0.244
CeO_2 (30 nm)	0.01%	0.166	0.221	0.204
CeO_2 (30 nm)	0.50%	0.204	0.167	0.148
Fe_3O_4 (10 nm)	0.01%	0.173	0.231	0.298
Fe_3O_4 (10 nm)	0.50%	0.167	0.279	0.326
Fe_3O_4 (25 nm)	0.01%	0.176	0.279	0.326
Fe_3O_4 (25 nm)	0.50%	0.139	0.146	0.137

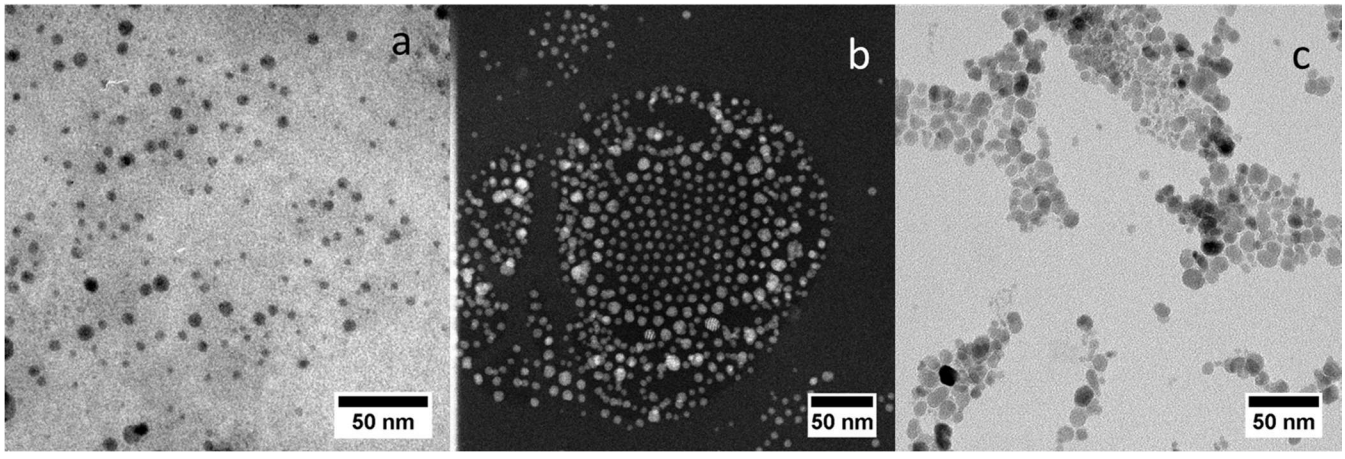

Figure 42. Representative TEM image (a) Cu NPs imaged using bright field (b) CeO_2 NPs imaged in dark field (c) Fe_3O_4 NPs imaged in bright field TEM.

Table 10 shows the performance of the lubricant additive in terms of coefficient of friction at various temperatures. Temperatures of 70 °C, 100 °C, and 130 °C were chosen to examine the friction coefficient because the temperature of auto engines typically operate between 90 – 105 °C. The based oil used to as a baseline of the measurement was SpectraSyn^{TM} 4 Polyalphaolefin (PAO) (ExxonMobil) without any additives. Based on the results from Table 10, the friction coefficient of PAO base oil increases as the temperature of the system increases, this is due to the increased viscosity of the base oil at higher temperatures. The coefficient of friction of the base oil without any nanoparticle additive appears to be generally higher in comparison to the addition of nanoparticles as additives with the exception of 0.5% loading of 30 nm CeO_2 particles as additives at 70 °C. From the results in Table 10, the coefficient of friction generally decrease with higher nanoparticle additive loading as well as larger particle size. For copper nanomaterials, previous studies have found that the lowest friction coefficient value of 0.247 was obtained from 3% CuO nanoparticles.[114] In this work, all the nanoparticles were surface modified by either bis-ethylhexyl phosphate, oleic acid, or oleylamine. The Cu / CuO nanoparticles was modified by bis-ethylhexyl phosphate resulting in friction coefficient as low as 0.124 with 0.5% loading of the Cu / CuO additive, indicating the surfactant plays an important role in reducing friction of the surface. It is noteworthy to mention that bare nanoparticles tend to agglomerate into larger particles and thus harder to disperse in non-polar solvent, therefore it can also alter the anti-wear properties of lubricants. Asadauskas et al. have previously reported that the nanoparticle stability of ZnO, CuO, and Fe NPs in which they have found that the Zn NP was the most stable in lubricant oil followed by CuO NPs.[121] However, it is still unclear if the instability of the material is due to the lack of

stabilizing or capping agent, as it have been shown in this work that it is a contributing factor in the colloidal properties.

Table 11. Wear scar diameter from HFRR measurement of lubricant additives on stainless steel at 100 °C, averaged between 2 measurements.

Additive	% additive loading	Wear Scar at 100°C (μm^2)
PAO Base oil	-	1816
Cu (10 nm)	0.01%	1685
Cu (10 nm)	0.50%	1532
Cu (30 nm)	0.01%	1374
Cu (30 nm)	0.50%	1285
Cu (30 nm)	10%	622
CeO_2 (10 nm)	0.01%	1787
CeO_2 (10 nm)	0.50%	1346
CeO_2 (30 nm)	0.01%	1211
CeO_2 (30 nm)	0.50%	1108
Fe_3O_4 (10 nm)	0.01%	1001
Fe_3O_4 (10 nm)	0.50%	1027
Fe_3O_4 (25 nm)	0.01%	1765
Fe_3O_4 (25 nm)	0.50%	2098

The average wear scar diameter of the nanoparticle lubrication additives are shown in Table 11. In general, it can be seen that the wear scar diameter decreases with the presence of Cu and CeO_2 NPs compared to the absence of additive. This observation agree with previous literature finding where the addition of nanomaterials decreases the wear scar diameter of the steel substrate.[122] However, anomaly is observed with Fe_3O_4 NPs as additives where increasing NP loading and NP size lead to larger wear scar in this system. This can be explained by the magnetic properties of the Fe_3O_4 on stainless steel surface acting as ball bearings between two interacting

surface resulting in a larger wear scar area. In addition, the hardness of Fe_3O_4 5.5-6.5 on the Moh scale hardness in comparison to Cu or CeO_2 with hardness value of 3.0-4.0 on the Moh hardness scale. This indicate that there are differences in the anti-wear mechanism of nanomaterial as lubricant additives.

Macroscopic studies in the literature have shown that lubrication additives such as zinc dialkyldithiophosphate (ZDDP) are known to decompose at the interacting interface, forming a protective layer known as tribofilm to reduce wear of moving parts.[123] In order to observe the tribofilm formation of the various nanoparticles, mini traction machine with spacer layer imaging method (MTM-SILM) was used to determine the thickness of the tribofilm. Typically, blue color indicate no tribofilm formed, as the tribofilm formed on the surface it changes from blue to orange and eventually to dark brown as the film thickness increase. Tribofilm formed on the surface of interest should be uniform and thin since tribofilm that are too thick will increase the friction coefficient of the interacting surface and uneven film will cause uneven wear pattern that can shorten the lifetime of the engine parts. In the observation of tribofilm formation, MTM-SLIM

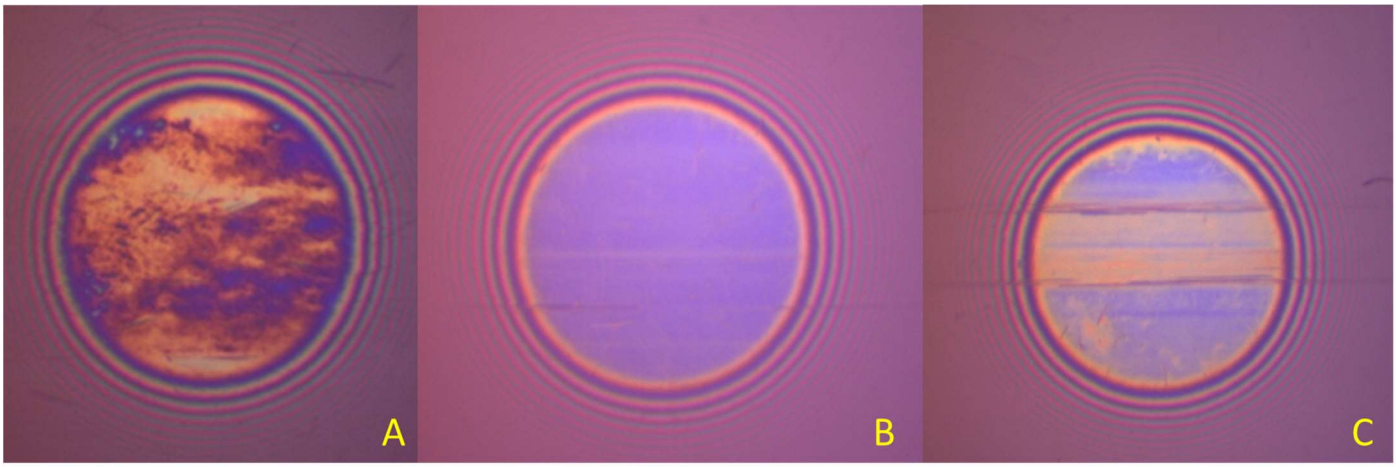

Figure 43. Mini traction machine with spacer layer imaging (MTM-SLIM) results. (a) 0.01% ZDDP as reference, (b) 0.01% 30 nm Cu loading, (c) 0.01% 30 nm CeO_2 loading.

images were obtained for ZDDP, as-synthesized Cu and CeO_2 NPs are shown in Figure 43. Fe_3O_4 sample was not subjected to MTM experiment due to the magnetic nature of the particles causing the instrument to seize up upon loading the Fe_3O_4 samples. ZDDP was chosen as a basis of comparison because it has been used in the lubricant industry since the late 1930s and still play an important role in reducing friction and wear in lubrication products nowadays.[124] From the MTM-SLIM analysis shown in Figure 43, the tribofilm formed using 0.01% ZDDP generated the thickest tribofilm in comparison to Cu and CeO_2. 0.01% Cu produced a minimal surface film where the color of the image only have a slight hint of orange. On the other hand, the addition of 0.01% CeO_2

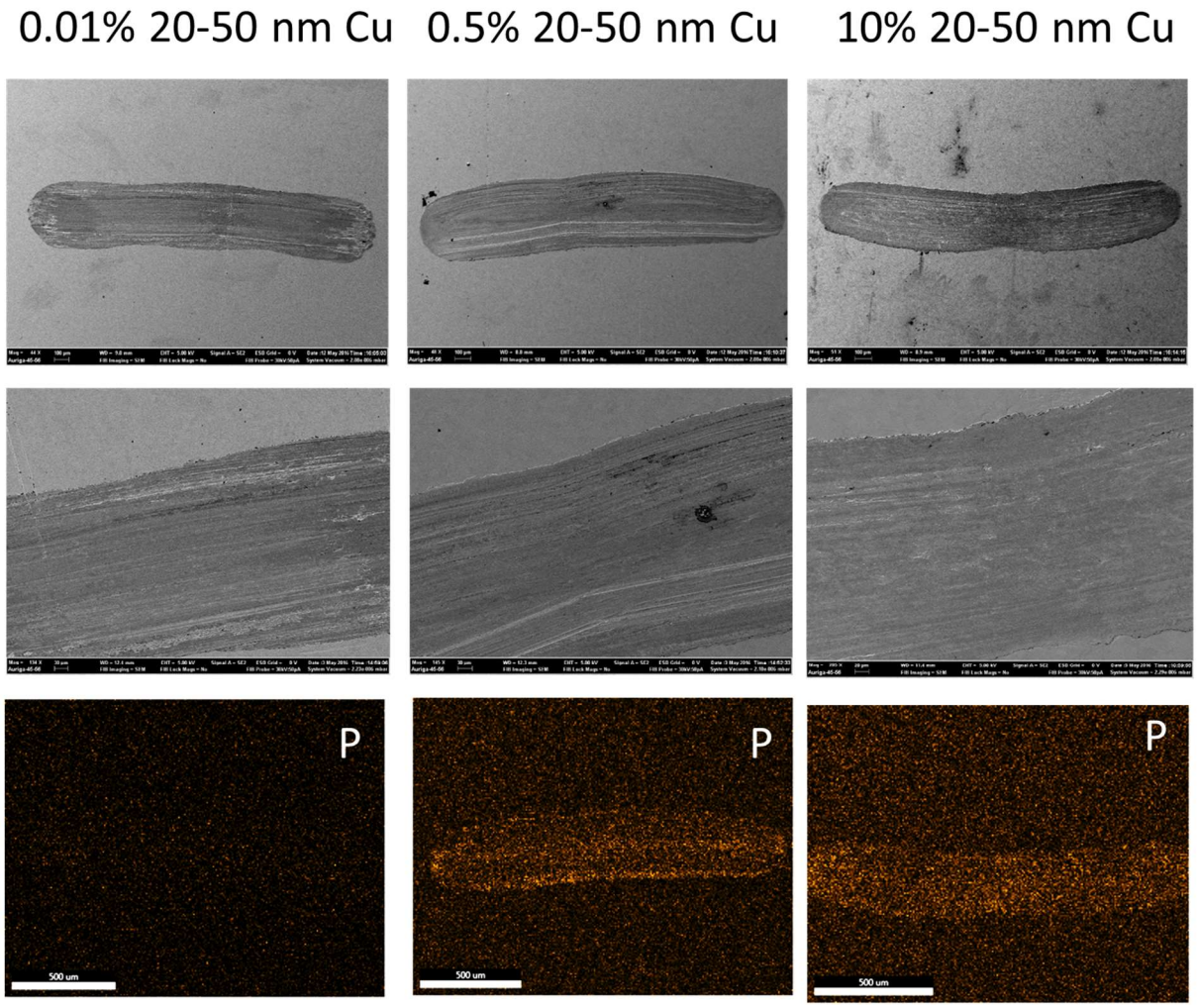

Figure 44. SEM surface analysis of HDEHP capped Cu at various magnifications and SEM-EDX elemental mapping of phosphorus on the surface.

to the PAO base oil created an uneven tribofilm on the steel balls of the MTM. This suggested that the anti-wear mechanism of nanoparticles vary from material to material where Cu formed no film on the surface and CeO_2 NPs formed an uneven film on the surface with similar particle size and additive loading.

SEM-EDX elemental mapping of Cu and Ce on HFRR wear disks shown in Figure 45 further suggest that the anti-wear properties of the two additives follow a different mechanism. In Figure 45, the Cu edx map showed an absence of Cu on the surface of the stainless steel whereas Ce EDS map showed the presence of Ce on the surface of the wear disk. Further SEM-E mapping of phosphorous presented in Figure 44 reveal Cu is acting as a delivery agent in the deposition of phosphate onto the surface of the stainless steel and thus repairing the surface of the steel as

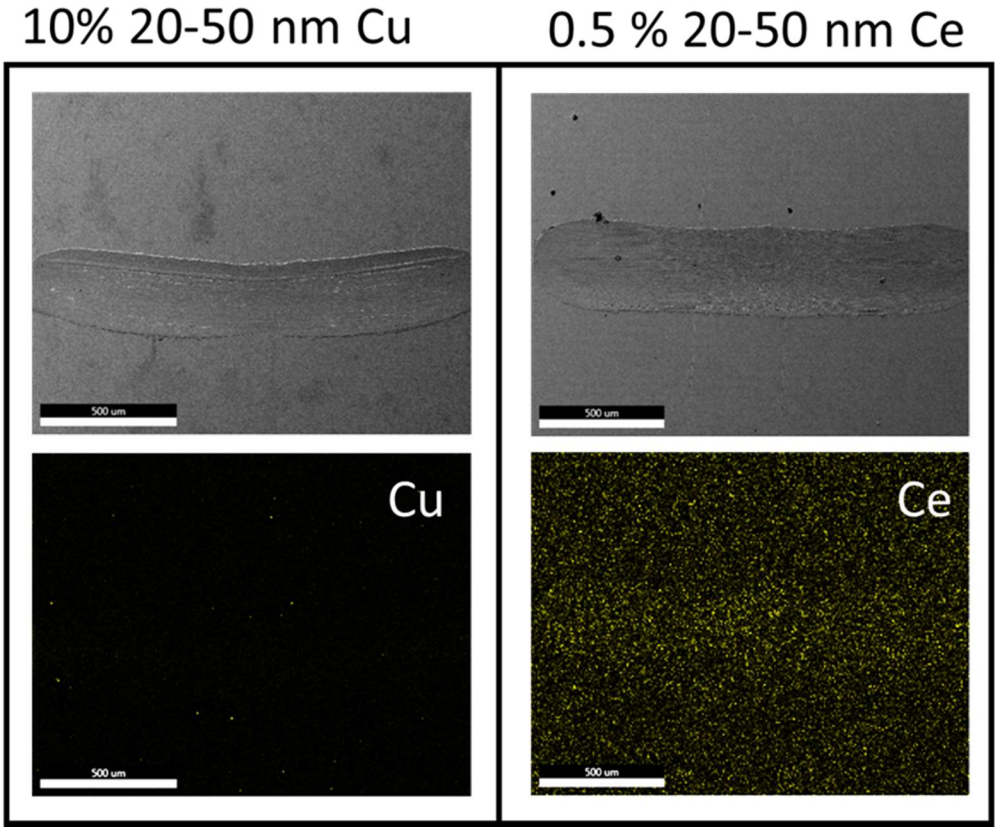

Figure 45. SEM surface analysis of Cu and ceria. SEM-EDX elemental mapping of Cu and Ce on the surface.

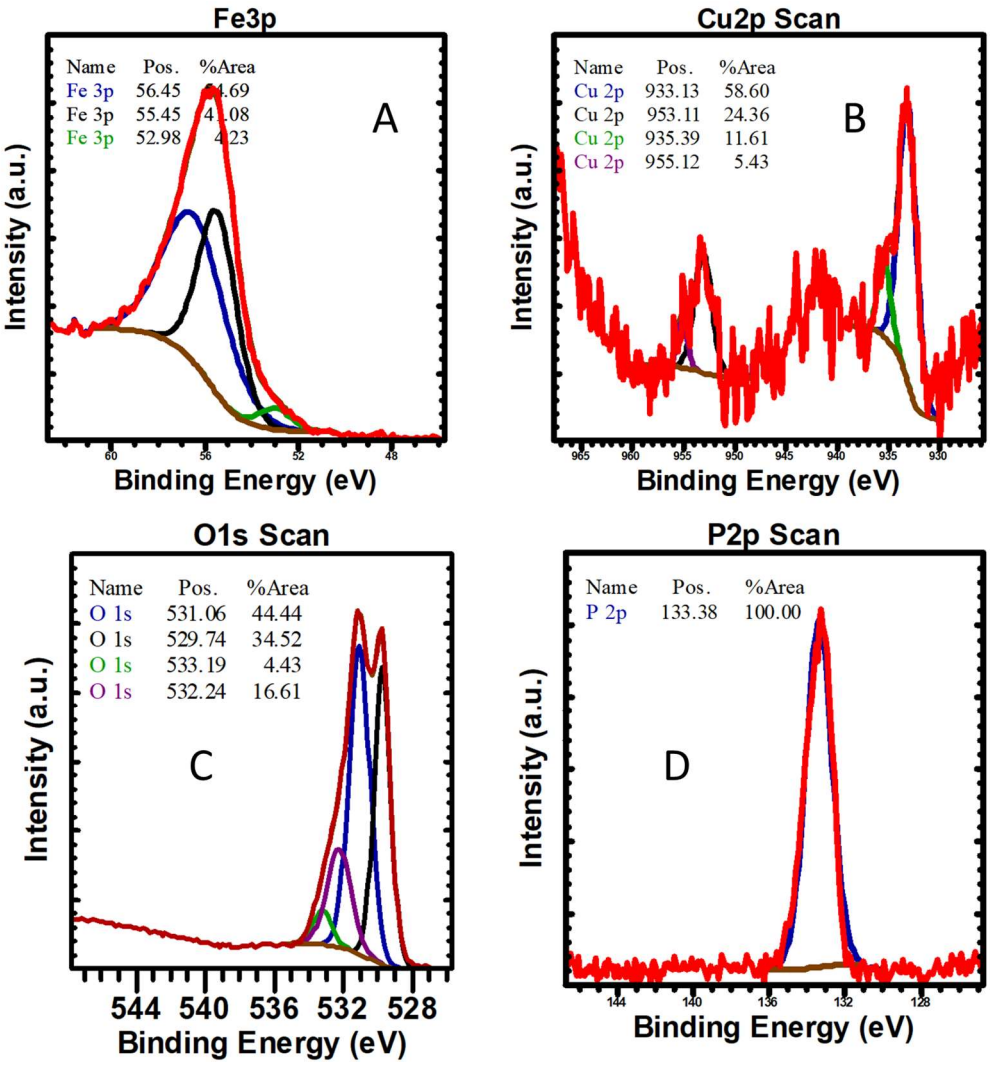

Figure 46. XPS spectra of the wear scar with 0.5% Cu additive.

suggested in the SEM images. On the other hand, the presence of Ce on surface of the stainless steel wear disk suggested that CeO_2 acts as a polishing agent where the surface of the steel is constantly polished by the CeO_2 in order to reduce friction.

X-ray photoelectron spectroscopy measurements were performed on 0.5% 20-50 nm Cu sample and 0.5% 20-50 nm Cu additive using ThermoFisher ESCAlab 250 with a monochromatic Al K_α. The XPS spectra from Figure 46 shows the surface chemistry of the wear scar by measuring the binding energies of iron, copper, oxygen, and phosphorus on the surface. Figure 46A shows the binding energies for iron in the 3p region where two distinct peaks appear at 56.45 eV and

55.45 eV, corresponding to Fe_2O_3 and Fe_3O_4 respectively.[125-126] The shoulder peak that occur at 52.98 eV was found to be corresponding to Fe^0 peak on the surface of the 315L stainless steel wear disk.[125] Likewise, Figure 46B shows the XPS spectrum for copper 2p region, where the peaks with binding energies of 953.11 eV and 933.1 eV correspond to $2p^{1/2}$ and $2p^{3/2}$ of Cu. Both of the Cu peaks contain shoulder peaks indicating the presence of two oxidation state of the Cu on the surface of the wear scar. The oxygen peak at 532.2 eV is associated to the C-O-P bonding between the C and P.[127] Figure 46D displays the binding energy of phosphorus 2p region where only one distinct peak appear at 133 eV region, this peak at 133.38 eV correspond to metaphosphate.[128] The XPS results agree with our SEM-EDS elemental mapping of phosphorus and copper of the wear scar. Further confirm are speculations on copper as a delivery agent to deliver surfactant onto the surface of the steel disc to protect the interacting parts.

A.1.5. Summary and Conclusions

Copper, cerium oxide, and iron oxide nanoparticles of various size have been synthesized and tested as lubricant additive into PAO 4 base oil. Through high frequency reciprocating rig testing, high loading of 25 nm iron oxide nanoparticles have shown the ability to reduce friction. However, due to its magnetic nature it causes the interacting parts to seize indicating that iron oxide is not an ideal candidate in reducing friction between parts. Mini traction machine was used to monitor the formation of tribofilm. The tribofilm formed using copper as an additive have shown minimal film formation with a uniform thickness, on the other hand cerium oxide additive have shown a thick and uneven film. These two types of nanoparticles have shown to form a thinner film In comparison to the ZDDP that is used in the current Industries. This results suggest that copper nanoparticles is a promising Material in reducing friction of the interacting surfaces. Based

on our SEM analysis of the surface of wear scars, we conclude that cerium oxide act as a polishing agent where it constantly removing material the between the interacting surfaces. On the other hand we conclude that copper act as a delivery agent to deposit the surfactant onto the surface the repairing the warn parts due to friction.

List of References

1. Gutfleisch, O.; Willard, M. A.; Brück, E.; Chen, C. H.; Sankar, S. G.; Liu, J. P., Magnetic Materials and Devices for the 21st Century: Stronger, Lighter, and More Energy Efficient. *Adv. Mater.* **2011**, *23*, 821-842.
2. Souza, C. G. S.; Beck, W.; Varanda, L. C., Multifunctional Luminomagnetic Fept@Fe3o4/Sio2/Rhodamine B/Sio2 Nanoparticles with High Magnetic Emanation for Biomedical Applications. *J. Nanopart. Res.* **2013**, *15*, 1545.
3. El-Gendy, A. A.; Almugaiteeb, T.; Carpenter, E. E., Coxc Nanorod Magnets: Highly Magnetocrystalline Anisotropy with Lower Curie Temperature for Potential Applications. *J. Magn. Magn. Mater.* **2013**, *348*, 136-139.
4. Zhong, L., et al., Cobalt Carbide Nanoprisms for Direct Production of Lower Olefins from Syngas. *Nature* **2016**, *538*, 84.
5. Clifford, D. M.; Castano, C. E.; Tsui, M. H. M.; Rojas, J. V.; Carpenter, E. E., Tailoring the Magnetic Properties of Fexco(1-X) Nanopowders Prepared by a Polyol Process. *Dalton Transactions* **2017**, *46*, 10364-10373.
6. Kramer, M. J.; McCallum, R. W.; Anderson, I. A.; Constantinides, S., Prospects for Non-Rare Earth Permanent Magnets for Traction Motors and Generators. *JOM* **2012**, *64*, 752-763.
7. Chu, S.; Majumdar, A., Opportunities and Challenges for a Sustainable Energy Future. *Nature* **2012**, *488*, 294.
8. Jiang, Y.; Mehedi, M. A.; Fu, E.; Wang, Y.; Allard, L. F.; Wang, J.-P., Synthesis of Fe16n2 Compound Free-Standing Foils with 20 Mgoe Magnetic Energy Product by Nitrogen Ion-Implantation. *Scientific Reports* **2016**, *6*, 25436.
9. Pecharsky, A. O.; Jr., K. A. G.; Pecharsky, V. K., The Giant Magnetocaloric Effect of Optimally Prepared Gd5si2ge2. *J. Appl. Phys.* **2003**, *93*, 4722-4728.
10. Pecharsky, V. K.; Gschneidner, J. K. A., Giant Magnetocaloric Effect in Gd5si2ge2. *Phys. Rev. Lett.* **1997**, *78*, 4494-4497.
11. Romero Gómez, J.; Ferreiro Garcia, R.; De Miguel Catoira, A.; Romero Gómez, M., Magnetocaloric Effect: A Review of the Thermodynamic Cycles in Magnetic Refrigeration. *Renew. Sust. Energ. Rev.* **2013**, *17*, 74-82.
12. Phan, M.-H.; Yu, S.-C., Review of the Magnetocaloric Effect in Manganite Materials. *J. Magn. Magn. Mater.* **2007**, *308*, 325-340.
13. Coey, J. M. D., *Magnetism and Magnetic Materials*; Cambridge University Press, 2010.
14. Zhang, H.; Peng, S.; Rong, C.-b.; Liu, J. P.; Zhang, Y.; Kramer, M. J.; Sun, S., Chemical Synthesis of Hard Magnetic Smco Nanoparticles. *J. Mater. Chem.* **2011**, *21*, 16873-16876.
15. Saguchi, A.; Uesugi, T.; Takigawa, Y.; Higashi, K., Development of Highly Efficient Saving Processes of Rare Earth in R-T-B Permanent Magnet. *Physics Procedia* **2014**, *54*, 168-173.
16. Anderson, I. E.; Kassen, A. G.; White, E. M. H.; Zhou, L.; Tang, W.; Palasyuk, A.; Dennis, K. W.; McCallum, R. W.; Kramer, M. J., Novel Pre-Alloyed Powder Processing of Modified Alnico 8: Correlation of Microstructure and Magnetic Properties. *J. Appl. Phys.* **2015**, *117*, 17D138.
17. Pecharsky, V. K.; Gschneidner Jr, K. A., Magnetocaloric Effect and Magnetic Refrigeration. *J. Magn. Magn. Mater.* **1999**, *200*, 44-56.

18. Warburg, E.; Hönig, L., Ueber Die Wärme, Welche Durch Periodisch Wechselnde Magnetisirende Kräfte Im Eisen Erzeugt Wird. *Annalen der Physik* **1883**, *256*, 814-835.
19. Pecharsky, V. K.; Gschneidner, K. A.; Pecharsky, A. O.; Tishin, A. M., Thermodynamics of the Magnetocaloric Effect. *Phys. Rev. B* **2001**, *64*, 144406.
20. Pecharsky, V. K.; Jr., K. A. G., Some Common Misconceptions Concerning Magnetic Refrigerant Materials. *J. Appl. Phys.* **2001**, *90*, 4614-4622.
21. Pecharsky, V. K.; Gschneidner, K. A.; Mudryk, Y.; Paudyal, D., Making the Most of the Magnetic and Lattice Entropy Changes. *J. Magn. Magn. Mater.* **2009**, *321*, 3541-3547.
22. Tegus, O.; Brück, E.; Zhang, L.; Dagula; Buschow, K. H. J.; de Boer, F. R., Magnetic-Phase Transitions and Magnetocaloric Effects. *Physica B: Condensed Matter* **2002**, *319*, 174-192.
23. Hueso, L. E.; Sande, P.; Miguéns, D. R.; Rivas, J.; Rivadulla, F.; López-Quintela, M. A., Tuning of the Magnetocaloric Effect in La0.67ca0.33mno3−Δ Nanoparticles Synthesized by Sol–Gel Techniques. *J. Appl. Phys.* **2002**, *91*, 9943-9947.
24. Pecharsky, V. K.; Gschneidner, K. A., Tunable Magnetic Regenerator Alloys with a Giant Magnetocaloric Effect for Magnetic Refrigeration from ∼20 to ∼290 K. *Appl. Phys. Lett.* **1997**, *70*, 3299-3301.
25. Julia, L., Magnetocaloric Materials for Energy Efficient Cooling. *J. Phys. D: Appl. Phys.* **2017**, *50*, 053002.
26. Pecharsky, V. K.; Gschneidner, K. A., Gd5(Sixge1–X)4: An Extremum Material. *Adv. Mater.* **2001**, *13*, 683-686.
27. Lyubina, J., Recent Advances in the Microstructure Design of Materials for near Room Temperature Magnetic Cooling (Invited). *J. Appl. Phys.* **2011**, *109*, 07A902.
28. Hu, F.-x.; Shen, B.-g.; Sun, J.-r., Magnetic Entropy Change in Ni51.5mn22.7ga25.8 Alloy. *Appl. Phys. Lett.* **2000**, *76*, 3460-3462.
29. Brück, E.; Tegus, O.; Cam Thanh, D. T.; Trung, N. T.; Buschow, K. H. J., A Review on Mn Based Materials for Magnetic Refrigeration: Structure and Properties. *International Journal of Refrigeration* **2008**, *31*, 763-770.
30. Dan'kov, S. Y.; Tishin, A. M.; Pecharsky, V. K.; Gschneidner, K. A., Magnetic Phase Transitions and the Magnetothermal Properties of Gadolinium. *Phys. Rev. B* **1998**, *57*, 3478-3490.
31. Zhang, L.; Bao, M.; Zheng, Q.; Tian, L.; Du, J., Magnetocaloric Effect in High Gd Content Gd-Fe-Al Based Amorphous/Nanocrystalline Systems with Enhanced Curie Temperature and Refrigeration Capacity. *AIP Advances* **2016**, *6*, 035220.
32. Rudolph, K.; Pathak, A. K.; Mudryk, Y.; Pecharsky, V. K., Magnetostructural Phase Transitions and Magnetocaloric Effect in (Gd5-Xscx)Si1.8ge2.2. *Acta Mater.* **2018**, *145*, 369-376.
33. Law, J. Y.; Franco, V.; Ramanujan, R. V., Direct Magnetocaloric Measurements of Fe-B-Cr-X (X = La, Ce) Amorphous Ribbons. *J. Appl. Phys.* **2011**, *110*, 023907.
34. Pękała, M.; Drozd, V.; Fagnard, J. F.; Vanderbemden, P., Magnetocaloric Effect in Nano- and Polycrystalline Manganites La0.5ca0.5mno3. *J. Alloys Compd.* **2010**, *507*, 350-355.
35. Andrade, V. M.; Vivas, R. J. C.; Pedro, S. S.; Tedesco, J. C. G.; Rossi, A. L.; Coelho, A. A.; Rocco, D. L.; Reis, M. S., Magnetic and Magnetocaloric Properties of La0.6ca0.4mno3 Tunable by Particle Size and Dimensionality. *Acta Mater.* **2016**, *102*, 49-55.
36. Xi, S.; Lu, W.; Sun, Y., Magnetic Properties and Magnetocaloric Effect of La0.8ca0.2mno3 Nanoparticles Tuned by Particle Size. *J. Appl. Phys.* **2012**, *111*, 063922.

37. Biswas, A.; Chandra, S.; Phan, M.-H.; Srikanth, H., Magnetocaloric Properties of Nanocrystalline Lamno3: Enhancement of Refrigerant Capacity and Relative Cooling Power. *J. Alloys Compd.* **2012**, *545*, 157-161.
38. Pękała, M.; Pękała, K.; Drozd, V.; Fagnard, J. F.; Vanderbemden, P., Magnetocaloric Effect in La0.75sr0.25mno3 Manganite. *J. Magn. Magn. Mater.* **2010**, *322*, 3460-3463.
39. Zhong, W.; Chen, W.; Ding, W.; Zhang, N.; Du, Y.; Yan, Q., Magnetocaloric Properties of Na-Substituted Perovskite-Type Manganese Oxides. *Solid State Commun.* **1998**, *106*, 55-58.
40. Fujita, A.; Fujieda, S.; Hasegawa, Y.; Fukamichi, K., Itinerant-Electron Metamagnetic Transition and Large Magnetocaloric Effects in La(Fexsi(1-X})13 Compounds and Their Hydrides. *Phys. Rev. B* **2003**, *67*, 104416.
41. Choi, Y.; Suresh, S., Size Effects on the Mechanical Properties of Thin Polycrystalline Metal Films on Substrates. *Acta Mater.* **2002**, *50*, 1881-1893.
42. Mandal, K.; Pal, D.; Gutfleisch, O.; Kerschl, P.; Müller, K.-H., Magnetocaloric Effect in Reactively-Milled Lafe11.57si1.43hy Intermetallic Compounds. *J. Appl. Phys.* **2007**, *102*, 053906.
43. Manosa, L.; Planes, A.; Acet, M., Advanced Materials for Solid-State Refrigeration. *Journal of Materials Chemistry A* **2013**, *1*, 4925-4936.
44. Mañosa, L.; Moya, X.; Planes, A.; Krenke, T.; Acet, M.; Wassermann, E. F., Ni–Mn-Based Magnetic Shape Memory Alloys: Magnetic Properties and Martensitic Transition. *Mater. Sci. Eng. A.* **2008**, *481-482*, 49-56.
45. Liu, J.; Gottschall, T.; Skokov, K. P.; Moore, J. D.; Gutfleisch, O., Giant Magnetocaloric Effect Driven by Structural Transitions. *Nature Materials* **2012**, *11*, 620.
46. Krenke, T.; Duman, E.; Acet, M.; Wassermann, E. F.; Moya, X.; Mañosa, L.; Planes, A.; Suard, E.; Ouladdiaf, B., Magnetic Superelasticity and Inverse Magnetocaloric Effect in Ni-Mn-In. *Phys. Rev. B* **2007**, *75*, 104414.
47. Krenke, T.; Duman, E.; Acet, M.; Wassermann, E. F.; Moya, X.; Mañosa, L.; Planes, A., Inverse Magnetocaloric Effect in Ferromagnetic Ni–Mn–Sn Alloys. *Nature Materials* **2005**, *4*, 450.
48. Booth, C. H.; Bridges, F.; Snyder, G. J.; Geballe, T. H., Evidence of Magnetization-Dependent Polaron Distortion in La1-Xaxmno3 a=Ca, Pb). *Phys. Rev. B* **1996**, *54*, R15606-R15609.
49. LaMer, V. K.; Dinegar, R. H., Theory, Production and Mechanism of Formation of Monodispersed Hydrosols. *J. Am. Chem. Soc.* **1950**, *72*, 4847-4854.
50. van Embden, J.; Chesman, A. S. R.; Jasieniak, J. J., The Heat-up Synthesis of Colloidal Nanocrystals. *Chem. Mater.* **2015**, *27*, 2246-2285.
51. Pearson, R. G., Hard and Soft Acids and Bases. *J. Am. Chem. Soc.* **1963**, *85*, 3533-3539.
52. Seo, W. S.; Shim, J. H.; Oh, S. J.; Lee, E. K.; Hur, N. H.; Park, J. T., Phase- and Size-Controlled Synthesis of Hexagonal and Cubic Coo Nanocrystals. *J. Am. Chem. Soc.* **2005**, *127*, 6188-6189.
53. Ghezelbash, A.; Korgel, B. A., Nickel Sulfide and Copper Sulfide Nanocrystal Synthesis and Polymorphism. *Langmuir* **2005**, *21*, 9451-9456.
54. Gu, H.; Soucek, M. D., Preparation and Characterization of Monodisperse Cerium Oxide Nanoparticles in Hydrocarbon Solvents. *Chem. Mater.* **2007**, *19*, 1103-1110.
55. Williams, B.; Clifford, D.; El-Gendy, A. A.; Carpenter, E. E., Solvothermal Synthesis of Fe7c3 and Fe3c Nanostructures with Phase and Morphology Control. *J. Appl. Phys.* **2016**, *120*, 033904.

56. Chang, S.-H.; Lu, M.-D.; Tung, Y.-L.; Tuan, H.-Y., Gram-Scale Synthesis of Catalytic Co9s8 Nanocrystal Ink as a Cathode Material for Spray-Deposited, Large-Area Dye-Sensitized Solar Cells. *ACS Nano* **2013**, *7*, 9443-9451.
57. Li, L.; Reiss, P., One-Pot Synthesis of Highly Luminescent Inp/Zns Nanocrystals without Precursor Injection. *J. Am. Chem. Soc.* **2008**, *130*, 11588-11589.
58. Fievet, F.; Lagier, J. P.; Blin, B.; Beaudoin, B.; Figlarz, M., Homogeneous and Heterogeneous Nucleations in the Polyol Process for the Preparation of Micron and Submicron Size Metal Particles. *Solid State Ionics* **1989**, *32*, 198-205.
59. Fievet, F.; Fievet-Vincent, F.; Lagier, J.-P.; Dumont, B.; Figlarz, M., Controlled Nucleation and Growth of Micrometre-Size Copper Particles Prepared by the Polyol Process. *J. Mater. Chem.* **1993**, *3*, 627-632.
60. Dong, H.; Chen, Y. C.; Feldmann, C., Polyol Synthesis of Nanoparticles: Status and Options Regarding Metals, Oxides, Chalcogenides, and Non-Metal Elements. *Green Chemistry* **2015**, *17*, 4107-4132.
61. Ducamp-Sanguesa, C.; Herrera-Urbina, R.; Figlarz, M., Synthesis and Characterization of Fine and Monodisperse Silver Particles of Uniform Shape. *J. Solid State Chem.* **1992**, *100*, 272-280.
62. Hachani, R.; Lowdell, M.; Birchall, M.; Hervault, A.; Mertz, D.; Begin-Colin, S.; Thanh, N. T. K., Polyol Synthesis, Functionalisation, and Biocompatibility Studies of Superparamagnetic Iron Oxide Nanoparticles as Potential Mri Contrast Agents. *Nanoscale* **2016**, *8*, 3278-3287.
63. Huba, Z. J.; Carpenter, E. E., Size and Phase Control of Cobalt–Carbide Nanoparticles Using Oh− and Cl− Anions in a Polyol Process. *J. Appl. Phys.* **2012**, *111*, 07B529.
64. Ammar, S.; Helfen, A.; Jouini, N.; Fievet, F.; Rosenman, I.; Villain, F.; Molinie, P.; Danot, M., Magnetic Properties of Ultrafine Cobalt Ferrite Particles Synthesized by Hydrolysis in a Polyol Medium. *J. Mater. Chem.* **2001**, *11*, 186-192.
65. Jézéquel, D.; Guenot, J.; Jouini, N.; Fiévet, F., Submicrometer Zinc Oxide Particles: Elaboration in Polyol Medium and Morphological Characteristics. *J. Mater. Res.* **1995**, *10*, 77-83.
66. Souad, A.; Noureddine, J.; Fernand, F.; Zyed, B.; Leila, S.; Philippe, M.; Michel, D.; Jean-Marc, G., Magnetic Properties of Zinc Ferrite Nanoparticles Synthesized by Hydrolysis in a Polyol Medium. *J. Phys.: Condens. Matter* **2006**, *18*, 9055.
67. Viau, G.; Fievet-Vincent, F.; Fievet, F., Monodisperse Iron-Based Particles: Precipitation in Liquid Polyols. *J. Mater. Chem.* **1996**, *6*, 1047-1053.
68. Adekoya, J. A.; Mlowe, S.; Dare, E. O.; Mesubi, M. A.; Revaprasadu, N., Synthesis and Characterization of Polyol Stabilised Ag/Co Allied Nanocomposites. *Superlattices Microstruct.* **2015**, *78*, 97-105.
69. Fujieda, S.; Shinoda, K.; Suzuki, S.; Jeyadevan, B., Synthesis of Ni Carbide Nanoparticles with Ni3ctype Structure in Polyol Solution Containing Dispersant. *MATERIALS TRANSACTIONS* **2012**, *53*, 1716-1720.
70. Harris, V. G., et al., High Coercivity Cobalt Carbide Nanoparticles Processed Via Polyol Reaction: A New Permanent Magnet Material. *J. Phys. D: Appl. Phys.* **2010**, *43*, 165003.
71. Yang, W.; Rehman, S.; Chu, X.; Hou, Y.; Gao, S., Transition Metal (Fe, Co and Ni) Carbide and Nitride Nanomaterials: Structure, Chemical Synthesis and Applications. *ChemNanoMat* **2015**, *1*, 376-398.

72. Ebelmen, *Recherches Sur Les Combinaisons Des Acides Borique Et Silicique Avec Les Éthers*, 1846.
73. Avnir, D.; Coradin, T.; Lev, O.; Livage, J., Recent Bio-Applications of Sol-Gel Materials. *J. Mater. Chem.* **2006**, *16*, 1013-1030.
74. Livage, J.; Sanchez, C., Sol-Gel Chemistry. *J. Non-Cryst. Solids* **1992**, *145*, 11-19.
75. Fricke, J.; Emmerling, A., Aerogels. *Adv. Mater.* **1991**, *3*, 504-506.
76. Hench, L. L.; West, J. K., The Sol-Gel Process. *Chem. Rev.* **1990**, *90*, 33-72.
77. Glaves, C. L.; Brinker, C. J.; Smith, D. M.; Davis, P. J., In Situ Pore Structure Studies of Xerogel Drying. *Chem. Mater.* **1989**, *1*, 34-40.
78. Poelz, G.; Riethmüller, R., Preparation of Silica Aerogel for Cherenkov Counters. *Nuclear Instruments and Methods in Physics Research* **1982**, *195*, 491-503.
79. Audebert, P.; Griesmar, P.; Hapiot, P.; Sanchez, C., Sol-Gel-Xerogel Evolution Investigated by Electroactive Probes in Silica and Transition-Metal Oxide Based Gels. *J. Mater. Chem.* **1992**, *2*, 1293-1300.
80. Chen, D.-H.; He, X.-R., Synthesis of Nickel Ferrite Nanoparticles by Sol-Gel Method. *Mater. Res. Bull.* **2001**, *36*, 1369-1377.
81. Danks, A. E.; Hall, S. R.; Schnepp, Z., The Evolution of 'Sol-Gel' Chemistry as a Technique for Materials Synthesis. *Mater. Horiz.* **2016**, *3*, 91-112.
82. Lin, J.; Yu, M.; Lin, C.; Liu, X., Multiform Oxide Optical Materials Via the Versatile Pechini-Type Sol−Gel Process: Synthesis and Characteristics. *The Journal of Physical Chemistry C* **2007**, *111*, 5835-5845.
83. Cushing, B. L.; Kolesnichenko, V. L.; O'Connor, C. J., Recent Advances in the Liquid-Phase Syntheses of Inorganic Nanoparticles. *Chem. Rev.* **2004**, *104*, 3893-3946.
84. Pandey, S.; Mishra, S. B., Sol–Gel Derived Organic–Inorganic Hybrid Materials: Synthesis, Characterizations and Applications. *J. Sol-Gel Sci. Technol.* **2011**, *59*, 73-94.
85. Waseda, Y.; Matsubara, E.; Shinoda, K., *X-Ray Diffraction Crystallography*; Springer: Verlag Berlin Heidelberg, 2011, p 210.
86. Rietveld, H. M., A Profile Refinement Method for Nuclear and Magnetic Structures. *J. Appl. Crystallogr.* **1969**, *2*, 65-71.
87. Williams, D. B.; Carter, C. B., *Transmittion Electron Microscopy: A Textbook for Material Science*; Springer: New York, USA, 2009.
88. Narayan, P.; Liu, J. P., Advances in Nanostructured Permanent Magnets Research. *J. Phys. D: Appl. Phys.* **2013**, *46*, 043001.
89. Carroll, K. J.; Huba, Z. J.; Spurgeon, S. R.; Qian, M.; Khanna, S. N.; Hudgins, D. M.; Taheri, M. L.; Carpenter, E. E., Magnetic Properties of Co2c and Co3c Nanoparticles and Their Assemblies. *Appl. Phys. Lett.* **2012**, *101*, 012409.
90. Carroll, K. J.; Calvin, S.; Ekiert, T. F.; Unruh, K. M.; Carpenter, E. E., Selective Nucleation and Growth of Cu and Ni Core/Shell Nanoparticles. *Chem. Mater.* **2010**, *22*, 2175-2177.
91. Huba, Z. J.; Carpenter, E. E., A Versatile Synthetic Approach for the Synthesis of Coo, Coxc, and Co Based Nanocomposites: Tuning Kinetics and Crystal Phase with Different Polyhydric Alcohols. *CrystEngComm* **2014**, *16*, 8000-8007.
92. Joseyphus, R. J.; Matsumoto, T.; Takahashi, H.; Kodama, D.; Tohji, K.; Jeyadevan, B., Designed Synthesis of Cobalt and Its Alloys by Polyol Process. *J. Solid State Chem.* **2007**, *180*, 3008-3018.

93. El-Gendy, A. A.; Qian, M.; Huba, Z. J.; Khanna, S. N.; Carpenter, E. E., Enhanced Magnetic Anisotropy in Cobalt-Carbide Nanoparticles. *Appl. Phys. Lett.* **2014**, *104*, 023111.
94. Clifford, D. M.; Castano, C. E.; Lu, A. J.; Carpenter, E. E., Synthesis of Feco Alloy Magnetically Aligned Linear Chains by the Polyol Process: Structural and Magnetic Characterization. *Journal of Materials Chemistry C* **2015**, *3*, 11029-11035.
95. Maurer, T.; Zighem, F.; Fang, W.; Ott, F.; Chaboussant, G.; Soumare, Y.; Atmane, K. A.; Piquemal, J.-Y.; Viau, G., Dipolar Interactions in Magnetic Nanowire Aggregates. *J. Appl. Phys.* **2011**, *110*, 123924.
96. Meziane, L.; Salzemann, C.; Aubert, C.; Gerard, H.; Petit, C.; Petit, M., Hcp Cobalt Nanocrystals with High Magnetic Anisotropy Prepared by Easy One-Pot Synthesis. *Nanoscale* **2016**, *8*, 18640-18645.
97. Soumare, Y.; Piquemal, J. Y.; Maurer, T.; Ott, F.; Chaboussant, G.; Falqui, A.; Viau, G., Oriented Magnetic Nanowires with High Coercivity. *J. Mater. Chem.* **2008**, *18*, 5696-5702.
98. Ott, F.; Maurer, T.; Chaboussant, G.; Soumare, Y.; Piquemal, J. Y.; Viau, G., Effects of the Shape of Elongated Magnetic Particles on the Coercive Field. *J. Appl. Phys.* **2009**, *105*, 013915.
99. Stoner, E. C. W., E.P., A Mechanism of Magnetic Hysteresis in Heterogeneous Alloys. *Philosophical Transactions of the Royal Society of London. Series A, Mathematical and Physical Sciences* **1948**, *240*, 599-642.
100. Baletto, F.; Rapallo, A.; Rossi, G.; Ferrando, R., Dynamical Effects in the Formation of Magic Cluster Structures. *Phys. Rev. B* **2004**, *69*, 235421.
101. Zamanpour, M.; Bennett, S. P.; Majidi, L.; Chen, Y.; Harris, V. G., Process Optimization and Properties of Magnetically Hard Cobalt Carbide Nanoparticles Via Modified Polyol Method. *J. Alloys Compd.* **2015**, *625*, 138-143.
102. Lebedev, O. I.; Van Tendeloo, G.; Amelinckx, S.; Leibold, B.; Habermeier, H. U., Structure and Microstructure of ${\Mathrm{La}}_{1\Ensuremath{-}X}{\Mathrm{Ca}}_{X}{\Mathrm{Mno}}_{3\Mathrm{\Ensuremath{-}}}\Mathrm{\Ensuremath{\Delta}}}$ Thin Films Prepared by Pulsed Laser Deposition. *Phys. Rev. B* **1998**, *58*, 8065-8074.
103. Pękała, M.; Drozd, V.; Fagnard, J. F.; Vanderbemden, P.; Ausloos, M., Magnetocaloric Effect in Nano- and Polycrystalline Manganite La0.7ca0.3mno3. *Appl. Phys. A* **2008**, *90*, 237-241.
104. Phan, M.-H.; Yu, S.-C.; Hur, N. H.; Jeong, Y.-H., Large Magnetocaloric Effect in a La0.7ca0.3mno3 Single Crystal. *J. Appl. Phys.* **2004**, *96*, 1154-1158.
105. Gencer, H.; Cengiz, N. E.; Kolat, V. S.; Izgi, T.; Atalay, S., Production of Lacamno3 Composite by Ball Milling. *Acta Phys. Pol., A* **2014**, *125*, 214-216.
106. Wang, X.; Wang, M.; Song, H.; Ding, B., A Simple Sol–Gel Technique for Preparing Lanthanum Oxide Nanopowders. *Mater. Lett.* **2006**, *60*, 2261-2265.
107. Schiffer, P.; Ramirez, A.; Bao, W.; Cheong, S., Low Temperature Magnetoresistance and the Magnetic Phase Diagram of La 1− X Ca X Mno 3. *Phys. Rev. Lett.* **1995**, *75*, 3336.
108. Kim, K. H.; Gu, J. Y.; Choi, H. S.; Park, G. W.; Noh, T. W., Frequency Shifts of the Internal Phonon Modes in ${\Mathrm{La}}_{0.7}$${\Mathrm{Ca}}_{0.3}Mn{\Mathrm{O}}_{3}$. *Phys. Rev. Lett.* **1996**, *77*, 1877-1880.

109. Lampen, P.; Bingham, N. S.; Phan, M. H.; Kim, H.; Osofsky, M.; Piqué, A.; Phan, T. L.; Yu, S. C.; Srikanth, H., Impact of Reduced Dimensionality on the Magnetic and Magnetocaloric Response of La0.7ca0.3mno3. *Appl. Phys. Lett.* **2013**, *102*, 062414.
110. Pękała, M., Magnetic Field Dependence of Magnetic Entropy Change in Nanocrystalline and Polycrystalline Manganites La1−Xmxmno3 (M=Ca,Sr). *J. Appl. Phys.* **2010**, *108*, 113913.
111. Oesterreicher, H.; Parker, F. T., Magnetic Cooling near Curie Temperatures above 300 K. *J. Appl. Phys.* **1984**, *55*, 4334-4338.
112. Zeng, H.; Zhang, J.; Kuang, C.; Yue, M., Magnetic Entropy Change in Bulk Nanocrystalline Gd Metals. *Applied Nanoscience* **2011**, *1*, 51-57.
113. Martin, J. M.; Ohmae, N., *Nanolubricants*; John Wiley & Sons, Ltd, 2008.
114. Asrul, M.; Zulkifli, N. W. M.; Masjuki, H. H.; Kalam, M. A., Tribological Properties and Lubricant Mechanism of Nanoparticle in Engine Oil. *Procedia Engineering* **2013**, *68*, 320-325.
115. Tung, S. C.; McMillan, M. L., Automotive Tribology Overview of Current Advances and Challenges for the Future. *Tribol. Int.* **2004**, *37*, 517-536.
116. Holmberg, K.; Ronkainen, H.; Laukkanen, A.; Wallin, K., Friction and Wear of Coated Surfaces — Scales, Modelling and Simulation of Tribomechanisms. *Surf. Coat. Technol.* **2007**, *202*, 1034-1049.
117. Morina, A.; Green, J. H.; Neville, A.; Priest, M., Surface and Tribological Characteristics of Tribofilms Formed in the Boundary Lubrication Regime with Application to Internal Combustion Engines. *Tribol. Lett.*, *15*, 443-452.
118. Viesca, J. L.; Battez, A. H.; Gonzalez, R.; Chou, R.; Cabello, J. J., Antiwear Properties of Carbon-Coated Copper Nanoparticles Used as an Additive to a Polyalphaolefin. *Tribol. Int.* **2011**, *44*, 829-833.
119. Battez, A. H.; Viesca, J. L.; Gonzalez, R.; Blanco, D.; Asedegbega, E.; Osorio, A., Friction Reduction Properties of a Cuo Nanolubricant Used as Lubricant for a Nicrbsi Coating. *Wear* **2010**, *268*, 325-328.
120. Thottackkad, M. V.; Rajendrakumar, P.; Prabhakaran, N., Tribological Analysis of Surfactant Modified Nanolubricants Containing Ceo2 Nanoparticles. *Tribology-Materials, Surfaces & Interfaces* **2014**, *8*, 125-130.
121. Asadauskas, S. J.; Kreivaitis, R.; Bikulčius, G.; Grigucevičienė, A.; Padgurskas, J., Tribological Effects of Cu, Fe and Zn Nano-Particles, Suspended in Mineral and Bio-Based Oils. *Lubr. Sci.* **2015**, n/a-n/a.
122. Li, B.; Wang, X.; Liu, W.; Xue, Q., Tribochemistry and Antiwear Mechanism of Organic–Inorganic Nanoparticles as Lubricant Additives. *Tribol. Lett.* **2006**, *22*, 79-84.
123. Carpick, R. W.; Salmeron, M., Scratching the Surface: Fundamental Investigations of Tribology with Atomic Force Microscopy. *Chem. Rev.* **1997**, *97*, 1163-1194.
124. Spikes, H., The History and Mechanisms of Zddp. *Tribol. Lett.* **2004**, *17*, 469-489.
125. Mills, P.; Sullivan, J. L., A Study of the Core Level Electrons in Iron and Its Three Oxides by Means of X-Ray Photoelectron Spectroscopy. *J. Phys. D: Appl. Phys.* **1983**, *16*, 723.
126. McIntyre, N. S.; Zetaruk, D. G., X-Ray Photoelectron Spectroscopic Studies of Iron Oxides. *Anal. Chem.* **1977**, *49*, 1521-1529.
127. Mishra, S.; Dwivedi, J.; Kumar, A.; Sankararamakrishnan, N., The Synthesis and Characterization of Tributyl Phosphate Grafted Carbon Nanotubes by the Floating Catalytic Chemical Vapor Deposition Method and Their Sorption Behavior Towards Uranium. *New J. Chem.* **2016**, *40*, 1213-1221.

128. Khattak, G. D.; Salim, M. A.; Wenger, L. E.; Gilani, A. H., X-Ray Photoelectron Spectroscopy (Xps) and Magnetic Susceptibility Studies of Copper–Vanadium Phosphate Glasses. *J. Non-Cryst. Solids* **2000**, *262*, 66-79.

Vita

Hei Man (Melissa) Tsui was born in Hong Kong SAR, China on December 11, 1989. She moved to the United States in 2006 and graduated George Mason High School in 2008. She received her Bachelor of Science in Chemistry in 2012 from Virginia Tech, where she graduated Cum Laude. A year later, she began her doctoral studies at Virginia Commonwealth University in the Department of Chemistry.

Awards and Honors

2017 - Gerald and Susan Bass Scholarship
2016 - Lindia M. Vallarino Scholarship
2010 - Dallas Kinser & R.T. Johnson Scholarship

Publications

1. Tsui, M.H.M.; Dryer, D.T.; El-Gendy, A.A.; Carpenter, E.E.; Enhanced Near Room Temperature Magnetocaloric Effect in $La_{0.6}Ca_{0.4}MnO_3$ for Magnetic Refrigeration Application, RSC Advances, 2017,**7**, 46589-46593.

2. Clifford, D.M.; Castino C.E.; Tsui, M.H.M.; Carpenter, E.E.; Fe_xCo_{1-x} Alloy Nanomaterials by Polyol Process: Physocal Property Control by DoE, Dalton Transection, 2017,*46*, 10364-10373.

3. Arachchige, S. M.; Shaw, R.; White, T. A.; Shenoy, V.; Tsui, H-M.; Brewer, K. J., High Turnover in a Photocatalytic System for Water Reduction to Produce Hydrogen Using a Ru, Rh, Ru Photoinitiated Electron Collector. ChemSusChem, 2011, *4*, 514-518.